

THE INFLUENCE OF REINFORCEMENT SIZE ON THE MICROSTRUCTURE AND
MECHANICAL BEHAVIOR OF A NANOSTRUCTURED ALUMINUM-BASED
METAL MATRIX COMPOSITE

by

Nathan Adam Behm

A dissertation submitted to the faculty of
The University of North Carolina at Charlotte
in partial fulfillment of the requirements
for the degree of Doctor of Philosophy in
Nanoscale Science

Charlotte

2015

Approved by:

Dr. Qiuming Wei

Dr. Haitao Zhang

Dr. Harish Cherukuri

Dr. Ronald Smelser

Dr. Don Chen

© 2015
Nathan Adam Behm
ALL RIGHTS RESERVED

ABSTRACT

NATHAN ADAM BEHM. The influence of reinforcement size on the microstructure and mechanical behavior of a nanostructured aluminum-based metal matrix composite.
(Under the direction of DR. QIUMING WEI)

With increased availability and growing commercial applications, aluminum-based metal matrix composites show promise as high specific strength structural materials. Before they can be implemented however, they require thorough characterization and testing. A novel nanostructured aluminum-based metal matrix composite (MMC) was characterized through a combination of microstructural analysis and mechanical testing. Two composites were studied, an aluminum MMC reinforced with 50 nm boron carbide, (B_4C) and an aluminum MMC reinforced with 500 nm boron carbide. Transmission electron microscopy (TEM) analysis revealed an ultra-fine grained matrix with grains on the order of 100 – 300 nm. The quasi-static and dynamic response of the composites was compared with the behavior of the unreinforced aluminum alloy, and it was found that the reinforcement resulted in a 30% improvement in strength. The decrease in the reinforcement size from 500 to 50 nm activated an additional strengthening mechanism, which further improved the strength of the MMC reinforced with the 50 nm B_4C . Dynamic compression tests were performed at elevated temperatures up to 400 °C on the composites, and it was found that they exhibited impressive strengths considering the thermal softening prevalent in aluminum. The reinforcement size was found to play an important role in the strain softening exhibited at elevated temperature, fracture mechanism, and composite strength. Models to describe the composite behavior are presented.

ACKNOWLEDGEMENTS

I would first like to thank my advisor Dr. Wei for his guidance and patience as I transitioned into a new field of research, without his support this dissertation would not have been possible. I would also like to thank Dr. Lavernia and his research group at UC Davis for supplying the materials investigated in this dissertation. Further thanks go Dr. Ron Smelser, Dr. Harish Cherukuri, Dr. Haitao Zhang, and Dr. Don Chen for taking the time to serve as my Committee. I am thankful for the support and assistance from my co-workers and group members, especially Dr. Jianghua Shen who helped me learn many of the instruments used in the course of my research. Thanks must also go to Dr. Baobao Cao who instructed me in the use of the TEM.

I would also like to thank the Army Research Laboratory, Nanoscale Science Program and Graduate School for their financial assistance and making my time here possible.

Finally, I would like to thank my friends and family for their constant encouragement and understanding; I am grateful and lucky to have their support.

TABLE OF CONTENTS	v
LIST OF TABLES	vii
LIST OF FIGURES	viii
LIST OF ABBREVIATIONS	xiii
CHAPTER 1: INTRODUCTION	1
1.1 Aluminum	5
1.2 Metal Matrix Composites	9
1.3 Adiabatic Shear Bands	19
1.4 Split-Hopkinson Pressure Bar	25
1.4.1 Considerations Regarding Kolsky Bar Testing	25
1.4.2 Calculation of Sample Stress and Strain	28
CHAPTER 2: EXPERIMENTAL METHODS	32
2.1 Materials Processing	32
2.1.1 Cryomilling	33
2.1.2 Aluminum Alloy 5083 and Boron Carbide Composites	34
2.2 Microstructural Characterization	35
2.3 Mechanical Testing	37
CHAPTER 3: MICROSTRUCTURE AND MECHANICAL PROPERTIES OF AL 5083 COMPOSITES	40
3.1 Introduction	40
3.2 Experimental Results	42
3.2.1 Microstructural Analysis	42
3.2.2 Dynamic and Quasi-static Compression Tests	46

	vi
3.2.3 Nanoindentation	50
3.3 Discussion	54
3.3.1 Grain Size Strengthening via Hall-Petch Effect	55
3.3.2 Composite Strengthening	56
3.3.3 Rate Dependence and Its Significance	62
3.3.4 Plastic Deformation and Shear Band Formation	64
3.4 Summary and Concluding Remarks	69
CHAPTER 4: COMPRESSIVE BEHAVIOR OF AL 5083 COMPOSITES AT ELEVATED TEMPERATURES	71
4.1 Introduction	71
4.2 Experimental Results	73
4.2.1 Elevated Temperature Compression Tests	73
4.2.2 Post-loading Surface Examination	77
4.3 Discussion	81
4.4 Conclusion	87
CHAPTER 5: INFLUENCE OF REINFORCEMENT SIZE ON COMPOSITE PERFORMANCE	89
5.1 Introduction	89
5.2 Size Effects in Mechanical Properties	90
5.3 Influence of Reinforcement Size on Plastic Response	105
5.4 Conclusion	113
CHAPTER 6: SUMMARY	114
CHAPTER 7: FUTURE WORK	117
REFERENCES	118

LIST OF TABLES

TABLE 2.1: Wt % of constituent elements in Al 5083 alloy	34
TABLE 2.2: Summary of material conditions and sample IDs for the aluminum MMCs used in this investigation.	35
TABLE 3.1: Mechanical properties of the aluminum alloys and composites with coarse-grained Al5083 included for comparison. The coarse-grained aluminum value [94] is used in the calculation of the Hall-Petch strengthening.	52
TABLE 3.2: A selection of yield strength data from the literature is presented for lightweight MMCs, along with information regarding the reinforcement material, type and size. The yield strengths vary significantly based upon reinforcement parameters, but also the processing technique used and the addition of heat treatments or plastic work such as extrusion.	60
TABLE 3.3: The estimated yield strengths of the unreinforced aluminum alloy and reinforced composites and the contributions from the various strengthening mechanisms.	61
TABLE 4.1: The approximate strain softening that occurs in the composite samples at temperatures ranging from RT to 400 °C during dynamic loading. Al-B ₄ C-1 exhibits greater strain softening at all temperatures, with nearly equivalent strain softening after the temperature is increased. Al-B ₄ C-2 shows less strain softening until 300 °C at which point it is approximately equivalent to Al-B ₄ C-1.	74

LIST OF FIGURES

FIGURE 1.1: Composition of commercial aircraft based on data from Boeing. 747, 767, etc. indicate plane model number. The prevalence of aluminum is readily apparent [5].	2
FIGURE 1.2: Categories for aluminum usage and approximate weights for global usage [6].	3
FIGURE 1.3: F-16 with ventral fins produced from DRA sheet for high strength and stiffness [28].	4
FIGURE 1.4: Molten alloy mixing schematic showing the addition of a to a molten alloy being agitated by a mechanical impeller [27].	11
FIGURE 1.5: Schematic demonstrating a general procedure for the mixing and consolidation of a powder processed metal matrix composite [76].	13
FIGURE 1.6: Stress strain data from Kouzeli showing the relationship between decreased particle reinforcement and increased yield strength of aluminum MMCs [107].	16
FIGURE 1.7: Yield stress and % elongation graphed as a function of TiB_2 content (a) showing the improvement of yield strength and decrease of ductility with increasing TiB_2 volume % [110]. The decrease of the composite fracture toughness due to the increased % of SiC clusters (b) from Hong [35].	18
FIGURE 1.8: Optical micrograph of a deformed adiabatic shear band, exhibiting the severe strain localization in the area around the band in an aluminum alloy [112] (a) and a white etched transformed band (b) in a steel 1040 alloy [113].	21
FIGURE 1.9: Schematic representation of a Split-Hopkinson Pressure Bar (SHPB) or Kolsky bar.	27
FIGURE 2.1: Schematic representation of the steps involved in dual mode dynamic (DMD) forging [149].	35
FIGURE 2.2: Picture of the Kolsky bar, high strain rate compression test setup used in this investigation.	38
FIGURE 2.3: Picture of the electric furnace used to heat the dynamic compression samples in the elevated temperatures tests.	39

- FIGURE 3.1: Representative TEM bright field image of Al-B₄C-2 (a) with the corresponding dark field image (b) demonstrating the ring-like pattern indicative of a polycrystalline sample. While the ring-like pattern is evident in (b), there are a large number of discrete spots due to strong diffraction of a few grains. 42
- FIGURE 3.2: TEM images of Al-B₄C-1; the bright field image (a) shows that grains are highly deformed with many dislocations, and without well-defined grain boundaries. The SAED (b) indicates the B₄C diffraction spot isolated to produce the dark field image (c). The reinforcing particles are found to be on the order of 40 – 50 nm. 44
- FIGURE 3.3: The microstructure of NR-AL post-loading (a) exhibits grains on the order of 200 – 250 nm, approximately 100 nm larger than either composite sample. Intermetallic particles formed during cryomilling are highlighted in the bright field (b) and dark field (d). Analysis of the particles reveals that they are approximately 10 nm in diameter. Their size combined with a d-spacing similar to that of aluminum (c) makes it likely that these are AlN particles formed during cryomilling, such dispersoids have been found previously [160]. 45
- FIGURE 3.4: Grain size distribution of matrix grains in Al-B₄C-1 (a), Al-B₄C-2 (b), and NR-AL (c). The distribution and average grain size exhibited in (a) and (b) closely match those from ref. [157], while the average and max grain size of NR-AL indicates that some grain growth likely occurred during processing. 46
- FIGURE 3.5: Representative true stress – true strain results for quasi-static (a) and dynamic (b) compression of the aluminum alloy and composites. The non-reinforced alloy exhibits strain hardening at quasi-static and dynamic strain rates though the strain hardening is much reduced at dynamic rates due to thermal softening. Composite samples undergo strain softening at both strain rates, though softening is greatly diminished for Al-B₄C-1 during quasi-static testing and may be considered elastic-nearly perfect plastic. Quasi-static tests were stopped at a prescribed strain of 0.3 (~30%), and the composite samples failed during testing. Dynamic tests had no prescribed strain and the stress drop at the end is due to sample unloading, no failure was observed. 48
- FIGURE 3.6: SEM images of (a) NR-AL, (b) Al-B₄C-1 and (c) Al-B₄C-2 after dynamic compression. No localized shearing is observed in NR-AL, while both composites exhibit localized plasticity along shear bands. Enlarged inset in (b) shows significant localized shear and crack formation. Highlighted sections of (c) indicate the conjugate shear planes that develop during dynamic deformation. 50
- FIGURE 3.7: SEM image of quasi-statically loaded Al-B₄C-1 exhibiting the brittle fracture the sample underwent without developing the localized plasticity observed in the dynamically deformed composite. 53

- FIGURE 3.8: Strain rate sensitivity of the aluminum alloy and composites indicating low rate dependence. The high strain rate data was collected from dynamic compression, while the low strain rate data points were a result of strain-rate jump tests performed during nanoindentation. 54
- FIGURE 4.1: The transition of the primary damage mechanism from particle cracking to interparticle voiding due to the reinforcement volume fraction %. As the volume fraction increases, interparticle void formation becomes more likely [75]. 72
- FIGURE 4.2: The elevated temperature response of Al-B₄C-1 (a) and Al-B₄C-2 (b) from RT to 400 °C. Significant strain softening is exhibited by both composites, though Al-B₄C-2 underwent less strain softening at temperatures below 300 °C. 75
- FIGURE 4.3: Strain softening exhibited by Al-B₄C-1 and Al-B₄C-2 under dynamic loading at room, and elevated temperatures. Al-B₄C-1 undergoes significant strain softening at all temperatures with a small increase in average softening at 300 °C. Al-B₄C-2 undergoes consistently lower strain softening until 300 °C when softening increases dramatically, possibly indicating a critical softening temperature. 76
- FIGURE 4.4: Representative flow curves for both composites comparing their response to dynamic loads. The differences in flow softening identified earlier are more pronounced here. In addition to strain softening, progressive flow softening as a result of increased temperature is readily apparent. 77
- FIGURE 4.5: SEM surface evaluations of Al-B₄C-1 at 100 (a-b) and 200 °C (c-d) after dynamic loading. Enlarged images of the highlighted areas in (a) and (b) are shown in (b) and (d) respectively. The high temperatures that develop along the ASBs are severe enough to cause melting as evidenced in (b), and the large strain localization and flow lines are easily seen in (d). 78
- FIGURE. 4.6: Similar to the observations at lower temperatures, the SEM surface analysis at 300 (a-b) and 400 °C (c-d) reveals that significant strain localization and heating continues to occur. 79
- FIGURE 4.7: The post-loading SEM images of Al-B₄C-2 at 100 (a-b) and 200 °C (c-d) show that ASBs still form, though they are less pronounced than those in Al-B₄C-1. Additionally, the strain localization resulting in the formation of the ASBs is not apparent on the specimen surface. The significant heating is still visible in the melted matrix along the shear band as seen in (d). 80
- FIGURE. 4.8: The elevated temperature SEM analysis of Al-B₄C-2 at 300 (a-b) and 400 °C (c-d) is shown here. While the 400 °C sample displays the greater softening and cracking expected at higher temperatures, the 300 °C sample shown in (a-b) exhibits very little cracking. 81

- FIGURE 4.9: After a void is nucleated in a matrix material, the results from Wu and Ramesh indicate that as long as the void is above a minimum size of 10 nm, it will quickly grow to an equivalent void size with void growth equalizing [182]. 84
- FIGURE 4.10: The transition temperature where the primary fracture mechanism switches from particle cracking to void nucleation (a). While (b) demonstrates the flow softening and increased strain softening that occurs at elevated temperatures of an aluminum MMC [189]. 86
- FIGURE 5.1: A schematic for the process of dislocation bowing and the generation of dislocation loops around small impenetrable particles in a ductile matrix [43]. 91
- FIGURE 5.2: A TEM micrograph demonstrating examples of dislocation bowing in an alloy with in-situ particles. Areas labeled *A* show dislocations interacting with the particles while *B* shows the formation of dislocation loops [43]. 93
- FIGURE 5.3: A simple schema for the generation of geometrically necessary dislocations at the matrix/particle interface [106]. 94
- FIGURE 5.4: A diagram for a particle residing in a metal matrix (a) and the dislocations that form around the inclusion (b) leading to a punch out structure. Also shown are the experimental results for the yield strength of aluminum composites with varying quench differentials. The different quenching temperatures should lead to differences in yield strength, but an absence of CTE mismatch hardening is observed instead [166]. 97
- FIGURE 5.5: The improved fatigue behavior for an aluminum alloy reinforced with SiC is shown in terms of reinforcement size (a) and volume fraction of loading (b) [199]. 100
- FIGURE 5.6: The S-N (a) and elastic strain amplitude (b) curves for a magnesium MMC reinforced with SiC. While (a) would indicate that the 15 SiC reinforcement produces superior performance, when the results are normalized by the elastic modulus, it is seen that the AZ91 alloy actually exhibits the best performance [197]. 102
- FIGURE 5.7: Comparison of the model from Ding [198] to experimental results, trying to understand and predict the size effect of the reinforcement on fatigue performance. 105
- FIGURE 5.8: Comparison of damage mechanisms occurring in MMCs with (a) depicting the fraction of broken reinforcement as a function of strain and particle size. When the loading of the reinforcement is increased, it is shown to reduce the strain at which the Considère criterion is fulfilled (b). This is primarily due to an increase in the number of sites for void nucleation or particle cracking [77]. 108

FIGURE 5.9: Post-loading micrographs depicting the dependence of shear band formation on the size of the reinforcing particles. When the particles are larger they “get in the way” and impede the formation of ASB. However, once the reinforcement is small enough ASB formation can proceed (a) [205].

LIST OF ABBREVIATIONS

ASB	adiabatic shear band
BF	bright field
BMG	bulk metallic glass
CTE	coefficient of thermal expansion
CTOD	crack tip opening displacement
DMD	dual mode dynamic
DRA	discontinuously reinforced aluminum
DY	dynamic
ECAP	equal-channel angular pressing
FCC	face-centered cubic
GND	geometrically necessary dislocations
GP	Guinier-Preston
HIP	hot-isostatic pressing
ID	identification
MA	mechanical alloying
MMC	metal matrix composite
NC	nanocrystalline
PIP	precision ion polishing
PM	powder metallurgy
QS	quasi-static
RT	room temperature
SAED	select area electron diffraction

SEM	scanning electron microscope
SHPB	split-Hopkinson pressure bar
SRS	strain rate sensitivity
TEM	transmission electron microscope
UFG	ultra-fine grain

CHAPTER 1: INTRODUCTION

Between limited natural resources and increasing global population, energy production and management has been an important research area for decades. It is a complicated issue, and it is important to remember that energy efficiency is nearly as important as the source of that energy. Clean, renewable energy has been the focus of many research areas from photovoltaics to organic solar cells to thermoelectric generation, just to name a few. In addition to increased clean energy production, it is necessary to reduce the energy consumption requirements that are placed on any nascent renewable energy infrastructure. One step towards reducing energy consumption is to make energy intensive tasks more efficient. Efficiency comes in many forms from fuel use per unit thrust, to aerodynamic improvements, to structural or weight reduction improvements [1, 2]. In the pursuit of weight reduction, aluminum alloys and composites are an attractive option. High strength aluminum alloys and composites already make up a significant portion of most modern aircraft (Fig. 1.1), and have started to become more common in automobiles as well [3]. Perhaps the most significant indicator of the growing prevalence of aluminum in the auto manufacturing industry is the decision by the Ford Motor Company to replace the body of the 2015 F-150, America's highest selling truck, out of aluminum [4].

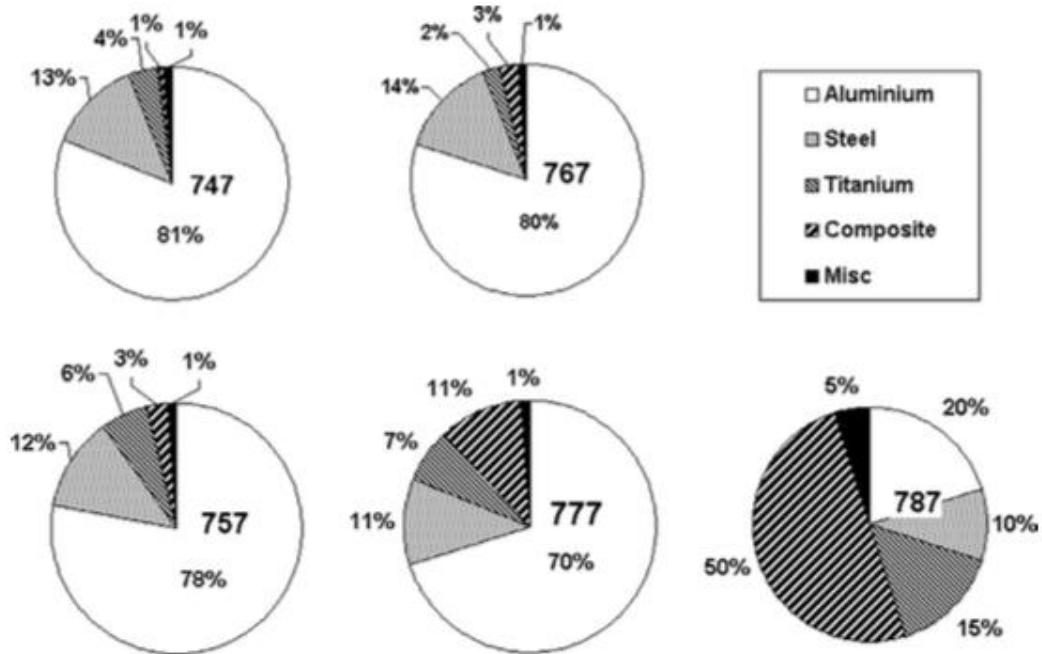


Figure 1.1: Composition of commercial aircraft based on data from Boeing. 747, 767, etc. indicate plane model number. The prevalence of aluminum is readily apparent [5].

The aluminum industry in the United States is already well developed with projected demand greater than 11 million metric tons [6], which after accounting for density is approximately 25% of the projected demand for steel during the same period [7]. The aluminum market is only going to increase as the global population, and the transportation and construction projects to sustain them, continue to grow. As can be seen in Fig. 1.2, aluminum extends well beyond automobiles and aircraft to packaging, consumer goods, electrical products and more [6]. However, the aluminum used in the most energy intensive applications, such as the aerospace and automotive industries, is not in its elemental form but has been alloyed to create a higher strength, tougher

material. Details of the alloying process and the mechanisms involved will be discussed in section 1.1.

Producer Shipments plus Imports		
figures in millions of pounds		
Product Form	2013	% of total
Sheet, Plate & Foil	10,634	43.9
Extrusions	4,430	18.3
Electrical Wire & Cable	858	3.5
Other	561	2.3
Total Mill Products	16,483	68.1
Ingot for Castings & Other	7,733	31.9
Total Aluminum Demand	24,216	100.0

Figure 1.2: Categories for aluminum usage and approximate weights for global usage [6].

In addition to alloying, further modification to the strength, elastic modulus, density and other material properties can be achieved through the use of reinforcement materials. A composite material consists of at least two phases, the matrix and the reinforcement material, with the matrix acting as the base material [8-19]. Likely the most well known composite material is carbon fiber, a shortened name for carbon fiber-reinforced plastic, a material that has been researched for the better part of 40 years [9, 12, 13, 20-26]. Carbon and glass fiber-reinforced polymer matrices exhibit excellent specific strengths and specific moduli, surpassing that of comparable metallic aerospace alloys [27] while also experiencing fewer issues with corrosion when compared to metallic alloys. However, they do suffer a number of drawbacks such as increased material cost, highly anisotropic mechanical properties, low damage tolerance and a

susceptibility to moisture and high temperature [27]. As a consequence, metal matrix composites such as those at the focus of this dissertation may provide an effective means of creating low density, high strength materials while maintaining isotropic response, and toughness. One commercial example where discontinuously reinforced aluminum (DRA) composites have been used is in the high strength ventral fins in the F-16 (Fig. 1.3).



Figure 1.3: F-16 with ventral fins produced from DRA sheet for high strength and stiffness [28].

The reinforcements used in a composite material come in numerous forms varying in aspect ratio, dimension, and material composition [29-37], all of which affect the final properties of the composite. Due to the number of variables involved, fully characterizing the influence of the various reinforcement parameters on the material behavior is of critical importance to the commercialization of any composite. The

behavior of a new composite must be characterized so that models can be produced which enable manufacturers to predict the behavior of the material in their desired application. Since comprehensive size-dependence studies on the effect of boron carbide reinforcement on nanostructured aluminum are not readily available in the literature, this study strives to characterize the influence of reinforcement size, as well as document the impressive mechanical properties exhibited by this nanostructured aluminum composite. The finer points of aluminum, its alloys and the metal matrix composite process are discussed in the following sections.

1.1 Aluminum

As common as aluminum is today, it may be a surprise to discover this was not always the case. Aluminum was first discovered in 1827 by Friedrich Wöhler [38], but because it has strong chemical bonds in its natural formations, it was not easy to isolate. As a result of its limited availability, it became a precious metal and was used in jewelry as well as for special projects such as the capstone on the Washington Monument in Washington D.C. [39].

It wasn't until 1886 that a commercially viable method of isolating aluminum was found. Paul Héroult working in France, and Charles Hall working in the United States independently discovered a method of performing the electrolysis of an aluminum salt in a non-water solvent that produced aluminum instead of aluminum hydroxide [40]. The following year, an Australian engineer, Karl Josef Bayer developed a chemical method to extract aluminum from bauxite, a commonly occurring aluminum ore [41]. These developments, and the creation of new hydroelectric production facilities provided the

necessary electrical capacity for large-scale aluminum production and would see the beginning of aluminum's widespread adoption.

The prevalence of aluminum is not hard to explain, as aluminum is an abundant and therefore affordable metal, it has a low density of 2.70 g/cm^3 [42], exhibits excellent ductility and has an electrical conductivity only slightly less than that of copper [42]. Aluminum's impressive ductility comes from its FCC crystal structure that allows for 12 slip systems [43], and its close-packed atomic structure. While aluminum is frequently considered as corrosion resistant, this is somewhat incorrect, as aluminum is actually highly reactive. Due to that reactivity however, a thin film of Al_2O_3 forms rapidly on the surface of exposed pure aluminum, and the dense aluminum oxide film that develops is inert, serving as a protective layer [44]. Corrosion can still occur at high or low pH values however; so care must be taken when considering the application in question [45]. As an extension of aluminum's high ductility, it also has excellent formability that both reduces production costs and allows for a wide range of shapes and structures to be produced making it a valuable material for metal forming operations.

While aluminum has many advantageous properties, enhancements can be made through the introduction of alloying element such as copper, magnesium, silicon, zinc, and lithium [5, 27, 46-48] to name some of the most common constituents. These alloying elements introduce strains and distortions in the crystal lattice of the solvent metal that impede dislocation motion, strengthening the alloy [49], and can also be used to produce some grain refinement [50, 51]. While each of the alloys benefit from solid solution strengthening, some of the alloys are also heat treatable, which can result in greatly improved strength and hardness. Of particular interest to the aerospace industry

have been the heat treatable aluminum alloys that result from the addition of copper, the 2XXX series, and zinc the 7XXX series of aluminum alloys [27]. In contrast to non-heat treatable alloys which only soften or have reduced solid solubility at elevated temperatures [52], heat treatable aluminum alloys have increased solid solubility at elevated temperature [53-56]. As a result, the temperature can be raised during processing to a value above the liquid transition of the solvent material, placing the alloying elements in solution. Once the solute atoms are in solution, the temperature is held for a period of time, followed by a rapid quench which traps the soluble elements in solution and results in a super-saturated solid solution [57]. This super-saturated solid solution can be decomposed into a two-phase system either via artificial aging or natural aging. Artificial aging takes place at an elevated temperature that remains below the solvus line following the quench. This aging process allows for the diffusion and nucleation of the alloying elements into fine particles that are distributed throughout the alloy. The particles provide additional resistance to dislocation movement, both due to their presence and the strain they induce in the lattice structure, further increasing the strength and hardness of the alloy beyond that which results from solid solution strengthening [56, 58] alone. Due to the growth the particles undergo with increasing aging duration, the temperature and length of aging must be carefully controlled to produce the desired mechanical properties.

The precipitation hardening that occurs in 2XXX and 7XXX series aluminum alloys [27, 44], those alloyed with copper and zinc respectively, results in strength-to-weight ratios competitive with the stronger, but heavier titanium and steel. The 7XXX series, as well as many work hardening alloys, follow a specific sequence during

precipitation hardening, starting with a supersaturated solution, followed by the development of Guinier-Preston (GP) zones, and then the formation of intermediate precipitates [27, 58]. While the number of intermediate precipitates and the form that they take depends on the particular alloy, a similar trend is generally followed. Due to the importance of precipitation hardening in aluminum and other alloys, efforts have been made to model the strengthening that will occur based on material parameters [59]. Due to their high strength and stiffness, the 2XXX and 7XXX series of aluminum alloys have been of interest to the aerospace industry for some time. Additionally, tempering and post-processing anneals can be used to tailor the fracture toughness and strength of a heat-treatable composite, to best suit the application in which they are to be used.

Of particular interest in this investigation are the microstructural features and mechanical properties of the aluminum alloy series with Mg as its primary alloying element, specifically Al 5083. The 5XXX series of aluminum alloys is the strongest of the non-heat treatable aluminum alloys, and it can be work hardened through post-processing techniques such as rolling, extrusion or equal-channel angular pressing (ECAP) [60-62]. A considerable body of research has been accumulated on ultra-fine grain (UFG) Al 5083 and its behavior at both cryogenic and room temperatures [63-65]. At room temperature, UFG Al 5083 undergoes solid solution strengthening and grain refinement strengthening following the Hall-Petch relationship [66, 67]. As with other face-centered cubic (FCC) metals, the low thermal activation required for gliding dislocations allows Al 5083 to maintain its ductility with little to no effect on yield strength at low or cryogenic temperatures [68]. At elevated temperatures however, it was found that Al 5083 exhibited a superplastic response [62, 69-71]; with strain rate

sensitivity values of ~ 0.4 at quasi-static strain rates, and elongations over 300% are possible at temperatures as low as 548 K [70]. Such superplastic behavior can greatly reduce costs during forming operations in manufacturing of body sheets, as well as reduce the number of subsequent processing steps necessary. The process used to create an alloy is an important parameter as well, with methods of composite processing including melt processing, mechanical alloying, and cryomilling. The method used to create the Al 5083 alloy used in this investigation, and a comparison to other techniques, will be presented in the following chapter.

1.2 Metal Matrix Composites

Carbon fiber reinforced polymer matrix composites, which were discussed earlier, are an example of polymer matrix composites and as the name suggests, the matrix material consists of a polymer or epoxy. Similarly, a metal matrix composite (MMC) has a metal matrix and will be at the focus of this section. Some of the methods for composite formation and the processing parameters involved will be discussed in this section. While Al 5083 is the matrix material of the composites studied in this investigation, pertinent background on multiple types of MMCs will be presented, with specifics to follow in the next chapter.

The MMC industry has been growing steadily throughout the 21st century, from around 2500 metric tons in 1999 [28, 72] to 5900 metric tons in 2013 [73]. Of that, 69% by mass is in the form of discontinuously reinforced aluminum, which is also the class of material studied in the course of this dissertation. While there are many methods available to consolidate and form MMCs, some of the most common are liquid-metal infiltration [74], stir casting [28], and powder metallurgy [75]. Additional methods such

as spray casting are possible, however the most commercially viable methods fall under the previous categories as they are cheaper and less complicated. The choice of processing method is generally dependent upon the matrix material and the type of reinforcement being used, as they impose restrictions on processing methods available. Since the material of interest in this study is a discontinuously reinforced aluminum composite, this brief review of MMCs will focus on particulate reinforcement techniques. Interested readers are directed to the comprehensive review by Ibrahim and Lavernia [76] for further information on other reinforcement types and specific details.

One of the driving considerations for the use of MMCs is the improvement they impart to material strength and stiffness, both of which are useful in structural applications [28, 77]. Ceramic materials while very strong are also brittle, and the process to modify them to increase their fracture toughness can be difficult [78, 79]. The high hardness and stiffness of ceramic materials do however make them excellent candidates for use in composite materials [33, 80-82]. In order for efficient strengthening to occur, there must be good interfacial bonding between the reinforcement and the matrix. Poor bonding leads to early fracture resulting from void nucleation, effectively reducing the composite strength as compared to the base matrix strength [76, 83]. Commonly used ceramic reinforcements include carbides and oxides such as SiC, B₄C, and Al₂O₃ due to their wide availability and contributions to material strength [30-32, 35, 80, 84-95]. The chosen processing method also has a significant impact on the resultant material properties as techniques vary in temperature and the phase in which they mix the constituent materials.

One common processing method is liquid metal infiltration, which is the process of introducing a molten alloy to a ceramic preform [96]. While the infiltration can be allowed to proceed without additional pressure this generally results in a less dense composite that requires additional processing [75] and as such an inert gas or mechanical system is often used to pressurize the melt. Wetting of the particulate surface can be problematic and is a factor of alloy / reinforcement composition, surface treatments of the reinforcement, temperature and more [96-99]. A somewhat similar processing method involves the introduction of the ceramic reinforcement into a molten alloy [75]. The low viscosity of the molten alloy which would otherwise lead to high instances of particulate agglomeration is overcome by using an impeller to agitate the alloy while adding the reinforcement, and an example is shown in Fig. 1.4 [27].

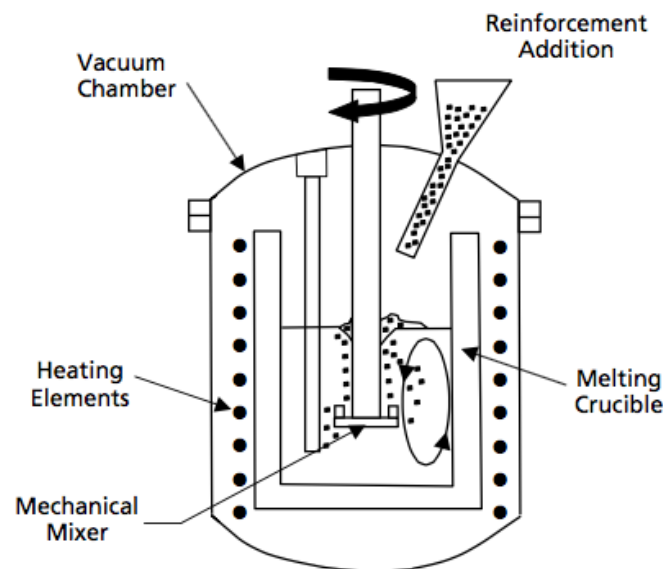


Figure 1.4: Molten alloy mixing schematic showing the addition of a reinforcement to a molten alloy being agitated by a mechanical impeller [27].

High temperatures and mechanical agitation are used to disrupt films that form around the reinforcements and helps interfacial bonding. Much like melt infiltration, wetting of ceramic particles is a challenge, and methods such as reinforcement coatings and the addition of matrix alloying elements such as Mg are used to help improve matrix-reinforcement bonding [27, 76, 97]. The last method to be discussed is powder metallurgy (PM), which involves the blending of rapidly solidified powders with particulates [100-102]. In contrast to the previously discussed methods, both the matrix and reinforcement are in the solid phase and as a result, fewer residual stresses and reaction products are formed in the final product [27, 103]. Powder metallurgy methods all follow a similar series of steps: mixing of constituent materials, compacting to ~50% density, degassing of the preform, and then a consolidation method such as hot isostatic pressing, dual-mode dynamic forging (Fig. 1.5), or some form of sintering [86, 104], often followed by either extrusion or rolling [33].

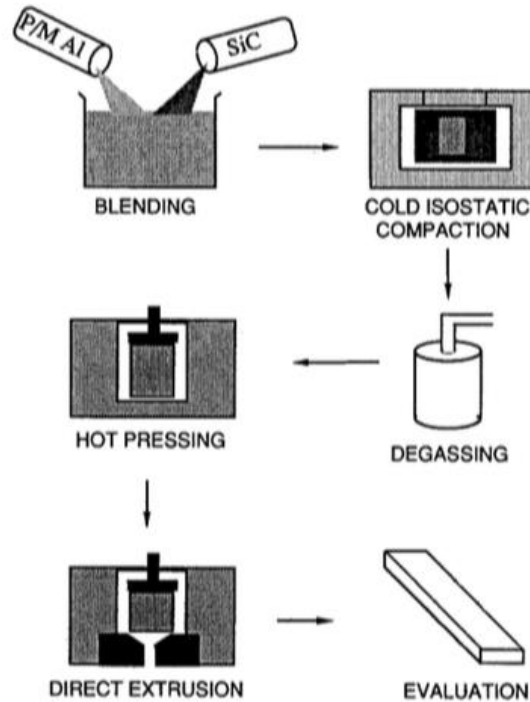


Figure 1.5: Schematic demonstrating a general procedure for the mixing and consolidation of a powder processed metal matrix composite [76].

Microstructure plays a key role in the material properties of all materials, and there are some unique microstructural features of MMCs that influence their mechanical properties. Of particular importance are the size and volume fraction of reinforcement particles. One measure of an MMC is the interparticle spacing, which can be derived from the particle size [105]:

$$\bar{\lambda} = \bar{d}(\sqrt{\pi/4V_p} - 1) \quad 1.1$$

$$\bar{d} = \sqrt{\frac{2}{3}} \cdot d \quad 1.2$$

where \bar{d} is the mean particle size, V_p is the volume fraction of the reinforcement particles and $\bar{\lambda}$ is the mean interparticle spacing. When the particulate reinforcement is smaller than the grain size of the material, then the particles can reside within the grain and resist dislocation movement. The smaller the particles, the smaller the interparticle spacing for a given volume fraction and the greater the influence they exert on dislocations. The additional resistance to dislocation movement by hard particles residing in the matrix grains is known as Orowan strengthening [94]. An expression for Orowan strengthening is provided in Eq. 1.3:

$$\Delta\sigma_{Or} = \frac{1.25G_m b \ln(\bar{d}/b)}{\pi\sqrt{1-\nu} \bar{\lambda}} \quad 1.3$$

where $\Delta\sigma_{Or}$ is the yield strength increase due to Orowan strengthening, G_m is the shear modulus of the matrix taken as 27 GPa [105] for this aluminum alloy, b is the Burgers vector of the matrix, and ν is the Poisson's ratio of 0.33. Additional strengthening can result from residual strains between the reinforcement and matrix due to elastic modulus mismatch (Eq. 1.4) [106], that result in geometrically necessary dislocations:

$$\Delta\sigma_{GND} = kG_m b \sqrt{\frac{8V_p \varepsilon_y}{bd}} \quad 1.4$$

where k is a constant, in this case 1.25, and ε_y is the yield strain which is taken as 0.2% or 0.002. A further mechanism that can occur is due to the coefficient of thermal expansion (CTE) mismatch between the matrix and reinforcement that results in the formation of additional dislocations, an equation based on material parameters is given in Eq. 1.5 [77], with the density of dislocations given by Kouzeli [107]:

$$\Delta\sigma_{CTE} = \eta G_m b \sqrt{\rho} \quad 1.5$$

$$\rho = \frac{12V_p \Delta T \Delta CTE}{bd(1-V_p)} \quad 1.6$$

where $\Delta\sigma_{CTE}$ is the strength improvement resulting from a CTE mismatch between the particle and matrix, ΔT is the difference between the processing temperature and the testing temperature, and ΔCTE is the difference between the materials' coefficients of thermal expansion.

A trend that has been established over many investigations, and that shows in the constitutive equations above. Greater increases in strength are obtained as the size of the particulate reinforcement is decreased, and as the loading volume fraction increases [77, 83, 93, 101, 106, 108, 109]. An example of the relationship between yield stress and the increase that occurs as reinforcement size is reduced is shown in Fig. 1.6 [107]. In the case shown in Fig. 1.6, two reinforcement types are shown, Al_2O_3 on the top and B_4C at the bottom; the labels indicate the approximate size of the reinforcement in micrometers.

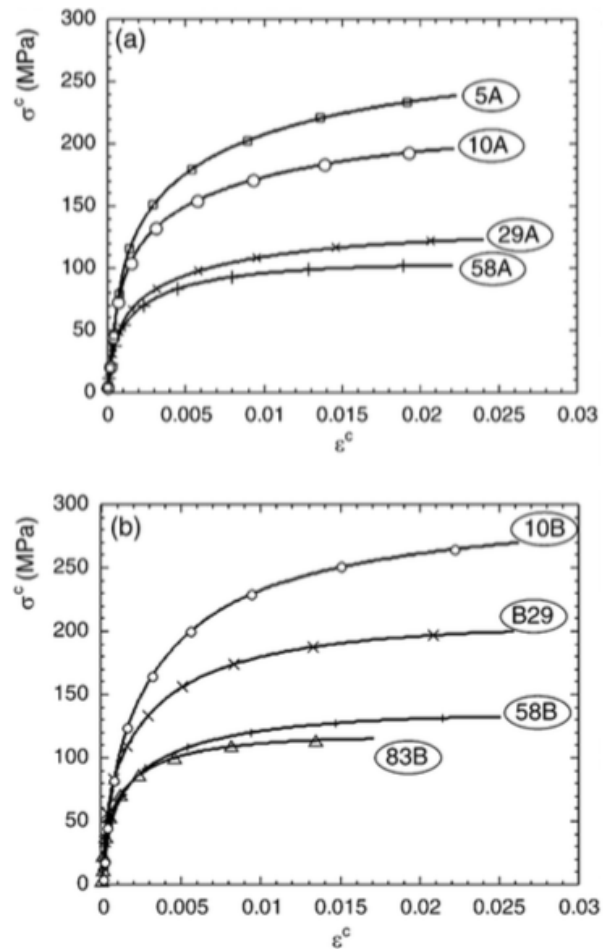


Figure 1.6: Stress strain data from Kouzeli showing the relationship between decreased particle reinforcement and increased yield strength of aluminum MMCs [107].

However, the loading volume fraction cannot be increased without limit, as Figure 1.7a shows both the benefit and drawback of increasing the volume fraction of reinforcement in a composite [110]. There is a marked increase in the yield strength as the volume fraction increases, but the percent elongation steadily decreases at the same time. One reason for the decreased plastic response is the increased agglomeration that occurs when more particles reside within the matrix. In a study by Hong et. al [35], the Mode I fracture

toughness was plotted along with the volume % of SiC clusters that formed versus the volume % of SiC added to the composite Fig. 1.7b.

The impressive mechanical properties exhibited by metal matrix composites have already been realized by many industries, and MMCs continue to be an important topic of research. The investigation presented here will focus on a nanostructured DRA composite with a matrix composed of Al 5083 and reinforced with boron carbide. The microstructure and mechanical properties of the aluminum composite will be investigated with special attention paid to the influence of reinforcement size on the mechanical properties.

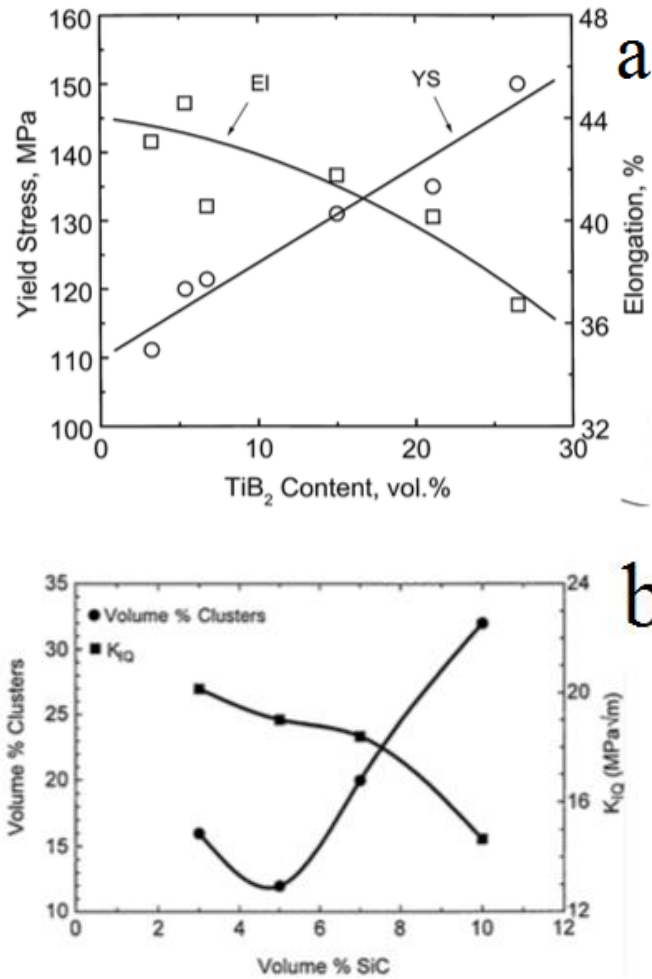


Figure 1.7: Yield stress and % elongation graphed as a function of TiB_2 content (a) showing the improvement of yield strength and decrease of ductility with increasing TiB_2 volume % [110]. The decrease of the composite fracture toughness due to the increased % of SiC clusters (b) from Hong [35].

1.3 Adiabatic Shear Bands

Adiabatic shear bands (ASBs) are the name given to highly localized areas of shear strain that develop in some materials at high strain rates. While the name ‘adiabatic’ is somewhat of an exaggeration, it was used by Zener and Hollomon [111] to describe the behavior they witnessed during the high strain rate deformation of steel, and the term stuck. The heating that occurs within the localized shear band while not truly adiabatic, is still highly localized and mostly confined to the band. The observation of ASBs in steel provides some of the best evidence of the significant local temperature rise that occurs during loading. Two ASB are shown in Fig. 1.8, one that developed in a 2014 aluminum alloy [112], and the other in 1040 steel [113]. While both are areas of highly localized shear strain, the aluminum alloy developed a deformed shear band, while the steel exhibits a transformed shear band, so named because the high temperature developed during deformation results in the phase transformation of ferrite to austenite which quenches to martensite [113] and produces a white band upon etching. Zener and Holloman estimated that strains of approximately 5 could result in a temperature rise of 1000 °C, and that the bands they observed in steel could represent shear strains as large as 100 [111]. Multiple equations exist to estimate that temperature rise that occurs in a shear band, one of which is presented in Eq. 1.7 [114].

$$\Delta T = \frac{\beta}{\rho C_p} \int_0^{\varepsilon_f} \sigma d\varepsilon \quad 1.7$$

In Eq. 1.7 β is the fraction of plastic work converted to heat, approximately 0.9, ρ is the density of the material, C_p is the specific heat, and ε_f is the final strain. Eq. 1.7 only

provides a rough estimate of the temperature rise, as there are difficulties in estimating the width of the shear band and the strain it undergoes. However, an attempt was made by Bai and Dodd [115], who performed a perturbation analysis based on the solutions of equations governing the formation of ASBs, and yielding Eq. 1.8 for the half-width of an ASB.

$$\delta \approx \left(\frac{kT_*}{\tau_* \dot{\gamma}_*} \right)^{1/2} \quad 1.8$$

The thermal conductivity of the material is represented by k , T is the temperature, τ is the shear stress and $\dot{\gamma}$ is the shear strain rate. The * subscript indicates that the parameter represents conditions within the shear band, and $\dot{\gamma}$ has been demonstrated to be approximately three times the imposed strain rate [116].

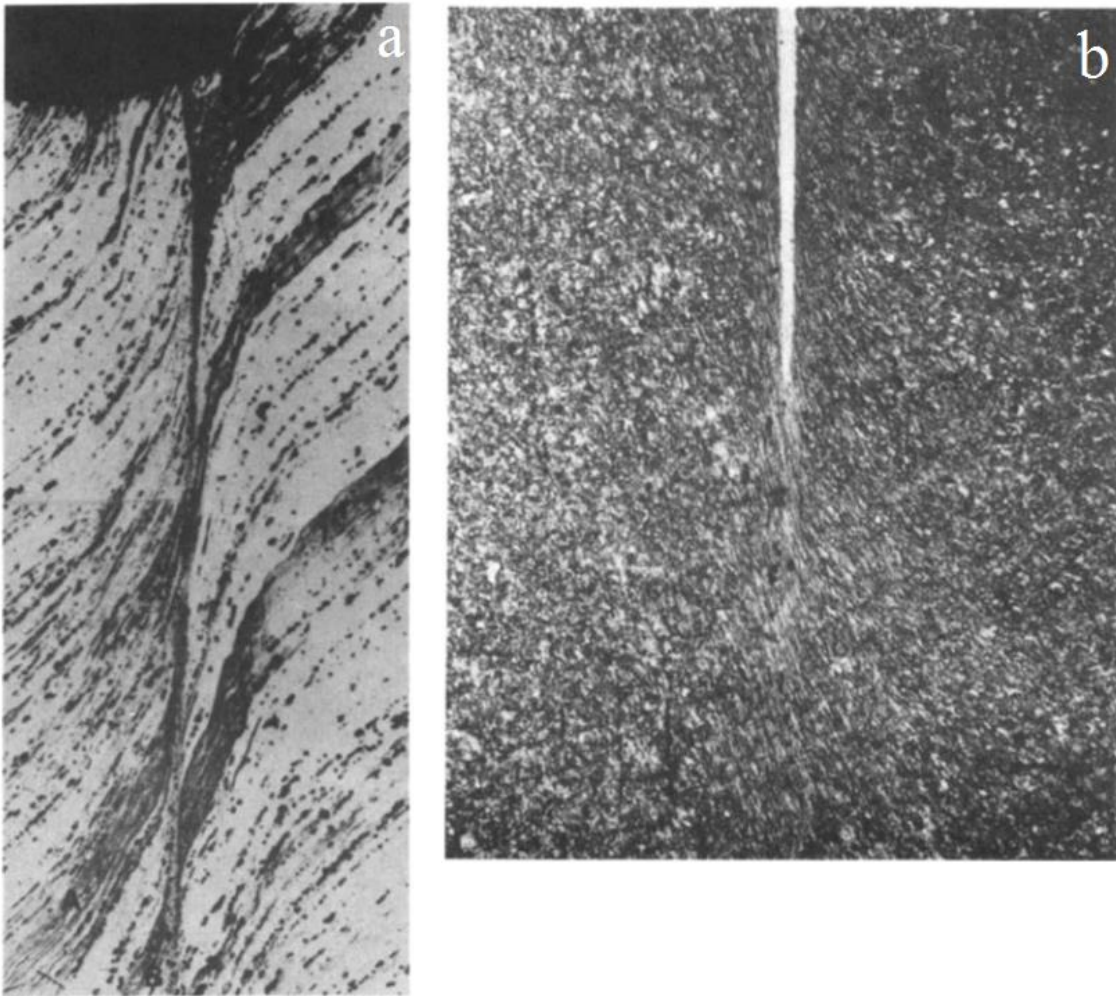


Figure 1.8: Optical micrograph of a deformed adiabatic shear band, exhibiting the severe strain localization in the area around the band in an aluminum alloy [112] (a) and a white etched transformed band (b) in a steel 1040 alloy [113].

While ASB are usually observed during the high strain rate deformation of materials such as during rod impact tests, explosive tests, high-speed tooling, or ballistic tests under compressive conditions, some exceptions apply at cryogenic temperatures. Adiabatic shear bands have been found to form at quasi-static strain rates under tensile loading when the test is performed at near liquid helium temperature, for a variety of

materials. This low temperature behavior is a result of the greatly reduced specific heat that is a consequence of the finite phonon energy states available at low temperature as developed by Debye [117]. Some of the materials that developed ASB at cryogenic temperatures include Ta-W alloys, stainless steel [118], pure aluminum [119, 120] and aluminum alloys [121]. The flow curves that resulted from the low temperature tests exhibited serrated flow resulting from adiabatic heating that softened the material due to low heat capacity and high thermal sensitivity, which then stabilized as the stress was relaxed.

More common than low temperature formation, ASB formation has been observed at room and elevated temperatures in a variety of materials such as steel [111, 122], UFG Fe [114, 123], Ti [104] and bulk metallic glasses [124, 125]. The mechanism behind ASB formation is essentially a competitive process between strain hardening and thermal softening [113]. That basic relationship has been used to develop many criteria for the onset of plastic instability and ASB formation. In the example of high-speed machining, Recht [126] neglected aspects of strain rate effects and changes in the area of the shear plane, obtaining Eq. 1.9 for the formation of chips in high-speed machining:

$$\frac{d\tau}{d\varepsilon} = \frac{\partial\tau}{\partial\varepsilon} + \frac{\partial\tau}{\partial\theta} \frac{d\theta}{d\varepsilon} \quad 1.9$$

In Eq. 1.9, τ is the shear stress and θ is the temperature. In another treatment, Bowden [127] used the empirical parameters of characteristic strain γ^* and initial strain inhomogeneity $\Delta\gamma$, found during quasi-static testing, to develop a relationship that predicts if the strain inhomogeneity will rapidly increase:

$$\gamma_m^D = \gamma^* \ln \left(\frac{\gamma^*}{\Delta\gamma} \right) \quad 1.10$$

where γ_m^D is the strain needed before the strain rate within the band will double, and

$\gamma^* = \frac{\dot{\gamma}_0}{G}$ where $\dot{\gamma}_0$ is the applied shear strain rate and G is the gradient of the contours of

constant stress, taken as a constant. On the other hand, Grady [128] took a different approach, using material properties to develop a “shear band toughness” that functions similarly to a material fracture toughness. Starting from one-dimensional equations for rigid planar thermoplastic shear:

$$\rho \frac{\partial v_y}{\partial t} = \frac{\partial \tau}{\partial x} \quad 1.11$$

$$\frac{\partial \theta}{\partial t} = \frac{\tau}{\rho C_p} \frac{\partial v_y}{\partial x} + \chi \frac{\partial^2 \theta}{\partial x^2} \quad 1.12$$

where $v_y(x, t)$, $\tau(x, t)$, $\theta(x, t)$ are the fields of velocity, shear stress and temperature in the vicinity of the shear band respectively, and χ is the thermal diffusivity. Grady then made some simplifying assumptions, and taking the constitutive expression for the thermal softening of the shear stress within the shear band as $\tau = \tau_y(1 - \alpha\theta)$, Grady developed an expression for the energy dissipated in the shear band, and related it to the elastic shear modulus to obtain a shear band toughness [129]:

$$\Gamma_{c0} = \frac{\rho C_p}{\alpha} \left(\frac{9\rho^3 C_p^2 \chi^3}{\tau_y^3 \alpha^2 \dot{\gamma}} \right)^{1/4} \quad 1.13$$

$$K_s = \sqrt{2G_m \Gamma_s} \quad 1.14$$

where α is the linear thermal softening, Γ_{c0} is the shear band dissipation energy, and K_s is the shear band toughness. The shear band toughness for a material gives a qualitative measure of the likelihood for a material to form an adiabatic shear band during dynamic deformation. A closer look at Grady's shear band toughness and a comparison to experimental values will be presented in Chapter 3.

In addition to high-speed machining, ASB formation plays a very important role in ballistic impact. Adiabatic shear band formation is important in both penetrators and armors and early studies looked at several armors such as aluminum, steel, and brass [112, 130, 131] and penetrators of tungsten and uranium [113]. As one might expect, the development of plastic instability and localized shearing is not a desired quality in armors when the shear band is of the deformed type. It was found that aluminum and brass alloys that developed shear bands also had extensive cracks that traveled through the armor plate leading to fracture [130, 131]. In contrast, adiabatic shear can be beneficial when used in ballistic penetrators, as the propensity to shear helps the penetrator keep its point [132, 133]. Depleted uranium has long been used as a kinetic energy penetrator due to its high density and ASB-assisted penetration mechanics.

1.4 Split-Hopkinson Pressure Bar

As mentioned in the last section, adiabatic shear banding is a particularly important deformation mode when studying the dynamic compression behavior of materials. In order to facilitate that study a number of techniques have been developed to impose dynamic strain rates on test specimens including, split-Hopkinson torsional bar [132], thick-walled cylinder explosive collapse [134], and split-Hopkinson pressure bar (SHPB). A SHPB is also known as a Kolsky bar in recognition of modifications that Kolsky [135] made to Hopkinson's [136] single-bar setup. There are also methods to prepare samples that promote the development of shear bands, such as hat-shaped specimens [134] and double-shear samples [137]. If the deformation mechanism of the material prepared without preferential geometry is already known, such processes can assist in the study of shear banding. However, if the deformation mechanism is still not understood for the material being studied, using preferentially shaped samples will not provide true information regarding the mechanical properties of the material and could be detrimental and misleading. In the investigation presented in this dissertation, a split-Hopkinson pressure bar was used along with rectangular samples with an approximate aspect ratio of 1.25 (for the side dimension with respect to the gage height). The theory and relevant details regarding the setup will be briefly discussed in the following subsections.

1.4.1 Considerations Regarding Kolsky Bar Testing

Dynamic compression tests differ from their quasi-static counterparts, and as a result certain considerations need to be made. One such consideration is related to the rate at which the loading occurs, and the consequences that arise as a result. For instance,

if you consider holding one end of a slack rope that is attached to a wall and then apply a sharp flick of your wrist, you would see a wave begin to travel down the rope, and possibly travel all the way to the wall. Such an analogy is only appropriate in a conceptual manner, but it reflects the idea that there is a finite wave that travels along a medium with a finite speed. In the case of a Kolsky bar experiment, the wave is a pressure wave and the medium is an elastic bar with a wave velocity of $c_{EL} = \sqrt{E / \rho}$ where E and ρ are the Young's modulus and density of the bar. Before continuing with the breakdown and experimental conditions necessary for analysis, a brief description of the steps that occur during testing would be helpful.

An experimental setup is shown in Figure 1.9, and the main features include a striker bar that delivers the impact, an incident bar that transmits the stress wave, the specimen, and the transmitted bar. The strain in the incident and transmitted bars is measured through the use of electrical resistance strain gages located in the middle of the incident and transmitted bars. When the test is performed, the gas tank launches the striker bar, which impacts the incident bar generating a stress wave. The wave travels down steel bar with a wave velocity of c_{EL} , until it reaches the incident bar / specimen interface. When the wave reaches the interface, part of the compressive wave is transmitted and part of the wave is reflected back, the portion that is reflected back is a tensile wave and considered to be propagating in the negative direction. The compressive wave that was transmitted continues to travel through the sample until it reaches the specimen / transmitted bar interface at which point a portion of the wave is transmitted and a portion reflected. The transmitted compressive wave is read at the transmitted bar strain gage, while the incident and reflected waves are collected at the incident bar strain

gage. With that conceptual framework in mind, further details regarding the use of a Kolsky bar system can be discussed.

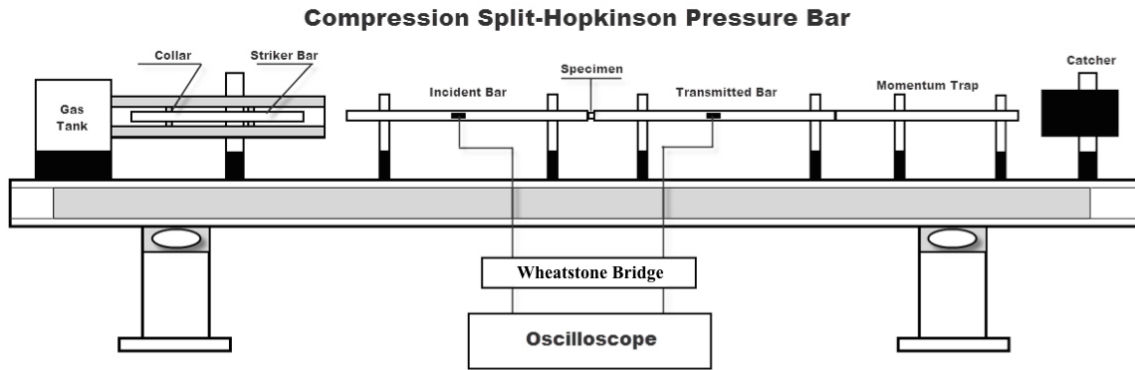


Figure 1.9: Schematic representation of a Split-Hopkinson Pressure Bar (SHPB) or Kolsky bar.

The stress wave velocity is important because an average stress condition within the specimen is used during data analysis, and an average stress within the specimen is only reached after approximately three reverberations, as found by Davies and Hunter [138]. Since plastic deformation is taking place in the sample during loading, it is more

appropriate to use the plastic wave velocity $c_{PL} = \sqrt{\frac{d\sigma / d\varepsilon}{\rho}}$ which is approximately 10%

of the elastic wave velocity. Using the plastic wave velocity and the sample dimensions it is possible to determine when a uniform stress condition will be reached in the specimen.

It is a result of this behavior that stress measurements are made at 4% strain in the dynamic samples, as will be seen in Chapter 3. The ability to relate the stresses in the bar to the sample was discovered by Hopkinson who determined that as long as the pressure bars (the incident and transmitted bars) remain elastic, the displacements in the

bar are directly related to the stresses within the bar [136]. It was later expanded upon by Kolsky who found that if a split-bar method was used that placed the specimen between the two pressure bars, the stress and strain within the specimen are then related to the displacements in the pressure bars. It is this relationship that allows for strains that are measured in the pressure bars to be related to the stress and strain in the sample. The mathematical analysis is presented in the next subsection.

1.4.2 Calculation of Sample Stress and Strain

First, two assumptions must be made for this analysis to be valid, that the stress wave is one-dimensional, and that the specimen deforms uniformly. Also, note that in this analysis, the wave is assumed to travel from left to right, in keeping with the scenario presented in Fig. 1.9. With those assumptions made, it is now possible to relate the strain gage measurements to the specimen stress – strain behavior [139]. Starting from basic wave theory, the solution to the wave equation is known:

$$\frac{\partial^2 u}{\partial x^2} = \frac{1}{c_b^2} \frac{\partial^2 u}{\partial t^2} \quad 1.15$$

which can also be written as:

$$u = f(x + c_b t) + g(x - c_b t) = u_i + u_r \quad 1.16$$

Giving the displacement of the incident bar, where u is the displacement of the sample, f and g are functions describing the incident and reflected waves, and c_b is the longitudinal

wave velocity in the incident and transmitted bar material. Since 1-D strain is just the change in displacement over position, is given by:

$$\varepsilon = \frac{\partial u}{\partial x} \quad 1.17$$

Then if Eq. 1.16 is differentiated with respect to x , the strain in the incident pressure bar would be:

$$\varepsilon = f' + g' = \varepsilon_i + \varepsilon_r \quad 1.18$$

Taking Eq. 1.16 and differentiating with respect to time then yields:

$$\dot{u} = c_b(f' - g') = c_b(\varepsilon_i - \varepsilon_r) \quad 1.19$$

Eq. 1.19 provides the wave velocity at the incident bar-specimen interface. The time derivative of the displacement in the transmitted bar is then:

$$\begin{aligned} u_t &= h(x + c_b t) \\ \dot{u}_t &= c_b h' = c_b \varepsilon_t \end{aligned} \quad 1.20$$

Taking u_1 and u_2 to be the displacements of the incident bar-specimen and specimen-transmitted bar interfaces respectively, and L as the instantaneous length of the specimen, the strain rate in the specimen is then given by:

$$\dot{\epsilon} = \frac{(\dot{u}_1 - \dot{u}_2)}{L} \quad 1.21$$

Substituting Eqs. 1.19 and 1.20 into Eq. 1.21:

$$\dot{\epsilon} = \frac{c_b}{L} (\epsilon_i - \epsilon_r - \epsilon_t) \quad 1.22$$

As stated earlier, an average stress state within the sample is assumed, so the following gives the average stress on the specimen:

$$\sigma = \frac{F_1(t) + F_2(t)}{2A} \quad 1.23$$

In Eq. 1.23, F_1 and F_2 are the forces at the incident bar-specimen and specimen-transmitted bar interfaces respectively, and A is the instantaneous cross-sectional area of the specimen. By definition, the forces are:

$$\begin{aligned} F_1 &= EA_b(\epsilon_i + \epsilon_r) \\ F_2 &= EA_b\epsilon_t \end{aligned} \quad 1.24$$

E is the Young's modulus in the pressure bar, and A_b is the cross-sectional area of the pressure bar. Again, because the stress in the specimen is assumed to be constant after three reverberations, a force equilibrium can be taken which yields:

$$\begin{aligned} F_1 &= F_2 \\ \varepsilon_t &= \varepsilon_i + \varepsilon_r \end{aligned} \tag{1.25}$$

Plugging the result of Eq. 1.25 into Eq. 1.22 for the strain and Eq. 1.23 for the stress, the strain and stress in the specimen is given by:

$$\begin{aligned} \dot{\varepsilon} &= -\frac{2c_b}{L} \varepsilon_r \\ \sigma &= \frac{EA_b \varepsilon_t}{A} \end{aligned} \tag{1.26}$$

In this manner the stress-strain behavior of the specimen can be found using strain signals in the incident and transmitted pressure bars.

CHAPTER 2: EXPERIMENTAL METHODS

This chapter will cover the details of the processes used to produce the materials under investigation as well as the microstructural and mechanical characterization methods. Regarding the materials processing, cryomilling and its effects on the microstructure of the Al 5083 alloy will be discussed in detail, in addition to the parameters used. Two metal matrix composites were tested in this investigation, Al 5083 reinforced with ~40 nm boron carbide particulates (Al-B₄C-1), and Al 5083 reinforced with ~500 nm boron carbide particulates (Al-B₄C-2). Microstructural characterization techniques in the form of scanning electron microscopy (SEM) and transmission electron microscopy (TEM) were used to examine the as-received and post-loading conditions. Mechanical testing was performed using quasi-static and dynamic compression techniques as well as through the use of a nanoindenter. Finally, the elevated temperature setup used to test the materials under high strain rate compression will be discussed.

2.1 Materials Processing

My dissertation research has focused on the mechanical properties, elevated temperature response, and influence of reinforcement size of three aluminum-based materials. All three materials were developed and produced by Dr. Lavernia's research group at the University of California, Davis. The materials processing was solely the work of Dr. Lavernia's group and not my own.

2.1.1 Cryomilling

Cryomilling is a powder metallurgy process that takes conventional high energy ball milling and modifies the equipment and procedure so that the process takes place at cryogenic temperatures, usually with the use of liquid nitrogen or some other low temperature media [49, 140]. While early mechanical alloying (MA) processes involved the use of elemental powders to form the desired alloy, most current methods use master alloy powders since the elemental metals are much more reactive which is not conducive to good interfacial bonding. When milling is performed at cryogenic temperatures, it prevents the metal from recrystallizing while still imposing large plastic deformation resulting in a refined internal structure [141]. In the case of aluminum, when cryomilling is performed using liquid nitrogen, very fine secondary particles of AlN on the order of 10 nm are formed in addition to the refinement of the metal grain structure [142]. These nanoscale particles help “pin” grain boundaries in the form of Zener pinning [143], where the particles exert a pinning force against the migration of the grain boundary. When the forces are in equilibrium, the following expression for the pinning pressure due to all particles is obtained [144, 145]:

$$P_z = \frac{3\phi\gamma}{2r} \quad 2.1$$

where γ is the grain boundary free energy, P_z is the pinning pressure, ϕ is the volume fraction of second-phase particles and r is the average particle radius. This pinning force allows the cryomilled aluminum to maintain a nanostructured grain structure while proceeding through the elevated temperature consolidation steps. Dr. Lavernia’s research

group has used cryomilling extensively in the production of Al 5083 alloys and composites and have reported on the effects of modifying milling parameters such as volume of reinforcement material, process control agent composition, and milling time on microstructural development [33, 89, 146-148].

2.1.2 Aluminum Alloy 5083 and Boron Carbide Composites

Gas atomized aluminum Al 5083 (Valimet, Inc., Stockton, CA), with a -325 mesh particle size, and material composition of (Al-4.5 Mg-0.57 Mn-0.25 Fe in wt. %) functioned as the master alloying powder (Table 2.1). The aluminum powder was blended with 5 vol.% B₄C powder with average particle sizes of ~40 nm (fabricated by U.S. Army Armament Research, Development and Engineering Center, Picatinny, NJ) or ~500 nm (HD20 B₄C fabricated by HC Stark, Newton, MA) in a V-blender for 12 hours to homogenize the powders.

Table 2.1: Wt % of constituent elements in Al 5083 alloy

Material	Al	Mg	Mn	Fe
Al 5083	94.68	4.5	0.57	0.25

The blended powders were then cryomilled for 12 hours in liquid nitrogen in a modified Union Process 1S Svevari attritor with a rotational velocity of 180 RPM, a ball-to-powder ratio of 30:1 and 0.2 wt. % stearic acid (CH₃(CH₂)₁₆CO₂H) as a surfactant. The cryomilled powders were then hot-vacuum degassed at 500 °C for 20 hours to form a green compact. The compact then underwent dual mode dynamic (DMD) forging twice at 400 °C. DMD forging is different from the common consolidation technique of hot-isostatic pressing (HIP) in that the pressure during forming is uniaxial and not isostatic,

and the mechanism is shown in Fig. 2.1 [149]. The Al-MMC with 40 nm B₄C particles is designated as Al- B₄C -1, and the Al-MMC with 500 nm B₄C particles is designated as Al- B₄C -2. A counterpart of ultra-fine grained Al 5083 alloy without reinforcing phase (NR-AL) was fabricated through an equivalent processing route and characterized as a control. Sample identifications (IDs) and material conditions are summarized in Table 2.2 and further details regarding the cryomilling process in relation to Al 5083 materials can be found in previous publications [150, 151].

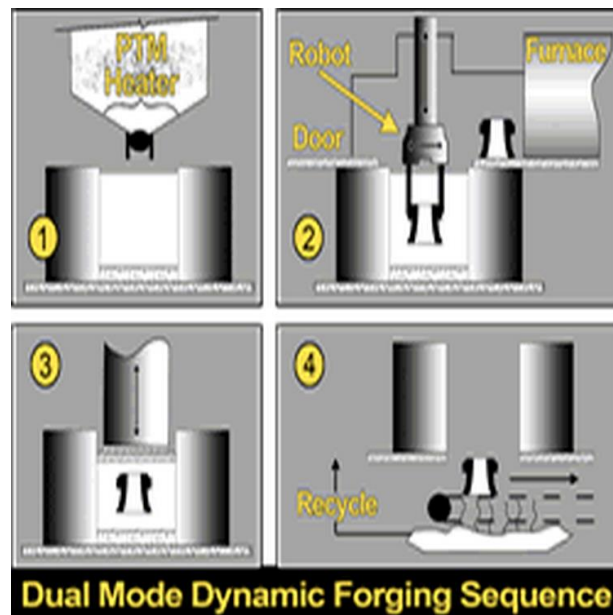


Figure 2.1: Schematic representation of the steps involved in dual mode dynamic (DMD) forging [149].

Table 2.2: Summary of material conditions and sample IDs for the aluminum MMCs used in this investigation.

Material	Boron Carbide Reinforcement Size (nm)
Al-B ₄ C-1	~ 40
Al-B ₄ C-2	~ 500
NR-AL	N/A

2.2 Microstructural Characterization

Microstructural analysis of the pre- and post-loading samples from both the room temperature and elevated temperature tests was performed to characterize the changes that occurred during deformation. Details of the microstructure were evaluated using a JEOL-2100 (LaB₆ gun) transmission electron microscope operated at 200 kV. TEM samples were prepared by first cutting a 0.5 mm-thick section of the desired sample for mechanical polishing. The 0.5 mm slice was then formed into a 3 mm diameter disk using a Gatan sample cutter, and mounted to a 656 disc grinder (Gatan) to mechanically thin the sample to ~70 μm. The sample was then subjected to further thinning on a 656 dimple grinder (Gatan), before finally being transferred to a Gatan 691 precision ion polisher system (PIPs) for final thinning to electron transparency. TEM bright field and dark field images were used in conjunction with ImageJ to assess the grain size and microstructural features before and after dynamic and quasi-static testing. Twenty to thirty micrographs were observed for each sample to obtain an appropriate sampling size of grains.

Surface analysis of the samples in both the as-received and post-loading conditions was performed using optical microscopy and SEM. SEM analysis was carried out on a JEOL JSM 6480 SEM operated between 10 and 20 kV. Due to the sub-micron characteristic features size of the materials being studied the optical images did not yield much relevant information and only the SEM images will be presented. The scanning electron micrographs reveal evidence about the formation, or lack thereof, of adiabatic shear bands during deformation, as well as provide information regarding the heat generated during ASB formation.

2.3 Mechanical Testing

Quasi-static tests were performed on all samples using an MTS Landmark Servo Hydraulic Test System at a constant strain rate of $\sim 1 \times 10^{-3} \text{ s}^{-1}$. The system is equipped with self-alignment features to maintain parallelism and perpendicularity during testing. The dimensions of the specimens for quasi-static testing were $\sim 2.5 \times 2.5 \times 5 \text{ mm}$. The loading faces and sides of the samples were polished before testing to ensure even contact and to assist in post-loading examination. Loading surfaces were lubricated to reduce friction interactions between the sample and the loading platens (MTS 643 Compression Platens) to eliminate barreling. The strain rate was controlled via modulation of the crosshead speed.

Dynamic (high strain rate) tests were performed using the Kolsky bar, also known as a split-Hopkinson pressure bar, system shown in Fig. 2.2. The technical specifications regarding its use, data processing, and setup were provided in the previous section. The samples prepared for high strain rate testing measured $\sim 2.5 \times 2.5 \times 2.0 \text{ mm}$, with the loading direction parallel to the 2 mm dimension (the gage section). Strain rates ranged from $\sim 4000 \text{ s}^{-1}$ to $\sim 5000 \text{ s}^{-1}$ for the Al-MMCs and $\sim 6000 \text{ s}^{-1}$ to $\sim 7000 \text{ s}^{-1}$ for the unreinforced Al 5083 with no prescribed strain in either condition. The higher imposed strain rate for the unreinforced Al samples was a result of using the same loading pressure as was used for the Al-MMCs.



Figure 2.2: Picture of the Kolsky bar, high strain rate compression test setup used in this investigation.

An instrumented nanoindenter (Agilent G-200) was used to evaluate hardness values, as well as to derive the strain rate sensitivity (SRS). A series of 10 indents were performed for each condition in order to illuminate any statistically relevant trends. 20 indents consisting of three strain rates 0.05 , 0.007 , and 0.001 s^{-1} were performed with an initial indentation depth of 1100 nm , and a final depth of 2000 nm on the as-received samples to obtain the SRS. It is assumed that strain rate hardening follows the popular power law, and as such, SRS is the slope of the double logarithmic plot of hardness versus the indentation strain rate. Details for using nanoindentation to derive SRS values can be found in Ref. [152].

Elevated temperature compression tests were performed at dynamic strain rates by adding an electric resistive heater to the Kolsky bar setup shown above. The heater is

shown in Fig. 2.3, where a pair of holes allows the sample and bars to pass through the heater, and insulation is used to maintain the desired temperature. A thermoelectric control system is used to monitor the temperature inside the furnace and provide feedback to maintain the temperature within 5 °C of the desired testing temperature. Once the desired temperature was reached, the sample and bars were inserted into the furnace and allowed to reach a homogenous temperature over a 5-minute period. The testing procedure for the dynamic test then proceeded as previously described.

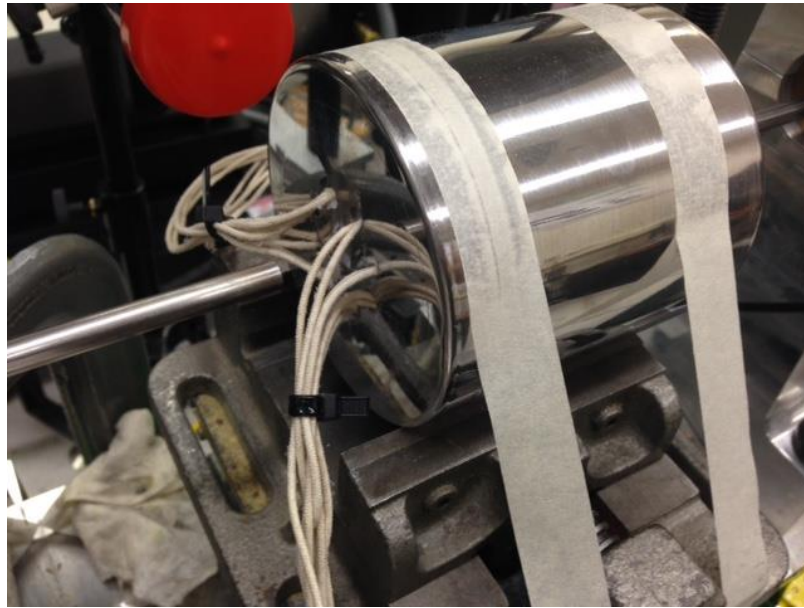


Figure 2.3: Picture of the electric furnace used to heat the dynamic compression samples in the elevated temperatures tests.

CHAPTER 3: MICROSTRUCTURE AND MECHANICAL PROPERTIES OF AL 5083 COMPOSITES

3.1 Introduction

The use of high performance aluminum alloys in the aerospace and automotive industries has already been discussed, however there is another industry that also has need of high strength aluminum alloys and composites, the defense industry [153]. Favorable properties for an armor material generally fall within three categories, high strength at impact velocities, adequate toughness and low weight [147]. Depending on the application in question, e.g. vehicular vs personnel armor, different aspects are of greater importance, for example weight may be of less concern when applied to a vehicle. Most current armor systems approach the problem by using multiple layers of materials that address one aspect of the incoming projectile [154]. One layer may be a ceramic with high strength, followed by a layer of aramid fibers in a polymer matrix, then backed with a metal plate for force distribution [78, 155]. The limiting factor of such a system is the weight of each component; as a result it would be very beneficial if two layers could be combined without loss of performance. Such attempts are currently being made with UFG and nanostructured aluminum composites due to their low weight and high strength that is unattainable with conventionally structured aluminum alloys. In the area of ceramic reinforced aluminum composites, the most prominent reinforcements are SiC and B₄C [32, 147, 156].

One of the materials that has generated considerable interest, and been the focus of extensive study is a tri-modal Al 5083 composite, reinforced with micron-sized B₄C [33, 105, 146, 157, 158]. This tri-modal composite was first produced and reported by Ye et al. [89] and was an extension of earlier work focused on a bi-modal Al 5083 alloy [61]. In both cases the microstructure consisted of a bi-modal distribution of Al 5083 grains, with grains in the UFG regime and coarse grains around one micrometer. Additionally, both were formed through powder processing methods and underwent extrusion after consolidation resulting in strong texture and additional plastic deformation. In the case of the tri-modal aluminum composite, the boron carbide reinforcement was on the scale of 4 – 7 μm [157]. Boron carbide is an attractive reinforcement material due to its good interfacial strength with aluminum [80, 148, 157], low density of 2.52 g/cm³ [159], high melting point of 2445 °C and elastic modulus of 460 GPa [85] which is close to diamond. I have given specific details of these materials because they were an inspiration for the composites under investigation in my dissertation, and to highlight some of the differences between the materials. The composites in my study have an entirely UFG Al matrix, B₄C reinforcements on the nanoscale, either 40-50 nm or 500 nm, and did not undergo any plastic work such as rolling or extrusion after consolidation. The mechanical performance of these nanostructured Al MMCs will be compared to some other Al MMCs from the literature in the discussion.

3.2 Experimental Results

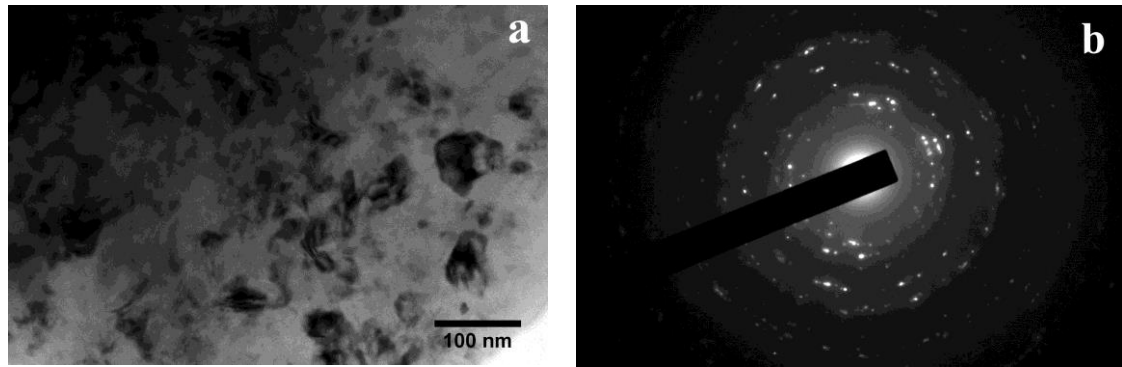


Figure 3.1: Representative TEM bright field image of Al-B₄C-2 (a) with the corresponding dark field image (b) demonstrating the ring-like pattern indicative of a polycrystalline sample. While the ring-like pattern is evident in (b), there are a large number of discrete spots due to strong diffraction of a few grains.

3.2.1 Microstructural Analysis

The microstructures of Al-B₄C-1, Al-B₄C-2, and NR-AL were analyzed using a combination of SEM and TEM techniques. A representative TEM bright field (BF) image is shown in Fig. 3.1 (a) for Al-B₄C-2, along with the selected area electron diffraction (SAED) pattern (Fig. 3.1 (b)). The SAED has a ring-like pattern indicating a polycrystalline Al matrix grain structure, along with a large number of discrete diffraction spots from oriented grains. The bright field image in Fig. 3.2 (a) is from Al-B₄C-1 and shows grains with a large number of dislocations. Fig. 3.2 (c) shows the corresponding dark field image with the diffraction from the {012} plane of B₄C highlighted, as shown in Fig. 3.2 (b). Analysis of the boron carbide reinforcement indicated that particles were on the order of 40 – 50 nm in diameter.

The microstructure of the unreinforced Al alloy was characterized, and some representative micrographs are provided in Fig. 3.3 The microstructure for the post-

loading NR-AL sample is shown in Fig. 3.3 (a) and is indicative of the larger yet submicron grains that are present in the NR-AL sample both pre- and post-loading, the provided arrows highlight grain boundaries. Figs. 3.3 (b) and 3.3 (d) indicate the second-phase particles that presumably formed during cryomilling and are on the order of 10 nm. The diffraction spots circled in Fig. 3.3 (c) indicate the diffraction spots that were highlighted to produce the dark field image. Though close to the aluminum diffraction ring the spots lie just outside it, and the small size of the particles is below the limits of the grain refinement performed on the samples. Based on the d-spacing and the findings of others working on cryomilled Al in liquid nitrogen [94, 146] it is believed these are AlN particles.

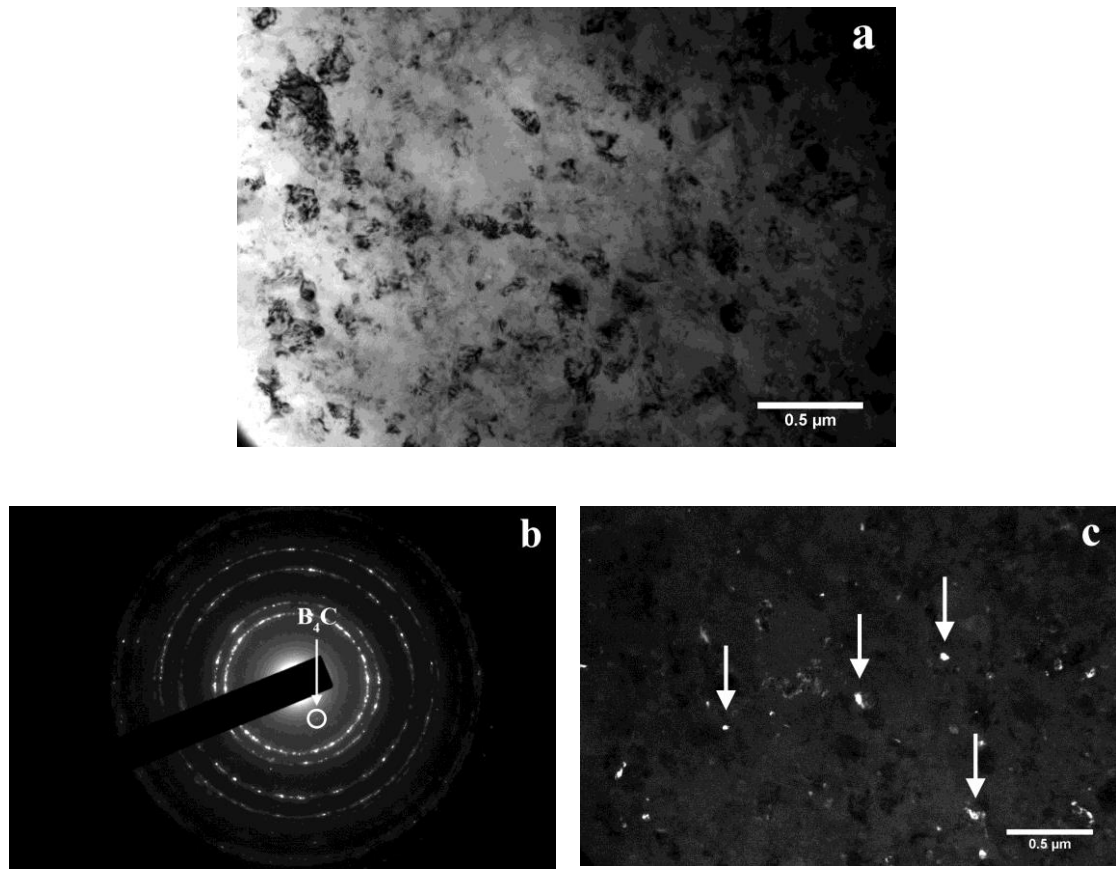


Figure 3.2: TEM images of Al-B₄C-1; the bright field image (a) shows that grains are highly deformed with many dislocations, and without well-defined grain boundaries. The SAED (b) indicates the B₄C diffraction spot isolated to produce the dark field image (c). The reinforcing particles are found to be on the order of 40 – 50 nm.

Transmission electron micrographs were used to analyze grain sizes of the three samples and the grain size histograms are shown in Fig. 3.4. After an analysis of 129 grains from the TEM images, the histogram of the grain size of the Al-B₄C-1 matrix is shown in Fig. 3.4 (a) where the average value was found to be 154 nm. Similar analyses were performed on the other two materials (Figs. 3.4 (b-c)) and the average grain sizes were found to be 141 nm for Al-B₄C-2 and 218 nm for NR-AL. These grain sizes agree

well with those provided in [157], where the average grain size of the UFG Al matrix with micron sized boron carbide reinforcement was found to be 156 nm.

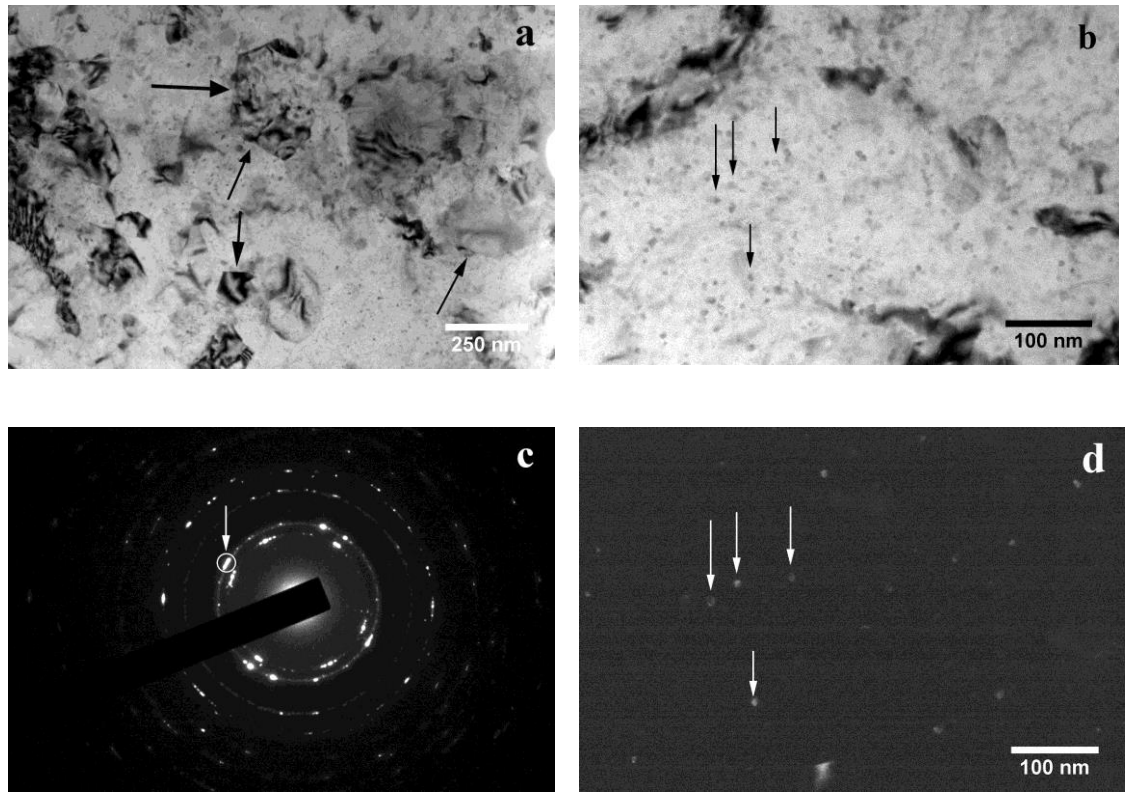


Figure 3.3: The microstructure of NR-AL post-loading (a) exhibits grains on the order of 200 – 250 nm, approximately 100 nm larger than either composite sample. Intermetallic particles formed during cryomilling are highlighted in the bright field (b) and dark field (d). Analysis of the particles reveals that they are approximately 10 nm in diameter. Their size combined with a d-spacing similar to that of aluminum (c) makes it likely that these are AlN particles formed during cryomilling, such dispersoids have been found previously [160].

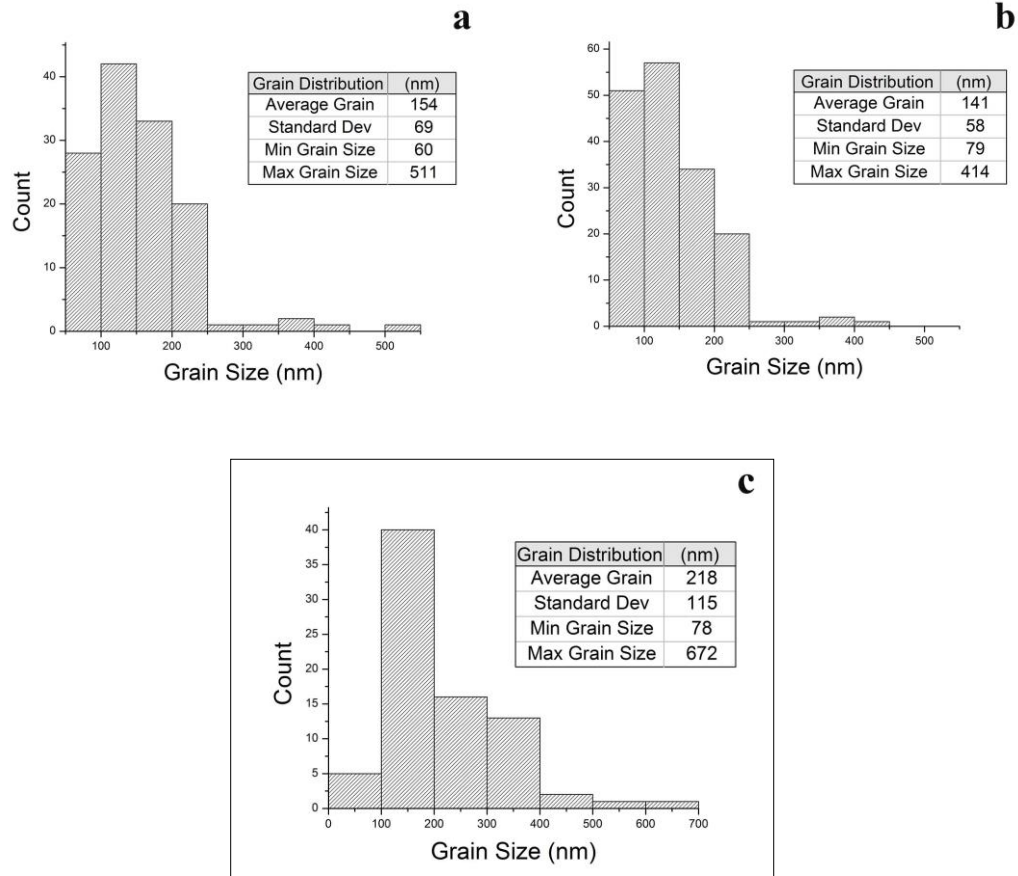


Figure 3.4: Grain size distribution of matrix grains in Al-B₄C-1 (a), Al-B₄C-2 (b), and NR-AL (c). The distribution and average grain size exhibited in (a) and (b) closely match those from ref. [157], while the average and max grain size of NR-AL indicates that some grain growth likely occurred during processing.

3.2.2 Dynamic and Quasi-static Compression Tests

The following section presents the results of the quasi-static (QS) and dynamic (DY) compression tests for the three aluminum-based materials. Fig. 3.5 shows the representative quasi-static (a) ($\sim 1.0 \times 10^{-3} \text{ s}^{-1}$) and dynamic (b) ($\sim 4.0 \times 10^3 \text{ s}^{-1}$) compression curves for Al-B₄C-1, Al-B₄C-2, and NR-AL. The yield strengths for the composite samples under both quasi-static and dynamic conditions are similar with yield occurring around 850 – 900 MPa. These values are in contrast to the unreinforced alloy

which exhibits a yield strength around 600 MPa, indicating a 30% improvement in yield strength for the Al composites. Since all three samples underwent the same powder processing method, the difference in mechanical properties should be due to the inclusion of the boron carbide particles, and their effect on the microstructure. The detailed discussion of the strengthening mechanism is deferred to a later section.

Comparison of the strain experienced by the composites also exhibits similarities, with unloading occurring around 20% true strain under dynamic compression for Al-B₄C-1, and slightly later for Al-B₄C-2. Under quasi-static loading Al-B₄C-1 and Al-B₄C-2 experienced failure around 20% true strain before reaching the prescribed strain of 30%. The unreinforced alloy did not form cracks under dynamic loading, while the dynamically loaded composite samples started to develop shear localization and subsequently cracks that can be seen under SEM investigation (Fig. 3.6). The stress drop at the end of the curves in Fig. 3.5 (b) is due to unloading of the samples, and not necessarily failure of the material.

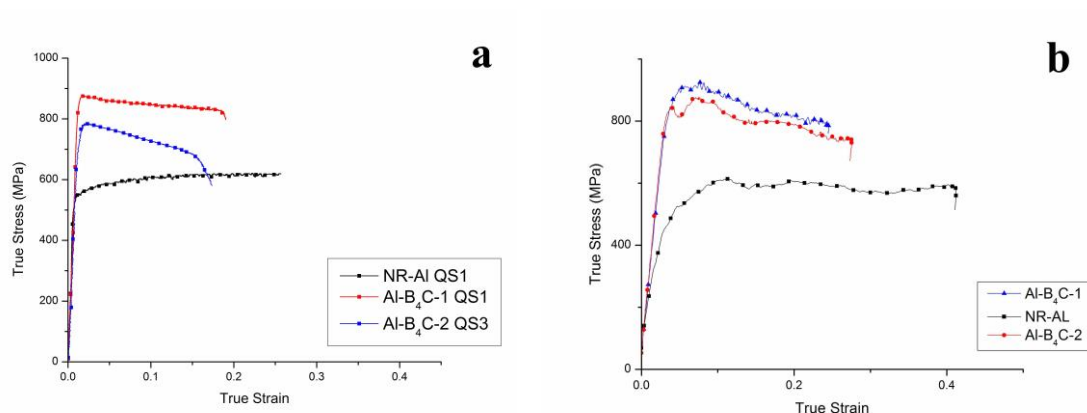


Figure 3.5: Representative true stress – true strain results for quasi-static (a) and dynamic (b) compression of the aluminum alloy and composites. The non-reinforced alloy exhibits strain hardening at quasi-static and dynamic strain rates though the strain hardening is much reduced at dynamic rates due to thermal softening. Composite samples undergo strain softening at both strain rates, though softening is greatly diminished for Al-B₄C-1 during quasi-static testing and may be considered elastic-nearly perfect plastic. Quasi-static tests were stopped at a prescribed strain of 0.3 (~30%), and the composite samples failed during testing. Dynamic tests had no prescribed strain and the stress drop at the end is due to sample unloading, no failure was observed.

Note: Al-B₄C-2 quasi-static data provided by Henry Yang of [161] at UC Davis

The unreinforced aluminum alloy consistently underwent comparable or increased plasticity without failure as compared to both Al-B₄C-1 and Al-B₄C-2. Under quasi-static compression NR-AL underwent 25% true strain without failure, while dynamic loading led to a final strain of 40% and though the sample still did not fail, it underwent significant inhomogeneous deformation as can be seen in Fig. 3.6 (a). The plastic behavior of the samples differed as well, with NR-AL undergoing moderate, and minor strain hardening during quasi-static and dynamic loading respectively while the composites underwent strain softening during dynamic deformation. During quasi-static

deformation however, Al-B₄C-1 exhibited an elastic-nearly perfect plastic response after yielding (Fig. 3.5 (a)) with slight yet distinct flow softening. Al-B₄C-2 on the other hand exhibited strain softening consistent with its dynamic softening behavior.

Shear banding-like behavior was observed in the two composite materials, though only under dynamic conditions. In both MMCs the shear bands were localized to two conjugate shear planes as highlighted in Fig. 3.6 (c). Both localized plasticity and cracking were observed along the shear bands, with one sample often exhibiting both forms of deformation. Due to the localized nature of the shear bands and the time scale of their formation, they can be classified as adiabatic shear bands [111]. Under quasi-static loading, Al-B₄C-1 fractured along the plane of maximum shear stress, however no localized deformation was observed, and the fracture appears to be of semi-brittle type as indicated by Fig. 3.7.

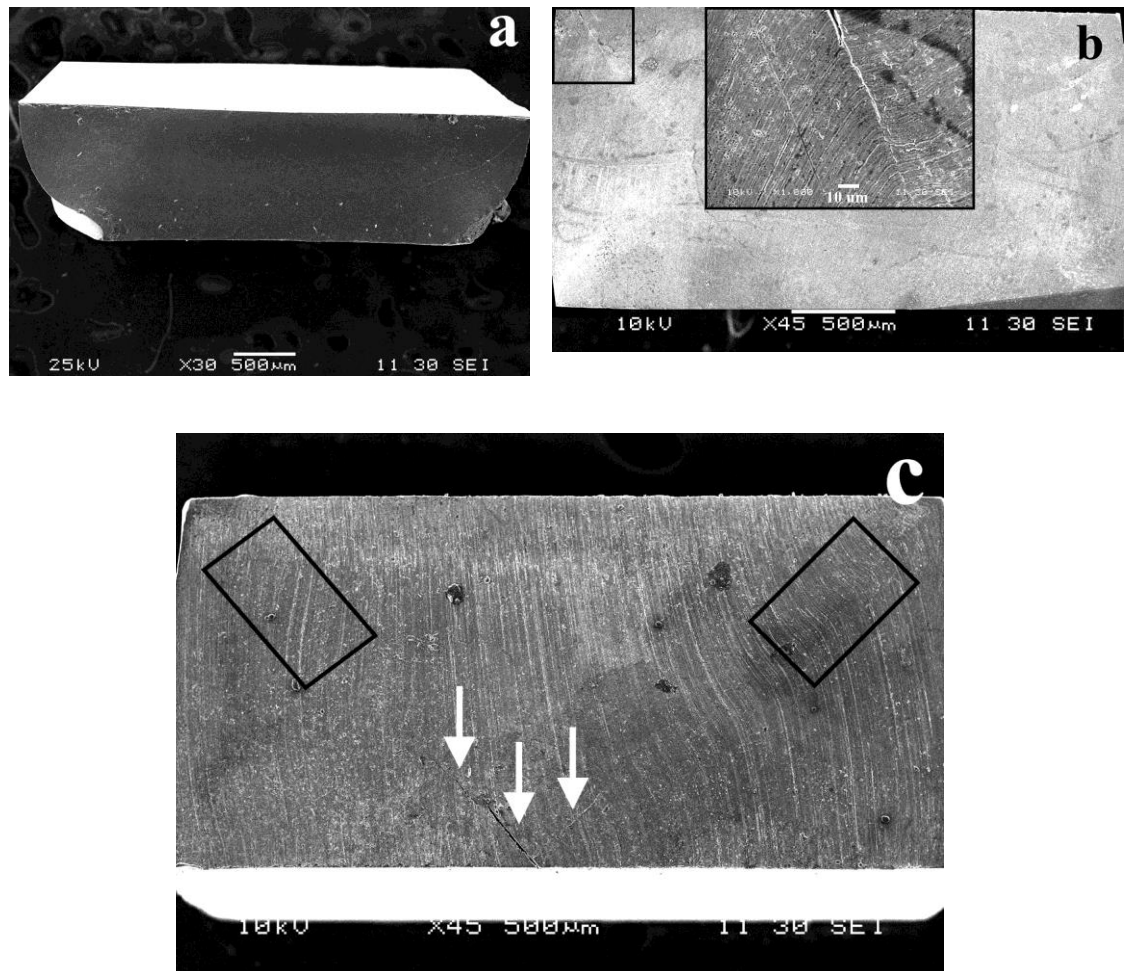


Figure 3.6: SEM images of (a) NR-AL, (b) Al-B₄C-1 and (c) Al-B₄C-2 after dynamic compression. No localized shearing is observed in NR-AL, while both composites exhibit localized plasticity along shear bands. Enlarged inset in (b) shows significant localized shear and crack formation. Highlighted sections of (c) indicate the conjugate shear planes that develop during dynamic deformation.

3.2.3 Nanoindentation

Nanoindentation hardness and strain-rate-jump tests were performed on the three aluminum-based materials to provide further insight into their mechanical properties. The Vickers hardness test was used to provide additional confirmation of the yield strengths

found for Al-B₄C-1, Al-B₄C-2, and NR-AL with values of 938 MPa, 909 MPa, and 644 MPa respectively. These values compare favorably with those found during compression tests, as can be seen in Table 3.1. The Vickers hardness values were converted to the yield strength through the Tabor law, and the most commonly used form is $VHN=3\sigma_y$, and VHN is the Vickers hardness number.

Strain-rate-jump tests were subsequently performed at increasing strain rates, to determine the influence of strain rate on material performance. The results are shown in Fig. 3.8, which is the double logarithmic plot of nanoindentation hardness versus the indentation strain rate. It was found that the SRS values of the materials were very similar, all existing within an order of magnitude, though the SRS of Al-B₄C-1 and NR-AL were slightly higher than that of Al-B₄C-2. It should be noted that in Fig. 3.8, the high strain rate data points from Kolsky bar experiments are also included. The effect of this practice will be discussed in the next section.

Table 3.1: Mechanical properties of the aluminum alloys and composites with coarse-grained Al5083 included for comparison. The coarse-grained aluminum value [94] is used in the calculation of the Hall-Petch strengthening.

Material	QS 0.2% Stress (MPa)	DY 5% Offset (MPa)	NI Hardness/3 (MPa)	SRS
Al-B ₄ C-1	860 ± 15	900 ± 10	938 ± 23	0.0026
Al-B ₄ C-2	-	850 ± 15	909 ± 16	0.0018
NR-Al	572 ± 6	575 ± 23	645 ± 29	0.0029
CG-Al	124	-	-	-

Notes:

Al5083-B4C-1: B₄C average particle size: ~40 nm;

Al5083-B4C-2: B₄C average particle size: ~500 nm;

NR-Al5083: Non-reinforced Al5083 processed by cryomilling and consolidation;

CG-Al5083: Coarse-grained Al5083 alloy;

NI Hardness/3: Nanoindentation divided by a constraint factor of 3 in the sense of Tabor rule;

SRS: Strain rate sensitivity following power law rate dependence.

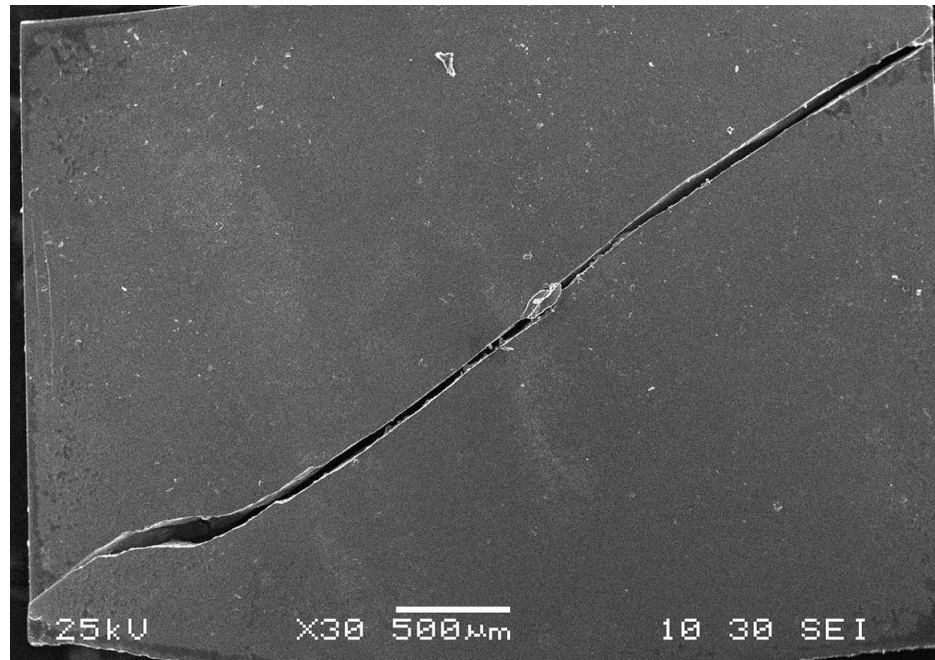


Figure 3.7: SEM image of quasi-statically loaded Al-B₄C-1 exhibiting the brittle fracture the sample underwent without developing the localized plasticity observed in the dynamically deformed composite.

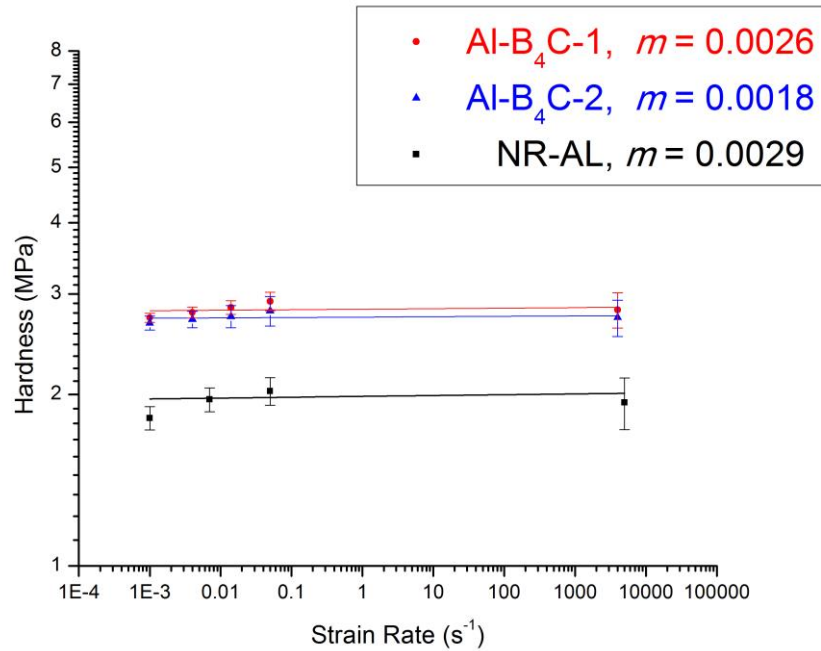


Figure 3.8: Strain rate sensitivity of the aluminum alloy and composites indicating low rate dependence. The high strain rate data was collected from dynamic compression, while the low strain rate data points were a result of strain-rate jump tests performed during nanoindentation.

3.3 Discussion

First of all, it should be noted that the three materials in this study, Al-B₄C-1, Al-B₄C-2 and NR-AL exhibit some similarities in their microstructure as a result of having undergone the same cryomilling and DMD (dual mode dynamic) forging processes. An important feature of the microstructure is grain size, as grain size refinement is the single largest contributor to the strength of the materials, which follows the Hall-Petch relationship [162]. In addition to the elements in the alloy (4 – 5% magnesium, ~ 0.5% manganese and trace iron) the cryomilling process also introduces oxygen and nitrogen that can react with other elements to create secondary nitrides within the matrix [105].

These dispersoids interact with dislocations in the samples leading to additional strengthening.

In order to account for the transfer of load to the boron carbide, a modified shear lag model was used. The differences in the coefficient of thermal expansion and elastic modulus between the matrix and reinforcement and their role in dislocation formation is discussed in the following sections. It has been predicted that decreasing the size of reinforcements leads to an increase in dislocation density [163], so it would be expected that Al-B₄C-1 and Al-B₄C-2 would contain more dislocations overall, even if there are fewer dislocations around each particle, as compared to composites with larger micron-sized reinforcements. Additionally, the Orowan strengthening resulting from the reinforcing particles and second phase nitrides is considered, with the dislocation strengthening treated in a quadratic format. Finally, the influence of the boron carbide reinforcement and processing method on the plastic deformation of the samples is discussed. In particular, the occurrence of adiabatic shear bands in the composite will be dealt with in detail in the context of adiabatic shear band toughness.

3.3.1 Grain Size Strengthening via Hall-Petch Effect

Cryomilling is used to reduce the original Al 5083 powder particles down to 100 – 200 nm grains after consolidation. The Hall-Petch relationship dictates the strengthening of the ultrafine-grain aluminum matrix, which accounts for the majority of the final strength of the composite. The Hall-Petch relationship states that the yield strength scales linearly with the inverse square root of the grain size, and is in the form [105],

$$\Delta\sigma_{HP} = \sigma_0 + k_y d^{-1/2} \quad 3.1$$

where $\Delta\sigma_{HP}$ is the yield strength improvement after taking into account grain size strengthening; σ_0 is the frictional yield strength (lattice friction, or the yield strength of coarse-grain material), d is the grain size, and k_y is a constant of .22 MPa \sqrt{m} [164] for Al 5083. In the case of Al5083 σ_0 is ~124 MPa which includes the strengthening from solid solutes [44], the average grain size was 154 nm for Al-B₄C-1, 141 nm for Al-B₄C-2 and 218 nm for NR-AL. Using these values, a grain refinement-based yield strength improvement of $\Delta\sigma_{HP} = 560MPa$ was calculated for the Al-B₄C-1, $586MPa$ for Al-B₄C-2, and $471MPa$ for NR-AL. Compared to the strength values of the three materials listed in Table 2, all the Hall-Petch contributions fall short of the experimental yield strength values, suggesting that additional strengthening mechanisms should be considered to reconcile the experimental results and theoretical predictions.

3.3.2 Composite Strengthening

Orowan strengthening is either not significant or is entirely invalid for micron-sized particulate composites due to the large interparticle spacing [75] and their large size in comparison to the matrix grains. So while Al-B₄C-2 with B₄C size ~500 nm will not undergo significant Orowan strengthening from its reinforcement particles, Al-B₄C-1 will, as the 40 nm particles are smaller than the average matrix grain size (~154 nm). Additionally, the microstructure of these cryomilled materials, both the alloy and composites, contain secondary particles such as nitrides that also provide Orowan strengthening [94, 105]. The theoretical value of the Orowan strengthening can be estimated by:

$$\Delta\sigma_{or} = \frac{1.25G_m b \ln(\bar{d}/b)}{\pi\sqrt{1-\nu} \bar{\lambda}} \quad 3.2$$

where $\Delta\sigma_{or}$ is the yield strength increase due to Orowan strengthening, G_m is the shear modulus of the matrix taken as 27 GPa [105], b is the Burgers vector of the matrix, and ν is Poisson's ratio of 0.33. The mean dispersoid size, \bar{d} and the mean inter-particle distance $\bar{\lambda}$ are given by $\bar{d} = \sqrt{2/3} \cdot d$ and $\bar{\lambda} = \bar{d}(\sqrt{\pi/4V_p} - 1)$ respectively where d is the particle size and V_p is the volume fraction of the B₄C particulate or nitride. In Al-B₄C-1 the value of d was taken as 40 nm, and V_p as 5% as indicated from the processing parameters, while the nitrides were estimated as 10 nm and V_p as 0.5% [94]. To account for the load transferred to the reinforcing particles Nardone and Prewo's modified shear lag model was used, with the particles considered to be equiaxed yielding [82, 165],

$$\Delta\sigma_l = \sigma_m (0.5V_p) \quad 3.3$$

where V_p is the volume fraction of the reinforcing particles, and σ_m is the matrix yield stress.

The final strengthening mechanisms to consider are those that result from a difference in material parameters between the matrix and reinforcement, namely elastic modulus and coefficient of thermal expansion differences. Recent discoveries relating to UFG and NC Al MMCs [166] have indicated that CTE mismatch does not provide a

significant contribution to material strength. Taken in conjunction with Lloyd's analysis that the critical CTE misfit strain cannot generally be reached for particles <100 nm [167] it was determined that CTE mismatch induced dislocations should be excluded.

Geometrically necessary dislocations due to elastic modulus mismatch however still play a role, and can be estimated using the equation [106]:

$$\Delta\sigma_{GND} = kG_m b \sqrt{\frac{8V_p \varepsilon_y}{bd}} \quad 3.4$$

where k is a constant, in this case 1.25, ε_y is the yield strain taken as 0.2% or 0.002.

Summation by quadrature was used to consolidate the various dislocation mechanisms, as they act unevenly throughout the matrix [101, 163]:

$$\Delta\sigma_{dis} = \sqrt{(\Delta\sigma_{Or}^I)^2 + (\Delta\sigma_{Or}^{II})^2 + (\Delta\sigma_{GND})^2} \quad 3.5$$

where $\Delta\sigma_{Or}^I$ is the Orowan strengthening due to nitride particulates and $\Delta\sigma_{Or}^{II}$ is the Orowan strengthening due to the nanoscale reinforcement in Al-B₄C-1. The strengthening in Al-B₄C-1 can then be summed as:

$$\sigma_y = \Delta\sigma_{dis} + \Delta\sigma_{HP} + \Delta\sigma_l \quad 3.6$$

The individual contributions come out as $\sigma_y = 241MPa + 684MPa + 17MPa = 942MPa$ for Al-B₄C-1. In Al-B₄C-2 there is no Orowan contribution from the boron carbide, and so it is somewhat lower as $\sigma_y = 135MPa + 710MPa + 17MPa = 862MPa$. Finally, for the unreinforced alloy, the only dislocation mechanism is due to secondary nitrides and the estimated yield strength is $\sigma_y = 133MPa + 595MPa = 728MPa$. However, a root sum square overestimates this strengthening, and a better estimate would be ~40 MPa, leading a final alloy strength of 635MPa. The estimate of 40 MPa also aligns well with that found by Cao and Ramesh [105], for nanoparticles in aluminum.

The results of the above calculations and the contributing mechanisms are summarized in Table 3.3. The estimates resulting from the treatment provided here closely match the experimentally obtained values, though the unreinforced alloy strength is considerably overestimated with this method. The experimental and calculated values of the yield strength also indicate an increased yield strength for Al-B₄C-1 reinforced with the smaller 40 nm boron carbide as compared to Al-B₄C-2. The reduction of particulate reinforcement size has been found to improve yield strength in other aluminum matrix composites [168], which supports the results found here.

Table 3.2 presents some examples of MMC yield strengths from the literature along with details regarding the reinforcement used and its approximate size. Due to limited space, the specific heat treatments and processing conditions could not be included. However, the yield strengths exhibited by the composites under investigation in this dissertation hold up well against a variety of reinforcement types and loading volume fractions.

Table 3.2: A selection of yield strength data from the literature is presented for lightweight MMCs, along with information regarding the reinforcement material, type and size. The yield strengths vary significantly based upon reinforcement parameters, but also the processing technique used and the addition of heat treatments or plastic work such as extrusion.

Material	Estimated YS (MPa)	Reinforcement Material	Reinforcement Type	Reinforcement Size	Ref
Al-5 wt. %	900	B ₄ C	Particle	~50 nm	This work
Al-5 wt. %	850	B ₄ C	Particle	~ 500 nm	This work
Al-7 wt. %	579	SiC	Whisker	~750 nm diameter	[169]
Mg-3 wt. %	275	SiC	Particle	~30 nm	[170]
Al-10 vol %	210	SiC	Particle	~10 μm	[35]
Al-25 vol. %	371	SiC	Particle	~11.5 μm	[93]
Al-5 wt. %	950	B ₄ C	Particle	~1-7 μm	[157]

Table 3.3: The estimated yield strengths of the unreinforced aluminum alloy and reinforced composites and the contributions from the various strengthening mechanisms.

Material	Estimated Yield Strength (MPa)	Contribution $\Delta\sigma_{dis}$ (MPa)	Contribution $\Delta\sigma_{HP}$ (MPa)	Contribution $\Delta\sigma_l$ (MPa)
Al-B ₄ C-1	942	241	684	17
Al-B ₄ C-2	862	135	710	17
NR-Al	728	133	595	-

Notes:

$\Delta\sigma_{dis}$: Dislocation strengthening resulting from Orowan mechanisms and GND dislocations due to modulus mismatch

$\Delta\sigma_{HP}$: Hall-Petch strengthening due to grain refinement

$\Delta\sigma_l$: Load transfer to reinforcement particles in the composites

3.3.3 Rate Dependence and Its Significance

The influence of strain rate on the three materials was investigated using a series of strain rate jump tests performed on a nanoindenter. Strain rate sensitivity (m) is an indicator of a material's yield or flow strength as a factor of strain rate. The strain rate sensitivity was calculated as [171]:

$$m = \frac{d \ln H}{d \ln \dot{\epsilon}} \quad 3.7$$

where H is the hardness and $\dot{\epsilon}$ is the indentation strain rate defined by $\dot{\epsilon} = \dot{P}/P$, with \dot{P} being the loading rate during indentation and P being the load. The results are shown in Fig. 3.8 and include a high strain rate data point from the dynamic compression tests. It should be noted that unlike conventional coarse grain metals where including high strain rate data usually brings up the SRS value, in the case of Al-5083 and the two Al-MMCs in this work, including the high strain rate data points brings down the SRS values for all the materials. As a matter of fact, the nanoindentation-based SRS values for the three materials are 0.053, 0.047 and 0.034 for Al-5083, Al-B₄C-1 and Al-B₄C-2, respectively. The SRS of coarse grain Al is typical of metals with face-centered cubic (FCC) structure such as Cu and Ni, on the order of 0.004. Refining the grain size of FCC metals into ultrafine grain and nanocrystalline (NC) regimes has been shown to increase the SRS [171]. It is observed from the indentation rate jump experiments that the three Al-based materials of this work follow the same trend. In other words, the SRS at quasi-static rate, particularly probed by nanoindentation, is controlled by the Al-matrix phase. However,

bulk testing such as uniaxial compression at different strain rates shows a different trend in terms of rate dependence. This observation is similar to those of bulk metallic glasses (BMGs) and other brittle materials where dynamic loading leads to reduced strength, primarily because of sensitivity to stress concentration. That being said, it is believed the bulk SRS indicates under high strain rate loading, the plastic deformation of the materials are controlled by different factors, such as the presence of reinforcement and initiation of failure.

From the Hart criterion [172] for a strain rate sensitive material:

$$\frac{1}{\sigma} \left(\frac{\partial \sigma}{\partial \dot{\varepsilon}} \right)_{\dot{\varepsilon}} - 1 + m \leq 0 \quad 3.8$$

In Eq. 3.8 a greater m value makes the material less susceptible to inhomogeneous deformation even in the absence of strain hardening. While Hart and others [173, 174] were interested in the stability during tensile deformation, this stabilizing factor also plays a role in the likelihood of adiabatic shear band formation during compression [175]. Looking at the m values in Table 3.1 and Fig. 3.8 it can be seen that bulk strain rate sensitivity of the materials is quite low, similar to that of coarse grain FCC metals such as copper [176, 177].

The m value for these UFG aluminum materials is unusually small if the high rate data point is included, as m tends to increase with grain refinement for FCC metals. Carreker and Hibbard [177] were one of the first to discover the grain size dependence of the strain rate sensitivity, with values ranging from ~ 0.004 for coarse grain copper to ~ 0.0072 for slightly more refined grains. Further investigations such as those by E. Ma

[178] on UFG copper, and J. May [179] on UFG aluminum found that relatively large m values of 0.03 and 0.014 respectively, could be obtained. As such, the low strain rate sensitivity of the three UFG materials in this investigation is uncommon, though similar values have been reported previously [180]. The low m values found here contribute to the deformation behavior that will be discussed in the following section.

3.3.4 Plastic Deformation and Shear Band Formation

Looking at the behavior of the three materials after yielding, there is a clear difference between the composite and alloy behavior, as well as the quasi-static and dynamic behavior. The unreinforced alloy strain hardens under both quasi-static and dynamic strain rates, while Al-B₄C-1 is elastic-nearly perfectly plastic in the quasi-static regime both Al-B₄C-1 and Al-B₄C-2 strain soften during dynamic loading. In regards to the microstructure, the composites and alloy are very similar, as both are stabilized by Zener pinning that results from by-products formed during cryomilling [94, 142, 151]. The difference between the composite and alloy behavior is therefore due to the addition of boron carbide.

As strain softening is often a result of microstructural damage, the difference in the plastic response of Al-B₄C-1 between quasi-static and dynamic loading is microcracking that occurs at the reinforcement-matrix interface. While this process would occur at both quasi-static and dynamic strain rates in the composites, at dynamic rates the addition of thermal effects results in overall strain softening. As seen in Fig. 3.5 (a), when thermal softening is not a factor due to low strain rates, any microstructural damage leads to an almost steady state, perfectly plastic deformation.

When considering ASB formation, low strain rate sensitivity, low strain hardening and high thermal softening are all known to make materials more susceptible to the development of ASBs [175]. Due to the strain hardening that occurs in the unreinforced alloy as well as the lack of microstructural damage, no ASBs are seen at either quasi-static or dynamic strain rates. Conversely, the composite samples exhibited ASB formation during dynamic loading due to the transient strain hardening and significant strain softening that occurs. However, the strain hardening, though limited, that occurs in the composites at quasi-static strain rates along with the additional time for thermal diffusion are sufficient to prevent the formation of ASBs. The formation of two conjugate ASBs exhibited by Al-B₄C -1 and -2 is in contrast to aluminum MMCs that consist of larger, micron-sized reinforcements [157] where shear banding occurs, but is distributed throughout the specimen. It has been shown previously that the introduction of reinforcing particles can inhibit ASB development [169], though based on the observation of these nanometric reinforced MMCs, it appears that by reducing the particle size to the nanoscale, ASB formation is no longer repressed.

The mechanical behavior of Al-B₄C-1 under quasi-static loading is quite interesting as it exhibited a strain to failure of over 15%, only slightly less than that exhibited during dynamic loading. In comparison, a similar aluminum alloy reinforced with micron-sized boron carbide and coarse-grained matrix material to aid in deformation, was tested at the same quasi-static strain rate and sustained less than 5% strain [157] before failure. Previous investigations have found impressive strain to failure of up to ~25% in other aluminum based nanocomposites [86], however the composites Al-B₄C -1 and -2 do not contain any coarse-grained matrix material and did not require

the further step of undergoing extrusion. The significant variation in strain-to-failure at quasi-static strain rates indicates the importance of reinforcement size on the deformation of these types of composite material.

A common phenomenon in ceramic reinforced composites is microcracking, where small cracks form at the interface of the metal matrix and reinforcing material, and it has previously been suggested [157] that this process is the source of the improved strain-to-failure at dynamic strain rates. While no microcracks at the interface between the matrix and B_4C were observed in this investigation, enhanced plasticity at dynamic strain rates was observed and it is an area that will receive further analysis.

In the interest of predicting the likelihood of adiabatic shear band formation, an analysis in the form of that taken by Grady [129] was performed. In this treatment the shear band is considered as a two-material system; the shear-band process zone which exists at the front of the shear band and propagates along the shear plane, and the thermally-softened material behind the process zone where the flow stress relaxes to zero and well-lubricated shear slip occurs. This analysis is actually an analogy to mode II fracture, in which the shear band nucleates and progresses with a finite growth rate and does not form along the full shear plane simultaneously [132]. Such behavior is supported by post-loading surface analysis of the composite samples as shown in Fig. 3.6 (b) and 3.6 (c). Shear localization is more concentrated at one end of the shear band, and the amount of deformation decreases progressing along the band.

In order to make the model more accessible and quickly applied, a two-dimensional approach is simplified to a one-dimensional analysis, but the time variation of temperature and stress is retained. A specific model of thermoplastic shear

deformation is used to calculate the dissipation within the shear-band process zone, and while the key equations will be presented, a thorough analysis can be found in the literature [128, 129]. In this model, it is assumed that the stress and dissipation rate only differ from zero in the process zone, and that the shear band has a defined thickness within which temperature and shear strain are constant. Linear thermal softening is assumed, and takes the form:

$$\tau = \tau_y (1 - \alpha\theta) \quad 3.9$$

where α is a softening coefficient, τ_y is the shear flow stress, taken as 57% of the compressive yield stress following a von Mises yield criterion, and θ is the temperature excursion above ambient temperature. Solutions where the flow stress relaxes to zero due to thermal softening are sought, when the material has surpassed a critical shear displacement, ψ_c . An implicit expression for the critical shear displacement can be formed:

$$\psi_c = \sqrt{\frac{32\tau_y\dot{\gamma}}{9\rho\chi_a^3} \left(\frac{\alpha\tau_y}{2c_a} \Psi_c - 1 \right)^3} \quad 3.10$$

The global shear strain rate is represented by $\dot{\gamma}$ and the properties $\chi_a = 2\chi/a^2$ and $c_a = \rho c a/2$ are the areal heat transfer and areal heat capacity, where c and χ are the bulk specific heat and thermal diffusivity coefficients. The critical displacement can be

related to the plastic dissipation within the shear band through the relation $\Gamma_c = \tau_y \psi_c / 2$, and for an optimum shear band thickness a_0 , the shear band dissipation energy is:

$$\Gamma_{c0} = \frac{\rho c}{\alpha} \left(\frac{9\rho^3 c^2 \chi^3}{\tau_y^3 \alpha^2 \dot{\gamma}} \right)^{1/4} \quad 3.11$$

The shear band dissipation energy calculated in Eq. (3.11) based on one-dimensional analysis, provides the shear band dissipation energy expended within the process zone $\Gamma_{c0} = \Gamma_s$. A shear band toughness, approximating the susceptibility of a material to ASB formation, can then be introduced with the relation $K_s = \sqrt{2G_m \Gamma_s}$. The material parameters and the resultant toughness values obtained are provided in Table 4. Based on Eq. 3.11, it can be seen that increases in density, specific heat capacity, and thermal diffusivity are stabilizing factors, while increases in flow stress result in a greater susceptibility to ASB formation.

In order to determine the influence the B₄C reinforcement had on the material parameters of the composites, the rule of mixtures was used. Boron carbide has a slightly higher specific heat capacity than Al 5083 at room temperature, and a somewhat lower density, yielding little change to the calculated toughness. Even the low thermal conductivity of 17 (W / K · m) compared to Al 5083's 117 (W / K · m) has a small effect once the volume fraction of boron carbide is taken into account. A thermal softening factor of $\alpha = 8 \times 10^{-4}$ was chosen for the three materials based on those used by Grady [129] and the increased microstructural stability imparted by secondary nanoscale particles. As a

result, the largest factor contributing to the shear band toughness is the yield stress of the material, which was highest in the composite materials. While the resultant shear band toughness values are not significantly different, they do match the trend observed during dynamic loading.

3.4 Summary and Concluding Remarks

The effects of boron carbide reinforcement on the microstructure, plastic deformation and mechanical properties of a high strength aluminum alloy have been investigated. The addition of B₄C regardless of size (40 nm or 500 nm), has been found to improve the yield strength of the metal matrix composites by 30% while also providing stiffness improvement as compared to the unreinforced alloy. Results also suggest that the further reduction of the reinforcement dimension from 500 nm to 40 nm produces a composite with a higher yield strength. Models have been proposed to estimate the yield strength based on material microstructural features and have been found to approximately agree with the experimental results. Additionally, the improved strength and moderate plasticity of the Al composites are exhibited at both quasi-static ($1 \times 10^{-3} \text{ s}^{-1}$) and dynamic ($4 \times 10^3 \text{ s}^{-1}$) strain rates. This improved strain to failure at quasi-static strain rates is a considerable improvement over aluminum alloys reinforced with micron-sized B₄C, though it does come at the cost of reduced yield strength.

In addition, the introduction of nanoscale boron carbide results in the development of adiabatic shear banding under uniaxial high strain rate compression. This behavior is not observed in the unreinforced alloy as its greater ability to strain harden, and the increased time for thermal diffusion removes this deformation pathway. The occurrence of adiabatic shear banding under dynamic loading can be rationalized from a

mechanistic model that analogized the initiation and propagation of ASB to those of a model II crack. A simple estimation indicates that the un-reinforced aluminum alloy exhibits the highest ASB toughness. The ASB toughness of the reinforced materials is reduced, making these materials more prone to ASB. Exhibiting excellent plasticity at dynamic and quasi-static strain rates considering the UFG nature of the composites, and demonstrating increased strength, these nano-reinforced MMCs are of great interest for continued study.

CHAPTER 4: COMPRESSIVE BEHAVIOR OF AL 5083 COMPOSITES AT ELEVATED TEMPERATURES

4.1 Introduction

Microstructural stability is an important parameter for any material being considered for structural applications. It is of even greater importance if the part spends part of its lifecycle at elevated temperatures. As mentioned in the Introduction, high strength aluminum alloys and composites have found uses in both the aerospace and automotive industries. In both cases elevated temperatures are frequently experienced through frictional heating resulting from tooling contact or air friction. A particularly important example of the later can be found in the development of the SR-71 Blackbird [181]. Initial tests using aluminum alloys found that the frictional heating that occurred above Mach 2 made the aluminum unstable, and Ti alloys were eventually used instead. While I am not proposing the materials at the focus of my dissertation work for use in supersonic aircraft, the anecdote does stress the importance of characterizing the performance of new materials over a wide range of temperatures.

Based on the work by Lloyd et al. [75] and others [182-184], the greatest influence on the fracture mechanics of the Al MMCs is due to the matrix. As the aluminum matrix has a much lower melting temperature than the boron carbide reinforcement, 660 °C compared to 2445 °C, and makes up 95% of the composite, this is reasonable. However, the reinforcement can still affect the deformation of MMCs at elevated temperatures even when the volume fraction of the reinforcement is quite low.

Lloyd et al. looked at the influence of the volume fraction of Al_2O_3 at temperatures between 100 °C and 300 °C for an Al 2014 alloy [75]. In their investigation, he found that particle volume fraction played an important role in the fracture mechanics at elevated temperature, and the existence of a transition temperature where the primary damage mechanism changes from particle cracking to interparticle voiding, which is shown in Fig. 4.1. In my study, dynamic compression tests were performed at elevated temperatures of 100, 200, 300, and 400 °C on Al- B_4C -1 and Al- B_4C -2. The results of those tests and an analysis of the role of the boron carbide reinforcement in the fracture mechanics will be presented in this chapter.

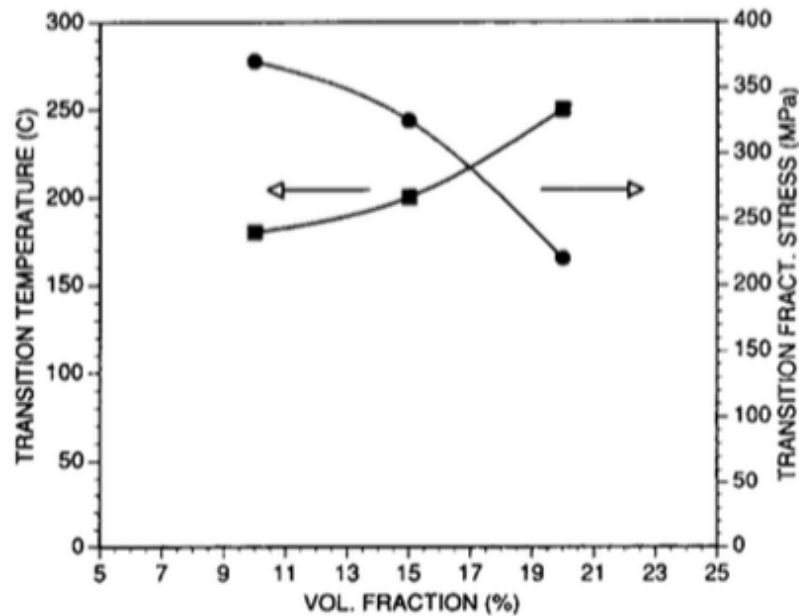


Figure 4.1: The transition of the primary damage mechanism from particle cracking to interparticle voiding due to the reinforcement volume fraction %. As the volume fraction increases, interparticle void formation becomes more likely [75].

4.2 Experimental Results

4.2.1 Elevated Temperature Compression Tests

The results from the dynamic compression tests performed at 100, 200, 300, and 400 °C on Al-B₄C-1 and -2 are presented in the following section. The strain rates imposed on the samples are similar to those used in the room temperature dynamic tests that were previously covered. While the exact strain rate experienced by the specimen differed somewhat from test to test, they were all on the order of 10^3 s^{-1} with an average strain rate around $5.0 \times 10^3 \text{ s}^{-1}$. At least three tests were conducted at each temperature and representative results for the two composites along with the room temperature (RT) behavior are shown in Fig. 4.2. As before, the point at which the true stress-true strain curve ends is not indicative of sample failure but sample unloading.

First of all, it is readily apparent that a decrease in the yield strength occurs at each progressively higher temperature. The exact amount of the decrease varies from sample to sample, but overall both composites undergo a softening of about 200 MPa from RT to 400 °C, with Al-B₄C-1 dropping from a yield stress of ~900 MPa to ~700 MPa and Al-B₄C-2 dropping from ~850 to 650 MPa using a 4% offset to allow for stress equalization. Additionally, the softened microstructure allows for greater deformation as the temperature increases, and while not true for every trial, a trend is established where the amount of strain the specimen undergoes increases with increasing temperature.

The behavior of the composites after yielding produced some interesting results. In the case of Al-B₄C-1, with some exceptions, the strain softening that occurred after yielding is consistent. Qualitatively this can be seen in Fig. 4.2a as each flow curve is approximately equidistant from those above and below it. Comparing this to the behavior

exhibited by Al-B₄C-2 in Fig. 4.2b, it can be seen that the RT, 100 and 200 °C curves are all very similar after yielding and almost overlap, and it is not until the tests at and above 300 °C that significant flow softening develops. In order to quantify the flow softening, points along the curves were taken and a rough linear value was obtained for the flow softening occurring in each composite at the various testing temperatures, the results are provided in Table 4.1, and were plotted in Fig. 4.3 to aid in visualization.

Table 4.1: The approximate strain softening that occurs in the composite samples at temperatures ranging from RT to 400 °C during dynamic loading. Al-B₄C-1 exhibits greater strain softening at all temperatures, with nearly equivalent strain softening after the temperature is increased. Al-B₄C-2 shows less strain softening until 300 °C at which point it is approximately equivalent to Al-B₄C-1.

Testing Temperature	RT	100 °C	200 °C	300 °C	400 °C
dσ/dε of Al-B ₄ C-1 (MPa)	-675	-841	-702	-932	-888
dσ/dε of Al-B ₄ C-2 (MPa)	-437	-370	-382	-841	-677

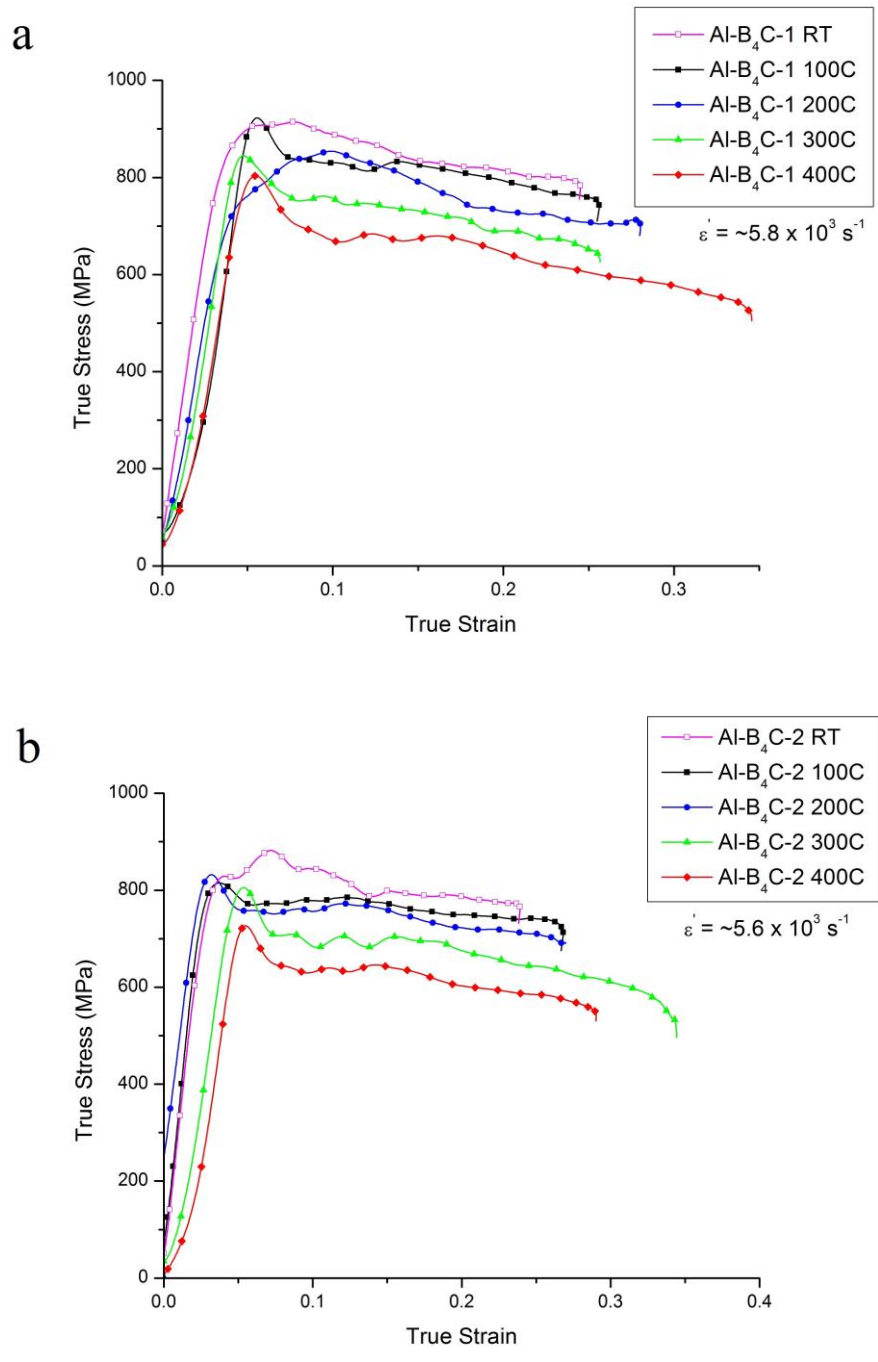


Figure 4.2: The elevated temperature dynamic response of Al-B₄C-1 (a) and Al-B₄C-2 (b) from RT to 400 °C. Significant strain softening is exhibited by both composites, though Al-B₄C-2 underwent less strain softening at temperatures below 300 °C.

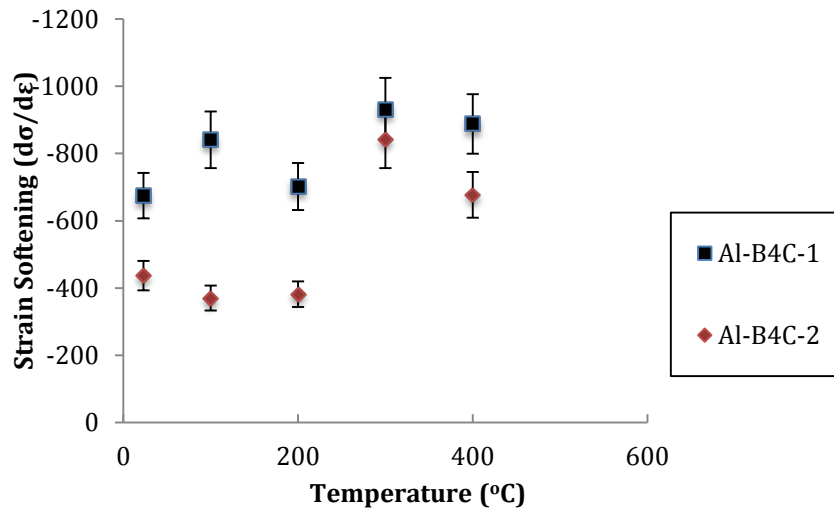


Figure 4.3: Strain softening exhibited by Al-B₄C-1 and Al-B₄C-2 under dynamic loading at room, and elevated temperatures. Al-B₄C-1 undergoes significant strain softening at all temperatures with a small increase in average softening at 300 °C. Al-B₄C-2 undergoes consistently lower strain softening until 300 °C when softening increases dramatically, possibly indicating a critical softening temperature.

It is now easy to see that the strain softening that occurs in Al-B₄C-1 is more consistent over the range of temperatures that tests were performed. Al-B₄C-2 on the other hand undergoes less flow softening until temperatures rise above 200 °C, or about 50% of aluminum's homologous melting temperature. Eventually Al-B₄C-2 begins to undergo softening comparable to that exhibited by Al-B₄C-1 though still slightly less severe. A visual representation of this can be seen in Fig. 4.4 that presents flow curves from both composites. In Fig. 4.4 the effect of the differences in flow softening can be seen, as Al-B₄C-1 yields at a higher stress than Al-B₄C-2 and so a gap between the curves exists at low strains, but by the time unloading occurs, the two composites have either reached an equivalent stress or Al-B₄C-1 has softened below that of its contemporary.

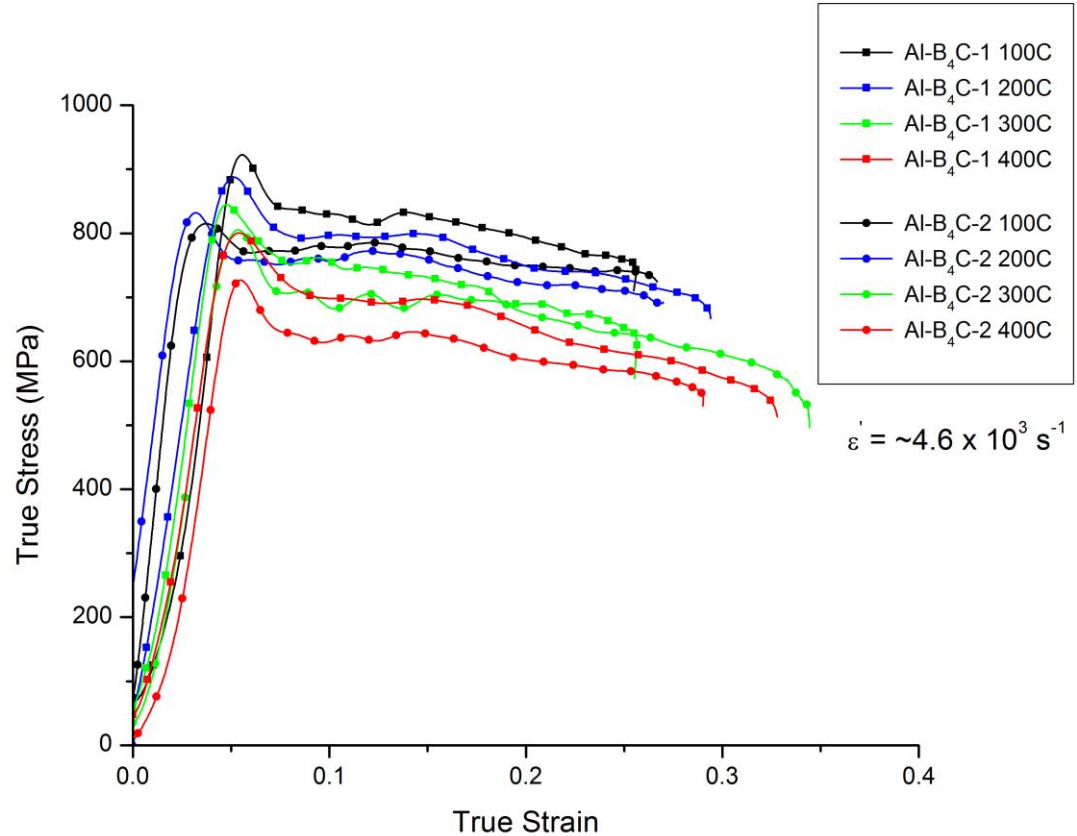


Figure 4.4: Representative flow curves for both composites comparing their response to dynamic loads. The differences in flow softening identified earlier are more pronounced here. In addition to strain softening, progressive flow softening as a result of increased temperature is readily apparent.

4.2.2 Post-loading Surface Examination

Surface examinations were performed using an SEM to help characterize the deformation that takes place during loading. As shown in Fig. 4.5 and 4.6, every Al-B₄C-1 specimen formed cracks during loading and as evidenced by many of the magnified images, in the areas of highly localized shear along the ASB the sample experienced temperatures great enough to cause the sample to melt (4.5b, 4.6b). Evidence of large

shear localization is apparent in the magnified images in 4.5d, and 4.6d. In addition to the primary shear bands that form, additional secondary cracks tend to form along the sides of the bands, with their size dependent upon the number of microcracks that coalesced.

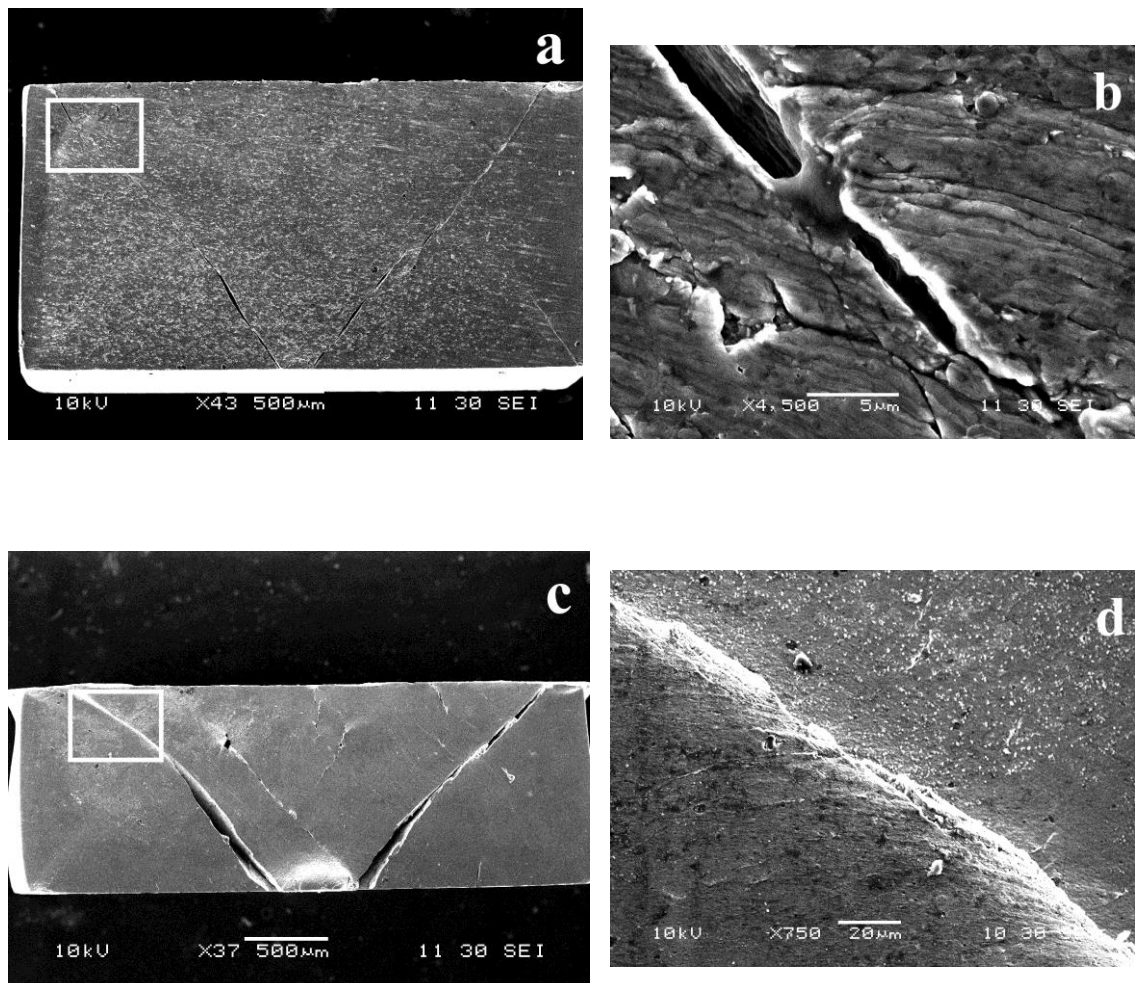


Figure 4.5: SEM surface evaluations of Al-B₄C-1 at 100 (a-b) and 200 °C (c-d) after dynamic loading. Enlarged images of the highlighted areas in (a) and (b) are shown in (b) and (d) respectively. The high temperatures that develop along the ASBs are severe enough to cause melting as evidenced in (b), and the large strain localization and flow lines are easily seen in (d).

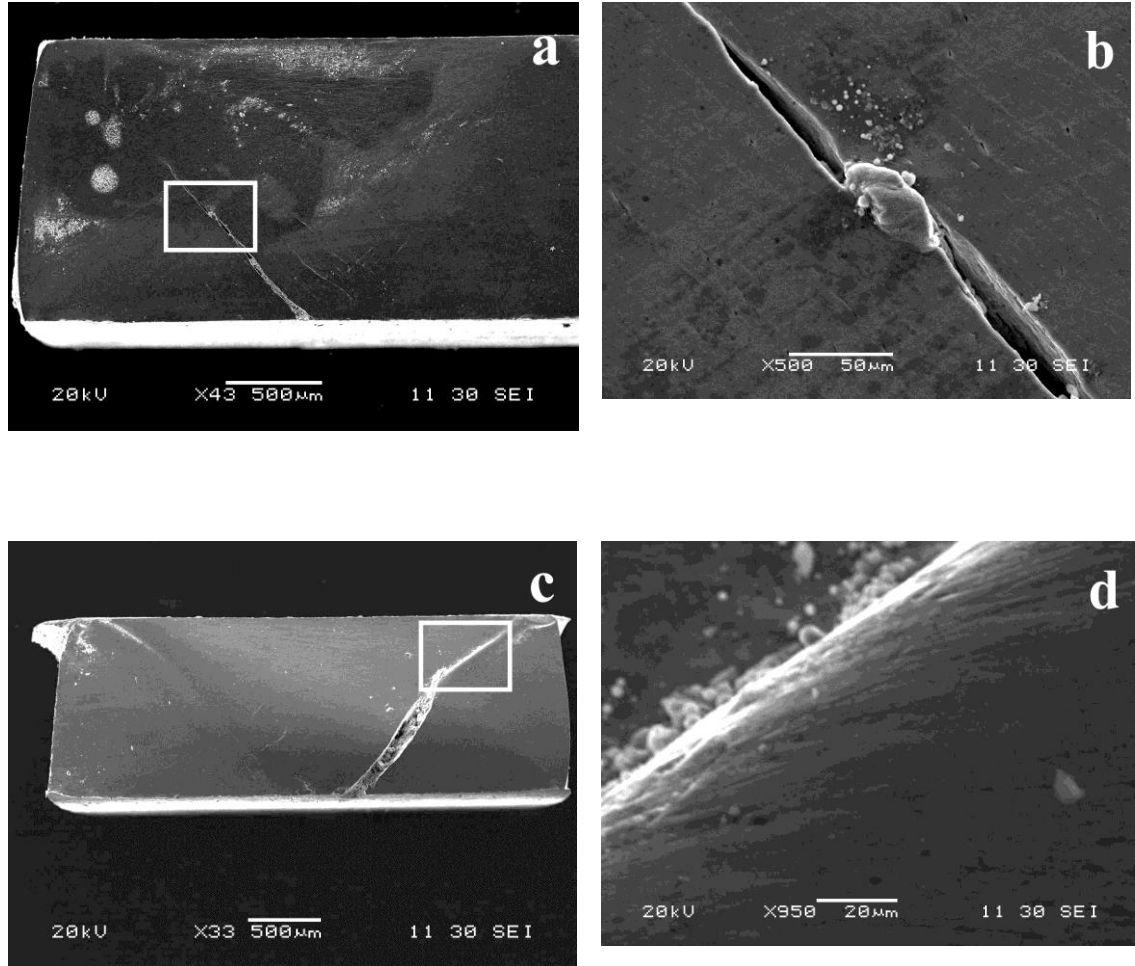


Figure. 4.6: Similar to the observations at lower temperatures, the SEM surface analysis at 300 (a-b) and 400 °C (c-d) reveals that significant strain localization and heating continues to occur.

The deformation exhibited by Al-B₄C-2 was similar (Fig. 4.7 and 4.8), however there were some marked differences. The cracks that formed were not as extensive or numerous, and the specimen deformation was not as affected by the elevated temperatures. Looking at the deformation of Al-B₄C-2 at 300 °C shown in Fig. 4.8a-b, very few cracks formed and no major shear bands developed.

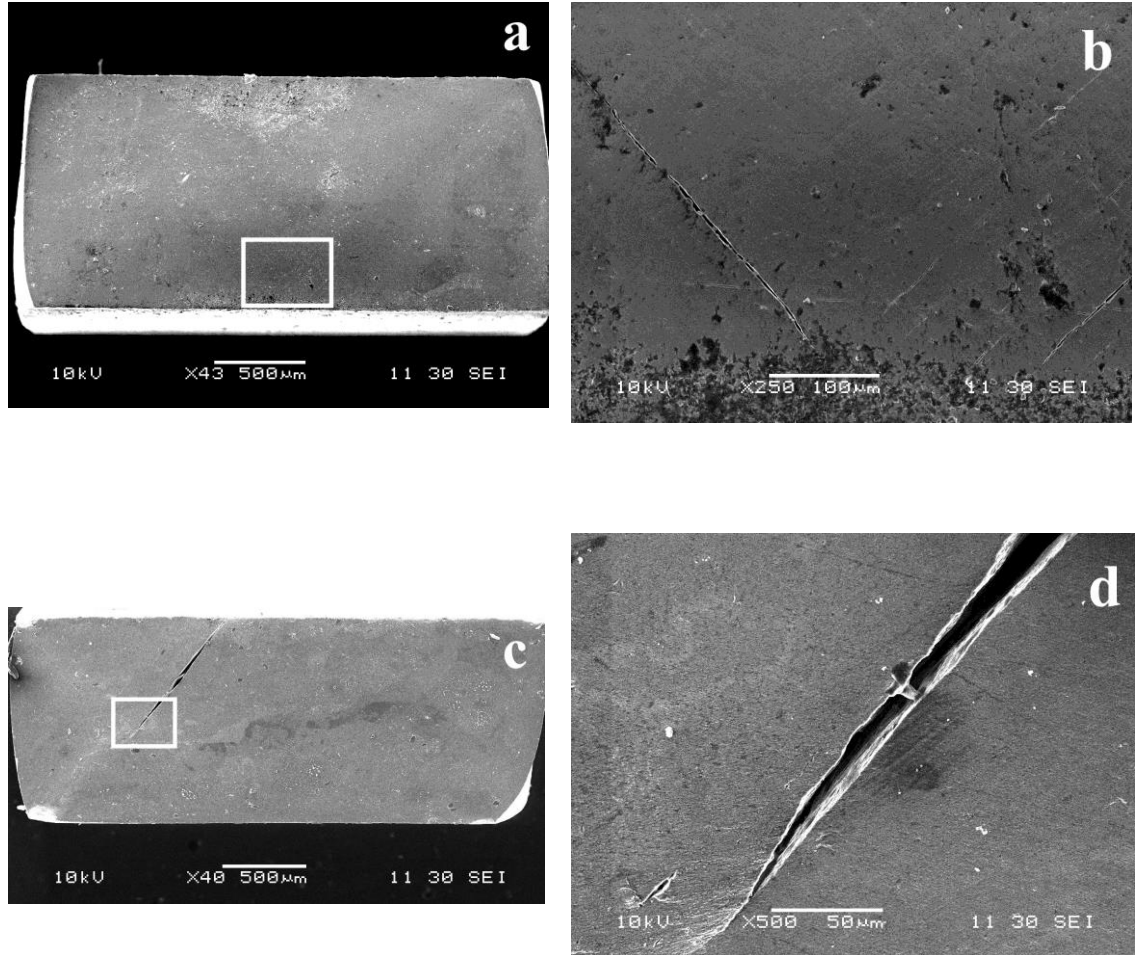


Figure 4.7: The post-loading SEM images of Al-B₄C-2 at 100 (a-b) and 200 °C (c-d) show that ASBs still form, though they are less pronounced than those in Al-B₄C-1. Additionally, the strain localization resulting in the formation of the ASBs is not apparent on the specimen surface. The significant heating is still visible in the melted matrix along the shear band as seen in (d).

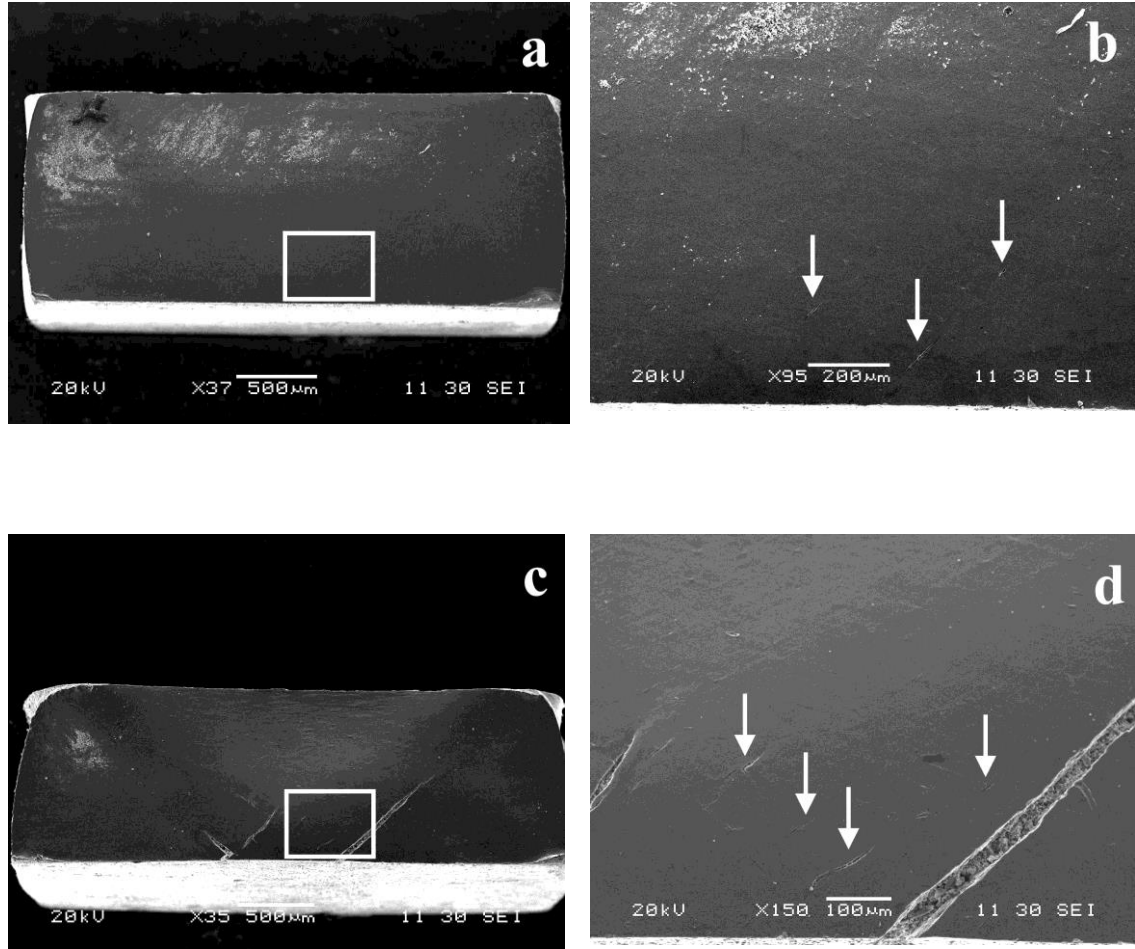


Figure. 4.8: The elevated temperature SEM analysis of Al-B₄C-2 at 300 (a-b) and 400 °C (c-d) is shown here. While the 400 °C sample displays the greater softening and cracking expected at higher temperatures, the 300 °C sample shown in (a-b) exhibits very little cracking.

4.3 Discussion

In this section I will evaluate the compressive behavior of the aluminum composites at elevated temperatures. Properties such as material strength and deformation mechanism have been discussed in Chapter 3, and will not be repeated here. Specifically the effect, if any, which the size of the reinforcement has on the dynamic response of the MMCs will be discussed. The behavior observed during experimentation

consisted of a decrease in material yield strength, increased strain softening, and generally greater crack formation and plastic deformation. The evolution of microstructural damage is intimately related to each of these behaviors, and as will be shown, the size of the reinforcement likewise influences the development of microstructural damage.

Damage in metal matrix composites is regarded as taking two main forms, either particle cracking or void formation at the particle-matrix interface [182, 184-188]. The influence of particle size on particle fracture, fracture toughness and void growth has been studied [183, 189, 190], and it was found that particle size does not significantly influence the onset of crack formation [188], while larger particles are at greater risk of particle fracture and provide additional routes for material softening. Arsenault and Flom were examining fracture toughness, and as such crack formation refers to a propagating failure and not microcracks at the reinforcement interfaces. As particle cracking primarily occurs under tensile loading, no particle cracking was observed in the post-loading samples in this study. The findings of Arsenault and Flom [188] regarding the lack of particle size effects on the onset of crack formation may seem to indicate a particle size insensitivity, however the results of this investigation show that is not the case. The experimental results show that Al-B₄C-1 exhibited greater flow softening than Al-B₄C-2, and the flow softening reached a maximum value at 100 °C that then persisted. As the only difference between the two composites from a material standpoint is the size of the reinforcement, it must be playing a role in the different deformation behavior.

Before continuing the discussion of the observed behavior, it is important to discuss certain fundamental concepts that will aid in the description of the composite

behavior. The first concept to address is the condition for void nucleation, which has been treated in two primary ways, with an energy-based criterion [191, 192] and with a critical stress criterion [182, 189, 193] which will be the basis used in this investigation. The critical stress which governs unstable cavitation growth is defined by Wu and Ramesh [182, 189, 193] as:

$$\rho_c = \frac{2}{3} \sigma_Y + \int_{\varepsilon_Y}^{\infty} \frac{\sigma_e}{e^{(3\varepsilon/2)} - 1} d\varepsilon \quad 4.1$$

where σ_Y is the yield stress, σ_e is the effective stress, and ε_Y is the yield strain defined as $\varepsilon_Y = \sigma_Y / E$. It is important to note the absence of particle size in this treatment, primarily because they were interested in modeling the growth of a void regardless of origin. However, when considering the dynamic compression of these aluminum MMCs, a supercritical loading condition where the applied stress exceeds the critical stress can be assumed. In that case, it is accepted that voids will form and what is of interest is the rate of void growth, and hence the rate of damage that occurs. Under supercritical conditions, an equilibrium void growth rate is obtained [186]:

$$\dot{a}_c = \sqrt{2(p^{app} - p_c) / 3\rho} \quad 4.2$$

where p^{app} is the applied stress and p_c is the critical stress as defined in Eq. 4.1. What can be seen from Eq. 4.2 is that under supercritical conditions, the initial void size does not influence the rate of void growth. This is also represented in Fig. 4.9 [182] that shows how the void growth rate quickly equalizes regardless of initial void size, with the

exception of the 10 nm void which stops growing due to heat conduction. In my case, the smallest void formed would result from 40 nm particles and therefore behave similar to the 30 nm voids provided in Fig. 4.9.

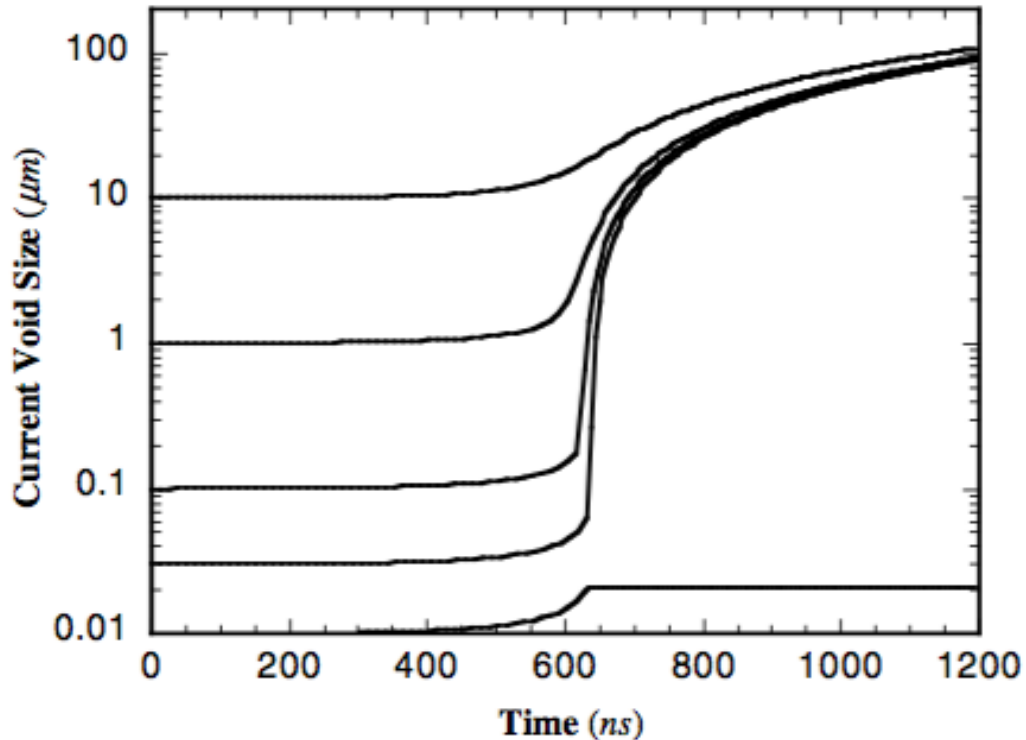


Figure 4.9: After a void is nucleated in a matrix material, the results from Wu and Ramesh indicate that as long as the void is above a minimum size of 10 nm, it will quickly grow to an equivalent void size with void growth equalizing [182].

So if the initial void size does not greatly influence void growth under dynamic loading, what explains the difference in the flow softening between the two MMCs? The answer lies in the loading volume fraction and the size of the reinforcements used. While crack formation is not influenced by particle size, the number of voids formed at the particle / matrix interface depends on the volume fraction of reinforcement particles and

consequently the particle size. For a given volume fraction of reinforcement, each particle will occupy a volume that scales with r^3 , so even though the radii of the two reinforcements in this investigation only differ by an order of magnitude, the resultant number of particles differs by three orders of magnitude. Correspondingly, there are a much greater number of void nucleation sites in Al-B₄C-1 compared to Al-B₄C-2, and so a greater rate of microstructural damage. What is intriguing is the saturation in the number of voids formed that occurs in Al-B₄C-1, as indicated by the nearly constant strain softening exhibited from 100 °C to 400 °C (Table 4.1, Fig. 4.3). In contrast, Al-B₄C-2 follows a trend more consistent with other studies where the damage increases with increasing temperature as shown in Fig. 4.10a and 4.10b [189]. When Al-B₄C-2 is tested above 200 °C, it exhibits a strain softening value similar to that of Al-B₄C-1, and there seems to be a maximum void formation/damage rate in these composites where strain softening does not continue to increase with increasing temperature. The difference in initial strain softening rates is likely due to the larger number of nucleation sites available when the reinforcement size is reduced, and consequently Al-B₄C-1 reaches saturation much more rapidly. This is not a concept I have seen addressed directly in the literature, and may be a topic for future study.

Additionally, while metals are known to lose significant strength above $0.4 T_{MP}$, the significant increase in softening observed in Al-B₄C-2 from 200 to 300 °C, and shown in Fig. 4.3, indicates the existence of a critical temperature. Upon exceeding $0.5 T_{MP}$ the aluminum matrix has softened sufficiently such that void formation requires less energy and the rate of void formation in Al-B₄C-2 increases, quickly reaching “saturation.”

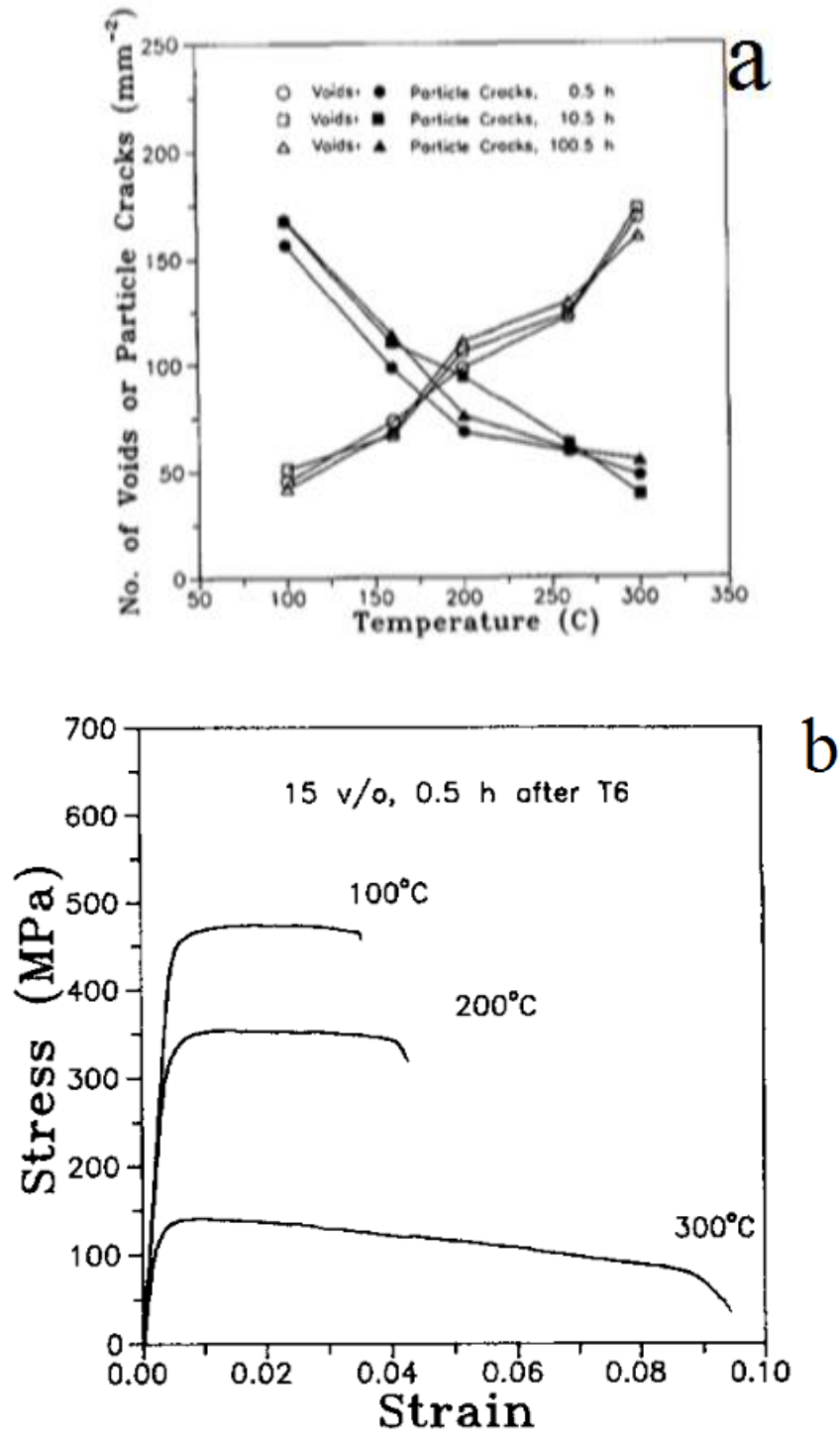


Figure 4.10: The transition temperature where the primary fracture mechanism switches from particle cracking to void nucleation (a). While (b) demonstrates the flow softening and increased strain softening that occurs at elevated temperatures of an aluminum MMC [189].

In terms of the plastic deformation demonstrated by the SEM surface analysis, the plastic response of the composites was very similar to the RT behavior. Cracks formed along the planes of maximum shear and shear localization was evident. However, the width of the localization was greatly decreased, with shear strain apparent in only a very limited area around the ASB. In some cases, the strain localization was barely evident at all as shear instability promptly led to extensive crack formation. This behavior was expected, as the softening of the matrix at elevated temperatures reduces the interface strength and makes strain localization more likely.

4.4 Conclusion

Aluminum MMCs reinforced with nanometric and half-micron boron carbide underwent dynamic compression at temperatures ranging from 373 K to 673 K. The composites exhibited a decrease in flow strength with increasing temperature consistent with matrix-controlled softening. Commiserate with the decrease in flow strength, Al-B₄C-2 reinforced with half-micron boron carbide, underwent progressively larger strain softening at higher temperatures, with maximum flow softening occurring at temperatures above 473 K. In contrast, Al-B₄C-1 reinforced with 50 nm boron carbide, exhibited maximum strain softening at the first elevated temperature of 373 K, at which point the rate of softening did not increase at higher temperatures. The softening of each MMC seems to saturate to approximately the same rate and then plateau, and the cause for this plateau may be an interesting area for future study.

The MMCs performed as expected of metals that are susceptible to thermal softening, and pronounced cracks developed during loading at elevated temperature. The number and severity of the cracks increased with increasing temperature, as the energy

required for void formation at the particle-matrix interface was lowered. While these MMCs have significant microstructural stability as a result of nitrides produced during processing, and in the case of Al-B₄C-1 additional nanometric reinforcement. The pinned grain boundaries do not significantly affect the mechanical behavior at elevated temperatures with a marked degradation in material performance evident with increasing temperature.

CHAPTER 5: INFLUENCE OF REINFORCEMENT SIZE ON COMPOSITE PERFORMANCE

5.1 Introduction

There are two main methods of improving composite performance, with changes due to the material properties of the reinforcement. Or due to the effect the reinforcement has on the matrix microstructure. An example of the former can be seen when considering thermal conductivity improvements that result when carbon nanotubes (CNT) are added to a metal matrix, and their unique properties assist in thermal transport [20]. The latter mechanism can be observed in the development of dislocations that result from CTE mismatches [33] between the matrix and reinforcement. In addition, parameters such as reinforcement size and aspect ratio affect mechanical performance [83, 168, 194].

In the previous chapters, the mechanical properties and plastic response of boron carbide reinforced Al MMCs have been presented. In the course of those discussions, the influence of the reinforcement has been mentioned. However, in this chapter I will provide an in-depth analysis of the role reinforcement size and morphology play on the mechanical properties and plastic response of metal matrix composites. Theoretical models outlining the role of reinforcement size will be provided for each property. The section on mechanical properties will cover how reinforcement morphology influences material strength, elastic modulus and fatigue behavior while the section following it will

cover the impact of reinforcement size on ductility / fracture and the development of shear bands.

5.2 Size Effects in Mechanical Properties

The role of reinforcement size in the resultant strength of composites was briefly covered in Chapter 3. While the mathematical models were provided in detail, the underlying mechanisms were left for this chapter. In order to make the analysis more convenient, the final forms of the strengthening model equations will be duplicated here. The strengthening mechanisms due to reinforcement are Orowan, isotropic and kinematic strain gradient contributions, and coefficient of thermal expansion mismatch [77, 92, 105, 107] represented by Equations 5.1-5.3 respectively.

$$\Delta\sigma_{Or} = \frac{1.25G_m b \ln(\bar{d}/b)}{\pi\sqrt{1-\nu} \bar{\lambda}} \quad 5.1$$

$$\Delta\sigma_{GND} = kG_m b \sqrt{\frac{8V_p \varepsilon_y}{bd}} \quad 5.2$$

$$\Delta\sigma_{CTE} = \eta G_m b \sqrt{\frac{12V_p \Delta T \Delta CTE}{bd(1-V_p)}} \quad 5.3$$

A condensed version of the strain gradient equations were used to produce Eq. 5.2. It may seem odd that the CTE mismatch is provided here as a strengthening mechanism while it was excluded from Chapter 3. The microstructural basis behind the strengthening

mechanisms, and the reason for the exclusion of CTE strengthening in these aluminum MMCs will now be discussed.

In discontinuously reinforced MMCs the microstructure consists of a comparatively soft metal matrix and hard reinforcement particles. When stress is applied to the material, defects in the form of dislocations move through the matrix along slip planes. If an impenetrable particle lies along the slip plane, then the dislocation must bow around it, as it cannot shear through it. This dislocation bowing takes additional stress, which is what produces the strengthening aspect of Orowan strengthening. The mechanism that takes place as a dislocation bows around an impenetrable particle is shown in Fig. 5.1 [43].

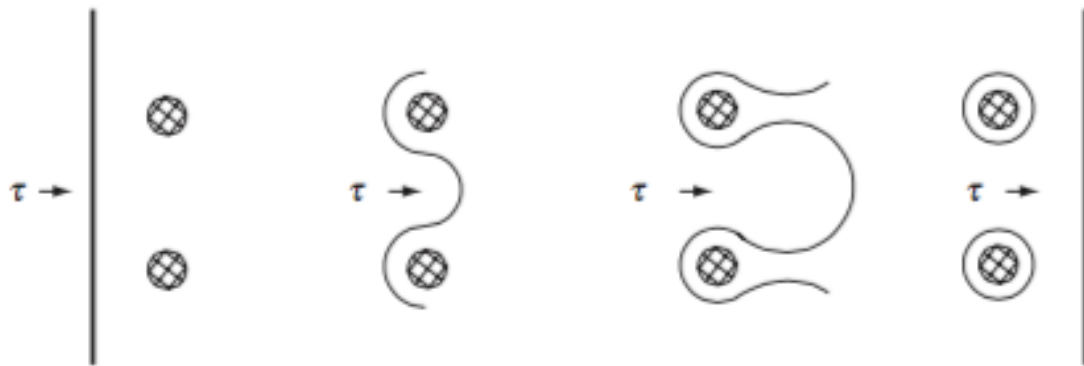


Figure 5.1: A schematic for the process of dislocation bowing and the generation of dislocation loops around small impenetrable particles in a ductile matrix [43].

The stress required to cause this bowing can be estimated through some simple equations and knowledge of the relevant material properties. The energy of a dislocation is generally taken as [43]:

$$U = \frac{Gb^2}{2} \quad 5.4$$

Then, with the assumption that the line tension of a dislocation is equivalent to a bowed dislocation, this can be related to the distance separating two hard particles, that pin the dislocations, R :

$$F = \frac{Gb^2}{2R} \quad 5.5$$

The Peach-Koehler equation is used to relate the force applied to a dislocation to a stress, and it takes the form of $F = \tau b$. Using this relation, and Eq. 5.5, a simple form of the Orowan stress can be determined:

$$\tau = \frac{Gb}{2R} \quad 5.6$$

To get the Orowan strengthening formula used in Eq. 5.1, a modification by Ashby was used that takes into account the particle radius. A TEM image courtesy of Meyers's Mechanical Behavior of Materials showing the activation of dislocation bowing is shown in Fig. 5.2 at locations labeled B.

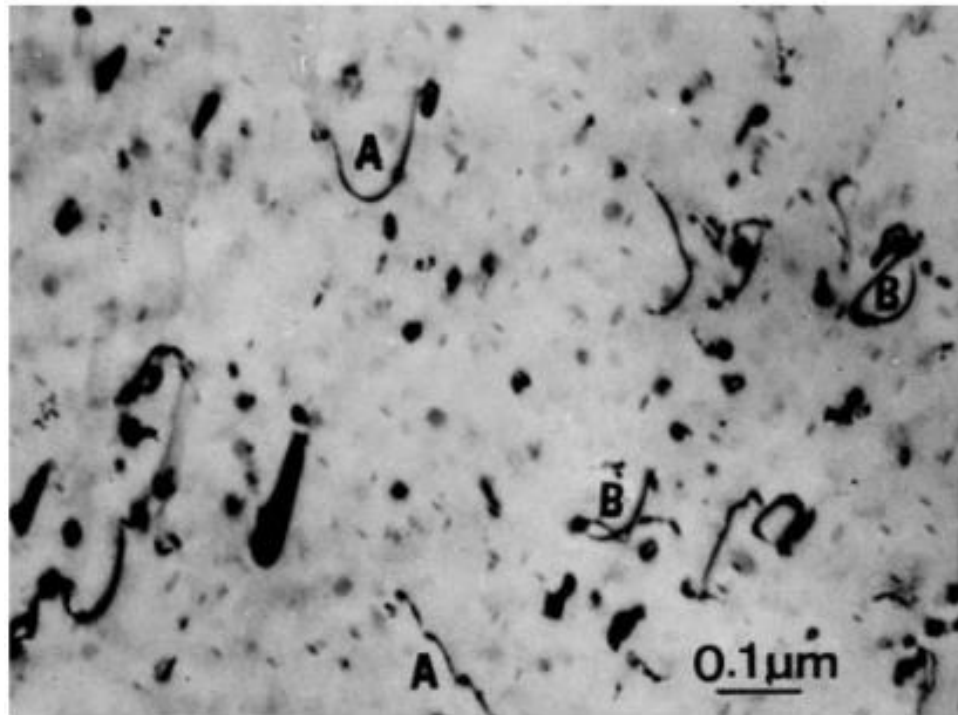


Figure 5.2: A TEM micrograph demonstrating examples of dislocation bowing in an alloy with in-situ particles. Areas labeled *A* show dislocations interacting with the particles while *B* shows the formation of dislocation loops [43].

As can be seen in Fig. 5.2, the particles that cause dislocation bowing are quite small. Not only must the dislocations be able to bow around the particle, there is an additional requirement in that the hard particle must lie within the matrix grains. Reinforcement particles are frequently found at the matrix grain boundaries where it would be unable to interact with mobile dislocations. As a result, Orowan strengthening is often considered in the form of in-situ precipitates that form as a result of heat treatment or other processing techniques [94, 105, 148]. However, when the reinforcement size is small, such as in the case of Al-B₄C-1 composite, the reinforcement may also reside within the grain structure, further contributing to Orowan strengthening

mechanisms. From Eq. 5.1 it can be seen that for a given volume fraction, decreasing the particle size results in an increase in the resultant strengthening which is due to a smaller interparticle spacing.

The next two strengthening mechanisms to be discussed are both a result of dislocations that form due to strains at the matrix-reinforcement interface. Again, these dislocations are activated by deformation of the plastic matrix. However instead of the need for additional stress to move dislocations around small particles, the strengthening is a result of dislocations that become stored at the reinforcement interface [77, 107] and can interfere with other mobile dislocations, resulting in work hardening. The dislocations are stored at the interface to accommodate the difference in the elastic modulus between the two constituents [106]. Since the dislocations are a result of geometric incompatibilities that result from differences in deformation, they are known as geometrically necessary dislocations (GND). A schematic of GNDs forming at a reinforcement interface is shown in Fig. 5.3 [106].

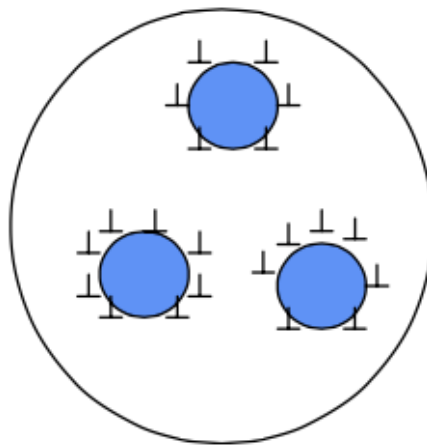


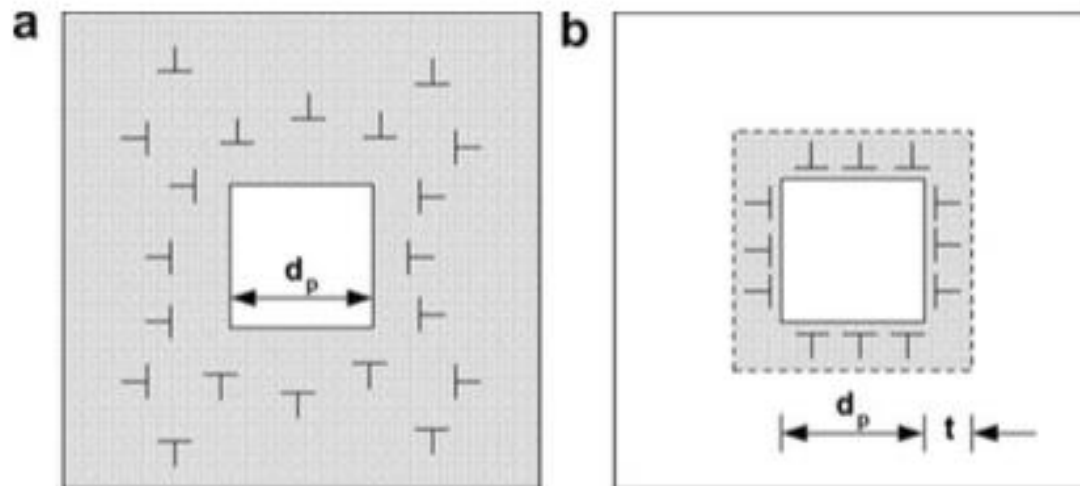
Figure 5.3: A simple schema for the generation of geometrically necessary dislocations at the matrix/particle interface [106].

The dislocation density, and the size dependence, as shown in Eq. 5.2 can be reached through some simple relationships. Since the dislocations that are formed are a result of strain gradients, the population of dislocations will increase proportionally with increasing strain. Additionally, as they form at the particle-matrix interface, the number of dislocations will increase proportionally with particle volume fraction. Taking the reinforcement size into account is also relatively straightforward as decreasing the particle size for a given volume fraction increases the number of interfaces where elastic strain gradients would form.

CTE strengthening is very similar to that of elastic strain-GND strengthening, however the cause of dislocation formation arises not from differences in how the materials respond to strain, but differences in how they respond to thermal changes. Recalling the powder processing route for these composites I discussed in Chapter 2, the composite constituents undergo cryomilling at liquid nitrogen temperatures, before undergoing consolidation at 400 °C and then cooling to room temperature. Due to the high temperature of consolidation, any thermal mismatch dislocations and strains from cryomilling would be relaxed, while those that develop during cooling from 400 °C would become stored. This is the mechanism behind the development of CTE-based dislocations, and while the exact mathematical model is different, comparing Eq. 5.2 and 5.3, there are many similarities.

The interesting aspect is why CTE strengthening does not play a role in the observed composite strengthening of these aluminum MMCs. The answer, as is frequently the case, lies within the microstructure. An investigation by Vogt et al. [166] found that the dislocations actually are being formed at the interface, but they are

confined. They found that around the boron carbide reinforcement, was a layer around 100 – 200 nm thick consisting of small matrix grains, ~40 nm in diameter. Outside of this interface layer, the matrix grains were larger and mostly dislocation free, while inside the layer the small grains had high dislocation densities. In order to determine if they were dislocations formed from elastic strain gradients, they put multiple samples through anneals to relax residual strains and found the dislocations were still there. What appears to be happening is that CTE mismatch dislocations are forming, but they are stopped from spreading further into the metal matrix by the large number of grain boundaries presented by the nanocrystalline grains in the interface layer. Prevented from interacting with the specimen at large, the dislocations are unable to contribute to work hardening or yield strength improvements of the composite. This was verified by performing multiple quenches with varying temperature differentials, which if the CTE mechanism was affecting the specimen at large, would result in different yield strengths. As shown in Fig. 5.4, the yield strength of the composite did not change when varying the quenching temperature. With the findings of Vogt et al. and those by Arsenault [195] that indicate CTE mismatch does not play a role when reinforcements are under 100 nm, it was determined to exclude CTE strengthening from the mechanisms involved in the aluminum MMCs in my study.



Sample	Quenching medium	Initial temperature (°C)	Quenching temperature (°C)	σ_y , 0.2% (MPa)	$\Delta\sigma$ (Eq. (2)) (MPa)	$\Delta\sigma$ (Eq. (4)) (MPa)
As-received	–	450	–	360	–	–
Annealed	Furnace cooled	413	20	369	–	–
				363 (LN ₂ *)		
H ₂ O	Water	413	20	361	43	10
Methanol	Methanol	413	–90	364	49	11
LN ₂	Liquid nitrogen	413	–196	359	53	12
				371 (LN ₂ *)		

* Tested at liquid nitrogen temperature.

Figure 5.4: A diagram for a particle residing in a metal matrix (a) and the dislocations that form around the inclusion (b) leading to a punch out structure. Also shown are the experimental results for the yield strength of aluminum composites with varying quench differentials. The different quenching temperatures should lead to differences in yield strength, but an absence of CTE mismatch hardening is observed instead [166].

Reinforcement materials are frequently used because of the large improvements to material stiffness that they can impart. An improved elastic modulus is significant in airspace frames, and glass fiber reinforced epoxy composites have become widely used. This improved stiffness extends to metal matrix composites as well; however the extent

of elastic modulus improvement is not meaningfully influenced by reinforcement size. Instead, the change in Young's modulus is almost entirely a result of reinforcement volume fraction, with some influence resulting from reinforcement morphology. A model from Ravichandran characterizes the relationship between the reinforcement volume fraction and the resultant change in composite stiffness [196]:

$$c = \left[\frac{1}{V_p} \right]^{1/3} - 1 \quad 5.7$$

$$E_c = \frac{(cE_p E_m + E_m^2)(1+c)^2 - E_m^2 + E_p E_m}{(cE_p + E_m)(1+c)^2} \quad 5.8$$

where c is a non-dimensional quantity describing the unit cell, while E_m and E_p are the elastic moduli of the matrix and particle respectively. I have decided to include the elastic modulus in this chapter despite its size independence, as the elastic modulus and the reinforcement size both influence the fatigue behavior of composites.

The fatigue behavior of materials is an important characteristic for many structural applications. Considering the impressive mechanical properties of MMCs, it is not surprising that the fatigue behavior of aluminum and magnesium discontinuously reinforced MMCs has been well studied. Studies by Chawla [168], Vaidya [197], Ding [198], and Hall [199] all found the same relations between reinforcement particle size, volume fraction of reinforcement and fatigue behavior. As the particle size decreases, and as the volume fraction of the reinforcement increases, the fatigue performance improves. The relation can be easily seen in Figure 5.5 from Hall, showing the results of tests performed on aluminum 2124 reinforced with SiC particles.

Similar results were found by Vaidya [197] in his investigation on magnesium reinforced with SiC particles. However, his analysis went further, using not only S-N fatigue behavior, but also elastic strain amplitude, which is the stress amplitude normalized by the elastic modulus. When normalized by the elastic modulus, the composites no longer exhibit improved fatigue behavior as compared to the monolithic magnesium alloy (Fig. 5.6). The improved fatigue properties of composites are therefore directly related to the elastic modulus improvement imparted by the reinforcing material. Referring back to Eq. 5.8, the dependence of fatigue behavior on the volume fraction of reinforcing material corresponds to the volume fraction dependence of the elastic modulus improvement. Somewhat less clear is the relationship between fatigue behavior and reinforcement size.

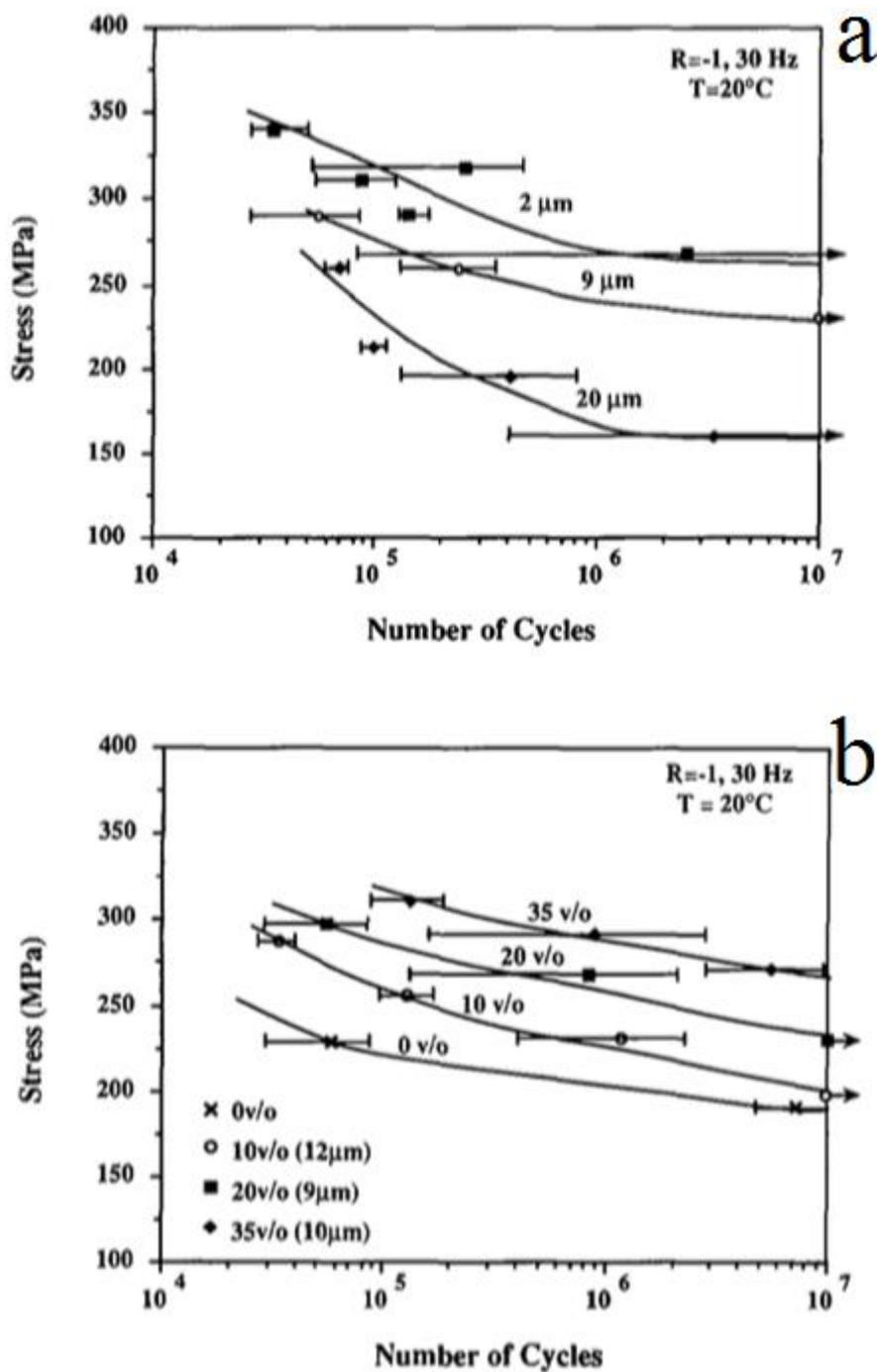


Figure 5.5: The improved fatigue behavior for an aluminum alloy reinforced with SiC is shown in terms of reinforcement size (a) and volume fraction of loading (b) [199].

The answer lies in the microstructural damage that occurs during fatigue cycle loading and the effect of reinforcement size on the critical condition resulting in unstable fatigue crack propagation [198]. The damage that is done to the microstructure is primarily a result of the formation of fatigue cracks and their progression through the specimen. Most investigations report that the fatigue crack growth is independent of particle size [81, 200, 201], while both the threshold for fatigue crack growth and the fatigue strength are influenced by particle size. An exception to this generally accepted relation is given by Arsenault and Flom who found that propagation fracture toughness increases with larger reinforcement size. Their explanation was that when the particle size is larger there is greater interparticle spacing, which allows for more plastic deformation to be accommodated by the matrix [195]. Some great work in this area has been done by Allison and Jones [200] including findings that powder metallurgy composite fatigue shows improvements over ingot metallurgy techniques.

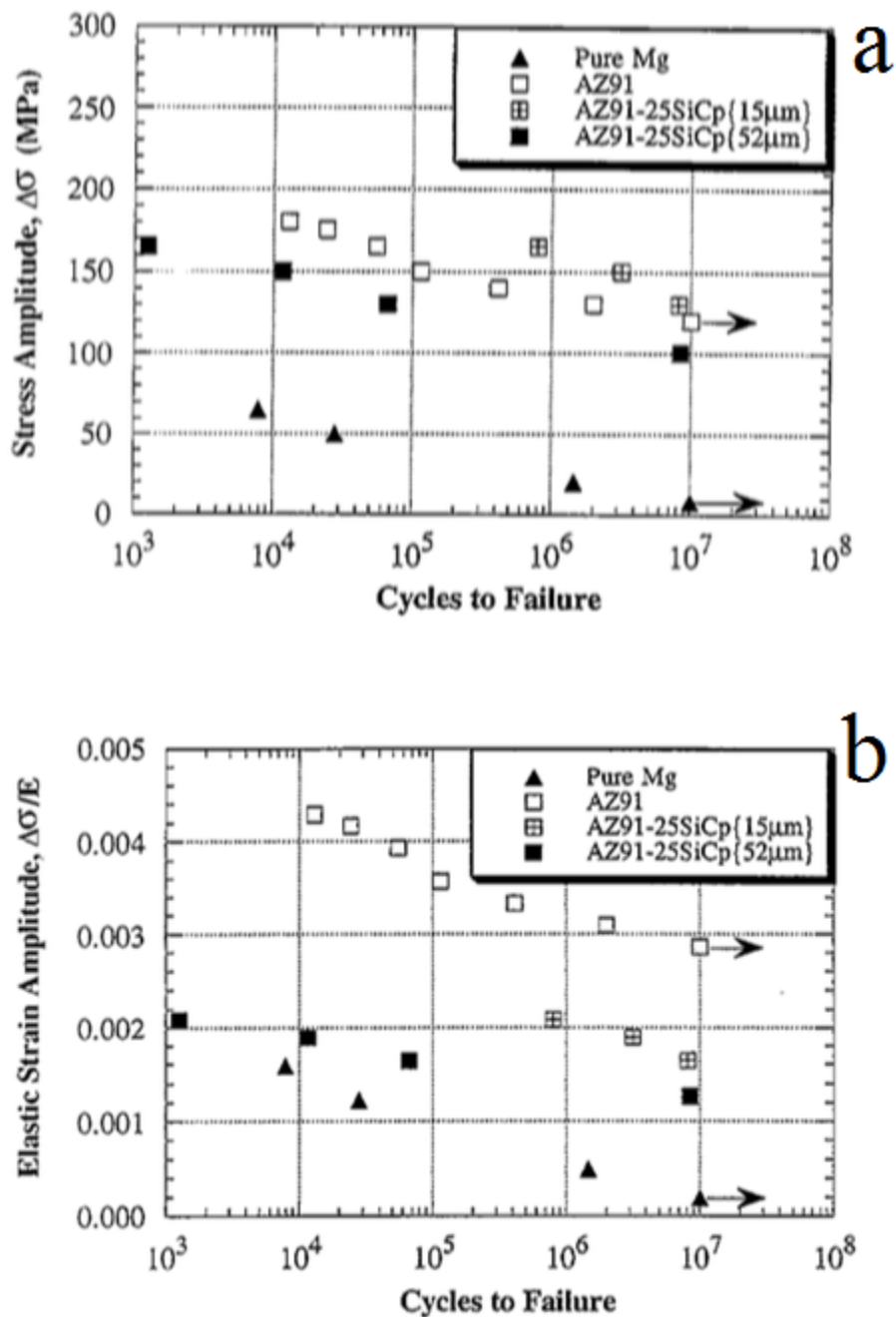


Figure 5.6: The S-N (a) and elastic strain amplitude (b) curves for a magnesium MMC reinforced with SiC. While (a) would indicate that the 15 μm SiC reinforcement produces superior performance, when the results are normalized by the elastic modulus, it is seen that the AZ91 alloy actually exhibits the best performance [197].

A model to determine composite fatigue strength and the development of fatigue damage has been developed by Ding and Biermann [198]. The model accurately reflects experimental trends and the influence of reinforcement size and volume fraction on fatigue behavior. In this model, the progression of fatigue cracks in the microstructure is represented by a fatigue-damaged region. It is assumed that the growth of this region follows Paris' law [198], relating the stress intensity factor ΔK to the crack growth rate:

$$\frac{da}{dN} = K(a) = A\Delta K^n = A(Y\Delta\sigma/2)^n a^{n/2} \quad 5.9$$

In Eq. 5.9, $\frac{da}{dN}$ is the growth of the fatigue-damaged region per cycle, A and n are material constants, Y is a geometric correction factor for the crack, a is the size of the fatigue-damaged area, and $\Delta\sigma/2$ is the cyclic stress amplitude. Using a method from Hahn and Rosenfield [202], the fatigue fracture toughness can be calculated by the following failure criterion:

$$K_{IC} = (2\sigma_{ys}E \times CTOD)^{1/2} \quad 5.10$$

where σ_{ys} is the matrix yield strength, and the crack tip opening displacement (CTOD), represents a region of large deformation. In the analysis presented here, the CTOD is replaced with the length of the matrix between particles that have decohered near the crack-tip, meaning that Eq. 5.10 can be modified to:

$$K_{IC} = \left[2\sigma_{ys} E (\pi / 6)^{1/3} d_p \right]^{1/2} f_p^{-1/6} \quad 5.11$$

In Eq. 5.11, d_p is the particle size and f_p is the particle volume fraction, while E is the Young's modulus of the matrix. Then, the critical condition where a fatigue crack will propagate unstably is given by rearranging Paris' law (Eq. 5.9) to give:

$$a(\Delta\sigma / 2) = \left(\frac{K_{IC}}{Y\Delta\sigma / 2} \right)^2 = \frac{2\sigma_{ys} E (\pi / 6)^{1/3} d_p}{(Y\Delta\sigma / 2)^2 f_p^{1/3}} \quad 5.12$$

So from Eq. 5.12 we can see the influence of both the reinforcement particle size and the volume fraction of the reinforcement on the final stages of fatigue crack growth.

Decreasing the reinforcement size and increasing the particle volume fraction, with particle size as the dominant factor, can delay unstable crack growth. Due to the involved nature of its derivation, the full model for the fatigue strength will not be presented though it is available in [198], however, a comparison of the model to experimental data is provided in Figure 5.7. While there have been many studies regarding the influence of reinforcement size on mechanical properties, there is a significant lack of studies of that nature for reinforcements in the nanoscale. Such a study would be of significant value as MMCs with nanometric reinforcement become more easily available.

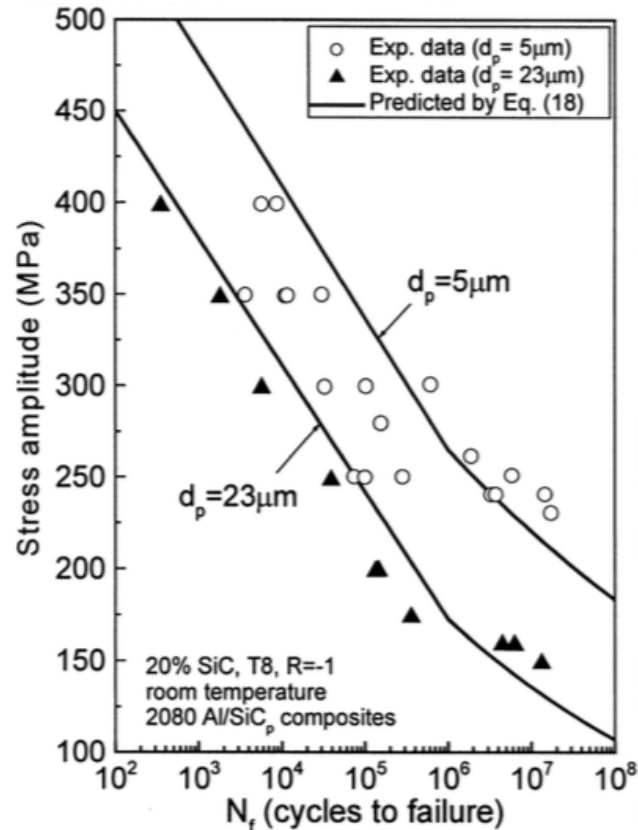


Figure 5.7: Comparison of the model from Ding [198] to experimental results, trying to understand and predict the size effect of the reinforcement on fatigue performance.

5.3 Influence of Reinforcement Size on Plastic Response

In UFG metals the plastic response is primarily determined by how much plastic strain the matrix can accommodate. When grains are more refined there are a greater number of grain boundaries, which act as barriers to dislocation movement, as well as sinks for dislocations. However, the rapid generation and annihilation of dislocations means that little strain hardening can occur and as a result the Considère criterion is fulfilled rapidly and strain localization occurs shortly after yielding and plastic deformation quickly results in failure. Improvements can therefore be made by

introducing larger grains into the microstructure to aid in deformation, other methods such as low temperature deformation can also help [203].

In discontinuously reinforced composites however, plastic response and the onset of failure is only determined by the microstructural damage incurred by the reinforcement [188]. The matrix composition will of course influence the resultant performance of the composite, however if the matrix is taken as a constant, the parameter of interest is the rate of microstructural damage. This damage takes three primary forms, nucleation of voids at the matrix-particle interface such as that discussed in Chapter 4 and the previous section, particle cracking [183] and clustering effects [35]. Since clustering is largely volume fraction sensitive and not particle size sensitive it is being left out of this discussion, especially as the volume fraction of reinforcement was constant in both Al-B₄C-1 and Al-B₄C-2. Additionally, as the effect of particle size on void nucleation was discussed in the previous section, I will focus on the influence of reinforcement size on particle cracking. Ceramic particle cracking can be considered to occur when the Griffith criterion is exceeded [77]:

$$\sigma_c^p = K / \sqrt{d} \quad 5.13$$

In Eq. 5.13 K is related to the fracture toughness of the particle as well as some geometric considerations, and σ_c^p is the stress required to crack the particle. What is readily apparent from Eq. 5.13 is that as the particle size decreases, a greater stress is required to cause particle cracking. This is beneficial to composite performance as particle cracking leads to a decrease in composite yield strength and additional sites for fracture initiation [183]. As pointed out by Nan and Clarke [77], when the flow strength is reduced, this

leads to the Considère criterion being fulfilled at a lower strain and earlier strain instability. Fig. 5.8a shows the increase of particle cracking with increasing particle size as well as the earlier onset of plastic instability. While the difference in strain localization in Fig. 5.8b is depicted as due to the volume fraction of reinforcement, the cause of the change is the increased particle cracking that occurs at greater volume fractions and larger particle sizes.

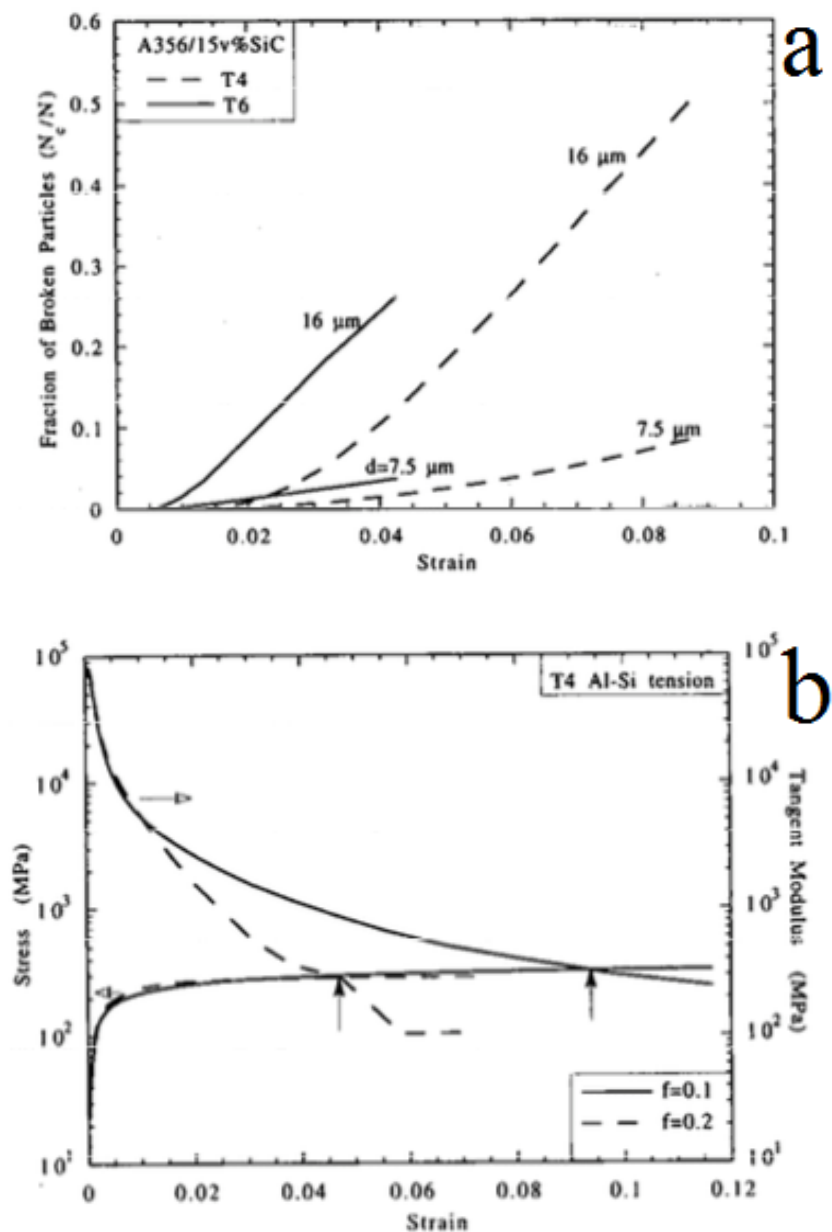


Figure 5.8: Comparison of damage mechanisms occurring in MMCs with (a) depicting the fraction of broken reinforcement as a function of strain and particle size. When the loading of the reinforcement is increased, it is shown to reduce the strain at which the Considère criterion is fulfilled (b). This is primarily due to an increase in the number of sites for void nucleation or particle cracking [77].

While particle cracking is a common damage mechanism in discontinuously reinforced composites, it is primarily active under tensile loading. As the MMCs studied in this dissertation have not yet undergone tensile testing, it is unclear if the order of magnitude size difference between the reinforcements would lead to a difference in global particle fracture. Considering the values of K used in Nan and Clarke for SiC and Si in heat-treated aluminum matrices, of $2.4 \text{ MPa}\sqrt{m}$ and $2.8 \text{ MPa}\sqrt{m}$, a modest estimate for B_4C in an UFG matrix could be around $3 \text{ MPa}\sqrt{m}$. Using a K of 3 in Eq. 5.13 along with the particle sizes used in Al- B_4C -1 and -2, fracture stresses of 15 GPa and ~ 4.3 GPa are obtained. Matrix yielding would occur well before tensile loads on the particle reinforcement could reach the stresses necessary for particle cracking. This would need to be experimentally verified, but following the Griffith's criterion, particles under $1 \text{ }\mu\text{m}$ would be unexpected to fracture, unless their K was low as a result of poor toughness or geometrical complications. This means that the most important mechanism in the evolution of microstructural damage in these MMCs comes from the nucleation of voids or micro-cracks at the particle-matrix interface. Not only can these micro-cracks coalesce leading to fracture, they also assist in the formation of plastic instabilities in the form of ASBs.

ASB formation is the result when a plastic instability forms and propagates through a material. Consequently, ASB formation is primarily dependent upon the material properties of the matrix material in a composite. As covered in Chapter 3, factors such as strain hardening, thermal softening and specific heat capacity all affect the susceptibility of a material to ASB formation with strain hardening assisting in retardation of ASB formation while high thermal softening and low specific heat capacity

increase the likelihood of formation [204]. The material properties of the reinforcement are therefore less important to ASB formation than how the reinforcement affects the matrix.

In an attempt to quantify how the size of the reinforcement affects the propensity of a DR MMC to form ASB, Yilong Bai et al. [205] developed a strain gradient-dependent shear instability criterion. The strain gradient constitutive equation takes the form:

$$\sigma_c = \sigma_m (1 + \hat{l}\eta)^{\nu} \quad 5.14$$

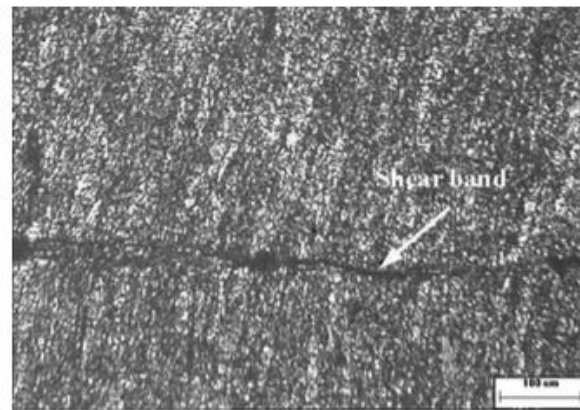
where σ_c and σ_m are the yield strength of the composite and matrix respectively, ν is a dimensionless constant, and $\hat{l} = 3a^2b(G_m / \sigma_m)^2$ is a material length with a as a dimensionless parameter. η is the effective strain gradient (Fleck 1997):

$$\eta = \sqrt{c_1 \eta_{iik} \eta_{ijk} + c_2 \eta_{ijk} \eta_{ijk} + c_3 \eta_{ijk} \eta_{kji}} \quad 5.15$$

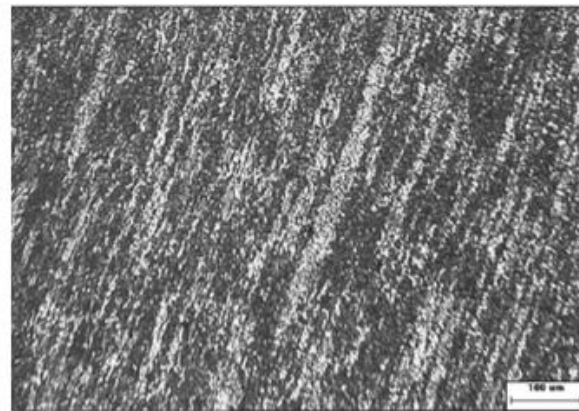
where c_1, c_2, c_3 are the effective strain gradients and η_{ijk} are the incompressible third rank strain gradient tensors. The effective strain gradient is a measure of the number of geometrically necessary dislocations for compatible deformation with dissimilar materials. The three constants are given by:

$$\begin{aligned}
c_1 &= \frac{1}{4} \left(1 + \frac{2f_p}{d_p} \right)^2 - \frac{1}{6} \left(1 + \frac{4f_p}{d_p} \right)^2 - \frac{1}{12} \\
c_2 &= \frac{1}{6} \left(1 + \frac{4f_p}{d_p} \right)^2 + \frac{1}{12} \\
c_3 &= -\frac{1}{6} \left(1 + \frac{4f_p}{d_p} \right)^2 + \frac{1}{6}
\end{aligned} \tag{5.16}$$

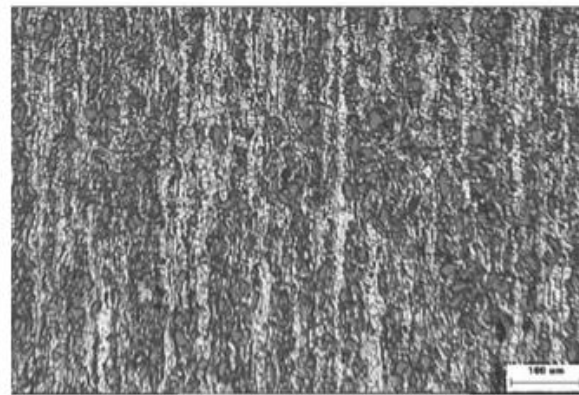
In Eq. 5.16 l is on the order of unity and f_p and d_p are the volume fraction and size of the reinforcement respectively. As can be seen from Eq. 5.16, decreasing the particle size and increasing the volume fraction will increase the strain gradient. When the strain gradient increases, the flow stress of the composite increases and additional plastic work is dissipated resulting in greater heat and thermal softening [205]. Experimental evidence in the literature supports this analysis [169, 206]. In the aluminum MMCs studied in this dissertation, there is not a clear difference in the propensity for ASB formation. Since both reinforcements are under 1 μm and the literature shows that when the reinforcement is under 3 μm [175, 205] (Fig. 5.9), ASB formation is able to proceed, any difference may be too small to observe experimentally.



(a) $d_p = 3.5 \mu m$



(b) $d_p = 10 \mu m$



(c) $d_p = 20 \mu m$

Figure 5.9: Post-loading micrographs depicting the dependence of shear band formation on the size of the reinforcing particles. When the particles are larger they “get in the way” and impede the formation of ASB. However, once the reinforcement is small enough ASB formation can proceed (a) [205].

5.4 Conclusion

In this chapter, the influence of the reinforcement size on various mechanical properties has been examined. Reinforcement size has a considerable impact on composite strength with improvements stemming from elastic modulus mismatch and the generation of GNDs, and when the reinforcement is small enough as is the case in Al-B₄C-1, Orowan strengthening can also play a role. While the particle size does not change the elastic modulus, it does influence the fatigue behavior of composites. It was found that by decreasing the size of the reinforcement gains could be made in the fatigue strength and fatigue life.

The matrix primarily determines the plastic response of a MMC, and as such reinforcement size effects only affect behavior by how they change the matrix microstructure. For instance, larger particles are more prone to cracking under tension which decreases fracture toughness and makes plastic instability more likely. However, as shown in Chapter 4, when the reinforcement size is decreased it also greatly increases the number of sites available for void nucleation. Adiabatic shear band formation is likewise promoted when the particle size is reduced. With the exception of particle cracking and fatigue performance which have not yet been investigated, the experimental work performed in this investigation has been in agreement with the literature and the theoretical models proposed.

CHAPTER 6: SUMMARY

As the aluminum industry has expanded and aluminum alloys and composites have become more widespread, the development of new materials for demanding applications has flourished. However, in order for them to be implemented, they must be fully characterized so that their behavior is understood and predictable. The impetus of this dissertation was to investigate the microstructure and mechanical performance of a novel, nanostructured aluminum MMC and the influence of the reinforcement size on its behavior. The MMC under investigation consisted of a cryomilled Al 5083 matrix reinforced with 5 vol.% boron carbide with an approximate diameter of either 50 nm or 500 nm.

The microstructural characterization that was performed determined that the UFG matrix formed during cryomilling persisted through subsequent consolidation. Nitrides that formed during cryomilling along with the nanometric boron carbide acted as pinning sites at grain boundaries. The dynamic compression tests performed with the Kolsky bar system revealed that the addition of boron carbide resulted in a significant improvement to the yield stress, with a 30% improvement over the unreinforced alloy. In addition to providing increased thermal stability, the nitrides and reinforcement produced increased material strength in the form of Orowan strengthening. This mechanism resulted in the Al-B₄C-1 having a slightly higher strength than Al-B₄C-2 while producing more sites for

void nucleation resulting in more severe strain softening. Nanoindentation hardness tests confirmed the yield strengths found during dynamic testing, and strain rate jump tests found the increased sensitivity common to UFG aluminum was also present. However, it was also found that when extended to high strain rates, the SRS was less pronounced.

Post-loading analysis of the specimens found that the composites formed adiabatic shear bands after undergoing dynamic compression, while ASB were not formed during quasi-static loading. The unreinforced alloy did not form ASB at either quasi-static or dynamic strain rates, but did exhibit inhomogeneous deformation at high strain rates. The formation of ASB in the composites is consistent with the ASB toughness model proposed by Grady, as the higher yield stress of the composites would make them more susceptible than the alloy. In addition, the numerous nucleation sites provided by the reinforcement make strain localization much more likely.

Finally, elevated temperature dynamic compression experiments were performed on the composite samples to determine their high temperature performance. The composites maintained moderately high strength and stiffness even at 673 K, but the severe strain softening they exhibited indicates that any plastic deformation will rapidly deteriorate the mechanical behavior. Comparing the response of the two composites, it was found that Al-B₄C-1 exhibited greater flow softening than Al-B₄C-2 at all temperatures, though at 573 K and above, the rate of strain softening was approximately equivalent.

The findings of this investigation can be summarized as follows:

- A novel nanostructured MMC tested at both quasi-static and dynamic strain rates and was found to exhibit impressive strength compared to the unreinforced alloy.

- Strain rate sensitivity was found to increase with decreasing grain size at quasi-static strain rates, while SRS was reduced at high strain rates.
- Elevated temperature compression tests determined that while the microstructure has good thermal stability, the composites undergo significant strain softening at elevated temperatures.
- The size of the reinforcement played a role in many mechanical behaviors, with decreased particle size linked to increased strength, significantly improved plastic response at quasi-static strain rates, and a higher strain softening rate.

The composites studied in the course of this investigation exhibit improved mechanical properties as a result of their processing and reduced reinforcement size. While there are still many forms of characterization required before they could be considered for commercial applications, what has been revealed so far has been promising.

CHAPTER 7: FUTURE WORK

While many areas have been characterized in the course of my dissertation, there are still aspects that require additional investigation, and some of those are summarized in this chapter.

Although compressive tests have been performed at both quasi-static and dynamic strain rates, the tensile behavior of the composites has yet to be studied. At present this has not been performed as the samples are of very small dimensions, and we do not possess a micro-tensile testing setup. However, valuable information would be obtained from tensile tests such as differences in deformation and if the prediction that particle cracking would not occur due to their small size proves correct. This is a core characterization technique and one of the most important areas for future study.

Aluminum 5083, and aluminum alloys in general are known for their low temperature performance. Now that the elevated temperature response of these composites has been studied it would be beneficial to test their cryogenic temperature properties. Due to the reinforcement particles, it is possible that the composites would no longer perform as well at cryogenic temperatures, instead suffering from early fracture as a result of void nucleation and coalescence.

REFERENCES

- [1] Ross M. *Contemporary Physics*. 2010;38:381.
- [2] Peeters PM, Middel J, Hoolhorst A. National Aerospace Laboratory NLR. 2005;
- [3] Brooker A, Ward J, Wang L. SAE International. 2013;
- [4] Dyer E. Why Ford Reinvented the Best-Selling Vehicle in America. vol. 2015. <http://www.popularmechanics.com/cars/trucks/a15139/aluminum-ford-fl150>, 2015.
- [5] Dursun T, Soutis C. *Materials & Design*. 2014;56:862.
- [6] Industry Statistics. The Aluminum Association, 2014. p.2.
- [7] Administration IT. Steel Industry Executive Summary. [http://hq-web03.ita.doc.gov/License/Surge.nsf/webfiles/SteelMillDevelopments/\\$file/execsumm.pdf?openelement](http://hq-web03.ita.doc.gov/License/Surge.nsf/webfiles/SteelMillDevelopments/$file/execsumm.pdf?openelement): U.S. Department of Commerce, 2015.
- [8] Stankovich S, Dikin DA, Dommett GHB, Kohlhaas KM, Zimney EJ, Stach EA, Piner RD, Nguyen ST, Ruoff RS. *Nature*. 2006;442:282.
- [9] Breuer O, Sundararaj U. *Polymer Composites*. 2004;25:630.
- [10] Thostenson ET, Ren ZF, Chou TW. *Composites Science and Technology*. 2001;61:1899.
- [11] Bledzki AK, Gassan J. *Prog. Polym. Sci*. 1999;24:221.
- [12] Scott JM, Phillips DC. *Journal of Materials Science*. 1975;10:551.
- [13] Hancox NL. *Journal of Materials Science*. 1975;10:234.
- [14] Witte F, Feyerabend F, Maier P, Fischer J, Stoermer M, Blawert C, Dietzel W, Hort N. *Biomaterials*. 2007;28:2163.
- [15] Yang Y, Lan J, Li XC. *Mater. Sci. Eng. A-Struct. Mater. Prop. Microstruct. Process*. 2004;380:378.
- [16] Zhang XN, Lu WJ, Zhang D, Wu RJ, Bian YJ, Fang PW. *Scripta Materialia*. 1999;41:39.
- [17] Venkataraman B, Sundararajan G. *Acta Mater*. 1996;44:461.
- [18] Deuis RL, Subramanian C, Yellup JM. *Wear*. 1996;201:132.

- [19] Furuya Y, Sasaki A, Taya M. *Mater. Trans. JIM*. 1993;34:224.
- [20] Chen YM, Ting JM. *Carbon*. 2002;40:359.
- [21] Perera SD, Patel B, Nijem N, Roodenko K, Seitz O, Ferraris JP, Chabal YJ, Balkus KJ. *Advanced Energy Materials*. 1:936.
- [22] Coleman JN, Khan U, Blau WJ, Gun'ko YK. *Carbon*. 2006;44:1624.
- [23] Dalton AB, Collins S, Munoz E, Razal JM, Ebron VH, Ferraris JP, Coleman JN, Kim BG, Baughman RH. *Nature*. 2003;423:703.
- [24] Haggemueller R, Gommans HH, Rinzler AG, Fischer JE, Winey KI. *Chemical Physics Letters*. 2000;330:219.
- [25] Shaffer MSP, Windle AH. *Advanced Materials*. 1999;11:937.
- [26] Schadler LS, Giannaris SC, Ajayan PM. *Applied Physics Letters*. 1998;73:3842.
- [27] Campbell FC. *Manufacturing Technology for Aerospace Structural Materials*, Elsevier Ltd., Elsevier Inc, San Diego CA, USA, 2006.
- [28] Miracle DB. *Composites Science and Technology*. 2005;65:2526.
- [29] Naseri M, Hassani A, Tajally M. *Ceramics International*. 2015;41:3952.
- [30] Feng GH, Yang YQ, Luo X, Li J, Huang B, Chen Y. *Composites Part B-Engineering*. 2015;68:336.
- [31] Ekici R, Kaburcuk M. *J. Compos Mater*. 2015;49:853.
- [32] Zhou ZS, Wu GH, Jiang LT, Li RF, Xu ZG. *Materials & Design*. 2014;63:658.
- [33] Vogt RG, Zhang Z, Topping TD, Lavernia EJ, Schoenung JM. *Journal of Materials Processing Technology*. 2009;209:5046.
- [34] Zhang H, Ye J, Joshi SP, Schoenung JM, Chin ESC, Ramesh KT. *Scripta Materialia*. 2008;59:1139.
- [35] Hong SJ, Kim HM, Huh D, Suryanarayana C, Chun BS. *Mater. Sci. Eng. A-Struct. Mater. Prop. Microstruct. Process*. 2003;347:198.
- [36] Thilly T, Veron M, Ludwig O, Lecouturier F. *Mater. Sci. Eng. A-Struct. Mater. Prop. Microstruct. Process*. 2001;309:510.

- [37] Semiatin SL, Jata KV, Uchic MD, Berbon PB, Matejczyk DE, Bampton CC. *Scripta Materialia*. 2001;44:395.
- [38] Friedrich Wohler. <http://www.chemheritage.org/discover/online-resources/chemistry-in-history/themes/molecular-synthesis-structure-and-bonding/liebig-and-wohler.aspx>: Chemical Heritage Foundation.
- [39] Binczewski G. *JOM*. 1995;47:20.
- [40] Charles Hall. <http://www.chemheritage.org/discover/online-resources/chemistry-in-history/themes/electrochemistry/heroult-hall-hall.aspx>: Chemical Heritage Foundation.
- [41] Habashi F. *Bulletin for the History of Chemistry*. 1995;17:
- [42] Davis J. *ASM International*. 1999;
- [43] Meyers MA, Chawla K. *Mechanical Behavior of Materials*. 2nd ed., Cambridge University Press, Cambridge University Press, New York, 2009.
- [44] Davis J. *ASM Specialty Handbook: Aluminum and Aluminum Alloys*, ASM International, Materials Park, OH, 1994.
- [45] Twite RL, Bierwagen GP. *Progress in Organic Coatings*. 1998;33:91.
- [46] Mishra B, Mondal C, Goyal R, Ghosal P, Kumar KS, Madhu V. *Mater. Sci. Eng. A-Struct. Mater. Prop. Microstruct. Process*. 2014;612:343.
- [47] Ryen O, Nijs O, Sjolander E, Holmedal B, Ekstrom HE, Nes E. *Metallurgical and Materials Transactions a-Physical Metallurgy and Materials Science*. 2006;37A:1999.
- [48] Polmear IJ. *Mater. Trans. JIM*. 1996;37:12.
- [49] Suryanarayana C, Ivanov E, Boldyrev VV. *Mater. Sci. Eng. A-Struct. Mater. Prop. Microstruct. Process*. 2001;304:151.
- [50] Murty BS, Kori SA, Chakraborty M. *Int. Mater. Rev*. 2002;47:3.
- [51] McCartney DG. *Int. Mater. Rev*. 1989;34:247.
- [52] Qin Y, Chen L, Shen H. *Journal of Alloys and Compounds*. 1997;256:230.
- [53] Murayama M, Hono K. *Acta Mater*. 1999;47:1537.
- [54] Edwards GA, Stiller K, Dunlop GL, Couper MJ. *Acta Mater*. 1998;46:3893.

- [55] Manoharan M, Lewandowski JJ. *Scripta Metallurgica*. 1989;23:301.
- [56] Ardell AJ. *Metallurgical Transactions a-Physical Metallurgy and Materials Science*. 1985;16:2131.
- [57] Smith WF. ASM International. 1979;
- [58] Zhao YH, Liao XZ, Jin Z, Valiev RZ, Zhu YT. *Acta Mater*. 2004;52:4589.
- [59] Mott NF, Nabarro FRN. *Proceedings of the Physical Society*. 1940;52:86.
- [60] Valiev RZ, Langdon TG. *Prog. Mater. Sci*. 2006;51:881.
- [61] Han BQ, Lee Z, Witkin D, Nutt S, Lavernia EJ. *Metallurgical and Materials Transactions a-Physical Metallurgy and Materials Science*. 2005;36A:957.
- [62] Verma R, Friedman PA, Ghosh AK, Kim S, Kim C. *Metallurgical and Materials Transactions a-Physical Metallurgy and Materials Science*. 1996;27:1889.
- [63] Garcia-Bernal MA, Mishra RS, Verma R, Hernandez-Silva D. *Mater. Sci. Eng. A-Struct. Mater. Prop. Microstruct. Process*. 2015;636:326.
- [64] Singh D, Rao PN, Jayaganthan R. *Materials Science and Technology*. 2014;30:1835.
- [65] Rokni MR, Widener CA, Nardi AT, Champagne VK. *Applied Surface Science*. 2014;305:797.
- [66] Gubicza J, Chinh NQ, Horita Z, Langdon TG. *Mater. Sci. Eng. A-Struct. Mater. Prop. Microstruct. Process*. 2004;387:55.
- [67] Chang SY, Lee JG, Park KT, Shin DH. *Materials Transactions*. 2001;42:1074.
- [68] Park KT, Park JH, Lee YS, Nam WJ. *Mater. Sci. Eng. A-Struct. Mater. Prop. Microstruct. Process*. 2005;408:102.
- [69] Lee YB, Shin DH, Park KT, Nam WJ. *Scripta Materialia*. 2004;51:355.
- [70] Park KT, Hwang DY, Chang SY, Shin DH. *Metallurgical and Materials Transactions a-Physical Metallurgy and Materials Science*. 2002;33:2859.
- [71] Verma R, Ghosh AK, Kim S, Kim C. *Mater. Sci. Eng. A-Struct. Mater. Prop. Microstruct. Process*. 1995;191:143.

- [72] Metal Matrix Composites in the 21st Century: Markets and Opportunities. <http://www.bccresearch.com/market-research/advanced-materials/AVM012B.html>, 2000.
- [73] BCCResearch. Metal Matrix Composites: The Global Market. <http://www.bccresearch.com/market-research/advanced-materials/metal-matrix-composites-market-avm012d.html>, 2009.
- [74] Ranganath S. Journal of Materials Science. 1997;32:1.
- [75] Lloyd DJ. Int. Mater. Rev. 1994;39:1.
- [76] Ibrahim IA, Mohamed FA, Lavernia EJ. Journal of Materials Science. 1991;26:1137.
- [77] Nan CW, Clarke DR. Acta Mater. 1996;44:3801.
- [78] Vargas-Gonzalez L, Speyer RF, Campbell J. International Journal of Applied Ceramic Technology. 2010;7:643.
- [79] Becher PF. Journal of the American Ceramic Society. 1991;74:255.
- [80] Ramnath BV, Elanchezhian C, Jaivignesh M, Rajesh S, Parswajinan C, Ghias ASA. Materials & Design. 2014;58:332.
- [81] Shang JK, Yu WK, Ritchie RO. Mater. Sci. Eng. A-Struct. Mater. Prop. Microstruct. Process. 1988;102:181.
- [82] Nardone VC, Prewo KM. Scripta Metallurgica. 1986;20:43.
- [83] Fu S-Y, Feng X-Q, Lauke B, Mai Y-W. Composites Part B-Engineering. 2008;39:933.
- [84] Li Q, Li F, Xia T, Lan Y, Jian Y, Tao F. Journal of Alloys and Compounds. 2015;627:352.
- [85] Sairam K, Sonber JK, Murthy T, Subramanian C, Hubli RC, Suri AK. International Journal of Refractory Metals & Hard Materials. 2012;35:32.
- [86] Zhang ZH, Topping T, Li Y, Vogt R, Zhou YZ, Haines C, Paras J, Kapoor D, Schoenung JM, Lavernia EJ. Scripta Materialia. 2011;65:652.
- [87] Gopalakrishnan S, Murugan N. Materials & Design. 2011;32:462.
- [88] Paliwal B, Ramesh KT. Journal of the Mechanics and Physics of Solids. 2008;56:896.

- [89] Ye J, Han BQ, Lee Z, Ahn B, Nutt SR, Schoenung JM. *Scripta Materialia*. 2005;53:481.
- [90] Tang F, Hagiwara A, Schoenung JA. *Mater. Sci. Eng. A-Struct. Mater. Prop. Microstruct. Process.* 2005;407:306.
- [91] Zhang H, Ramesh KT, Chin ESC. *Mater. Sci. Eng. A-Struct. Mater. Prop. Microstruct. Process.* 2004;384:26.
- [92] Kang YC, Chan SLI. *Materials Chemistry and Physics.* 2004;85:438.
- [93] Spowart JE, Miracle DB. *Mater. Sci. Eng. A-Struct. Mater. Prop. Microstruct. Process.* 2003;357:111.
- [94] Han BQ, Lee Z, Nutt SR, Lavernia EJ, Mohamed FA. *Metallurgical and Materials Transactions a-Physical Metallurgy and Materials Science.* 2003;34:603.
- [95] Shao I, Vereecken PM, Chien CL, Searson PC, Cammarata RC. *J. Mater. Res.* 2002;17:1412.
- [96] Clyne TW, Mason JF. *Metallurgical Transactions a-Physical Metallurgy and Materials Science.* 1987;18:1519.
- [97] Hashim J, Looney L, Hashmi MSJ. *Journal of Materials Processing Technology.* 2001;119:324.
- [98] Rajan TPD, Pillai RM, Pai BC. *Journal of Materials Science.* 1998;33:3491.
- [99] Clyne TW, Bader MG, Cappleman GR, Hubert PA. *Journal of Materials Science.* 1985;20:85.
- [100] Ogawa F, Masuda C. *Composites Part a-Applied Science and Manufacturing.* 2015;71:84.
- [101] Scudino S, Liu G, Sakaliyska M, Surreddi KB, Eckert J. *Acta Mater.* 2009;57:4529.
- [102] Webster D, Wald G, Cremens WS. *Metallurgical Transactions a-Physical Metallurgy and Materials Science.* 1981;12:1495.
- [103] Iseki T, Kameda T, Maruyama T. *Journal of Materials Science.* 1984;19:1692.
- [104] Yin WH, Xu F, Ertorer O, Pan Z, Zhang XY, Kecskes LJ, Lavernia EJ, Wei Q. *Acta Mater.* 2013;61:3781.
- [105] Cao BY, Joshi SP, Ramesh KT. *Scripta Materialia.* 2009;60:619.

- [106] Tang F, Anderson IE, Gnaupel-Herold T, Prask H. Mater. Sci. Eng. A-Struct. Mater. Prop. Microstruct. Process. 2004;383:362.
- [107] Kouzeli M, Mortensen A. Acta Mater. 2002;50:39.
- [108] Li Y, Ramesh KT. Acta Mater. 1998;46:5633.
- [109] Gustafson TW, Panda PC, Song G, Raj R. Acta Mater. 1997;45:1633.
- [110] Lee J, Kim NJ, Jung JY, Lee ES, Ahn S. Scripta Materialia. 1998;39:1063.
- [111] Zener C, Hollomon JH. Journal of Applied Physics. 1944;15:22.
- [112] Wingrove AL. Metallurgical Transactions. 1973;4:1829.
- [113] Rogers HC. Annual Review of Materials Science. 1979;9:283.
- [114] Wei Q, Kecskes L, Jiao T, Hartwig KT, Ramesh KT, Ma E. Acta Mater. 2004;52:1859.
- [115] Dodd B, Bai Y. Materials Science and Technology. 1985;1:38.
- [116] Wright TW, Walter JW. Journal of the Mechanics and Physics of Solids. 1987;35:701.
- [117] Debye P. Annalen Der Physik. 1912;39:789.
- [118] Kula E, DeSisto T. Behavior of Materials at Cryogenic Temperatures, American Society for Testing and Materials, 1966.
- [119] Chin GY, Hosford WF, Backofen WA. Transactions of the Metallurgical Society of Aime. 1964;230:437.
- [120] Hosford WF, Fleischer RL, Backofen WA. Acta Metallurgica. 1960;8:187.
- [121] Basinski ZS. Proceedings of the Royal Society of London Series a-Mathematical and Physical Sciences. 1957;240:229.
- [122] Stock TAC, Wingrove AL. Journal of Mechanical Engineering Science. 1971;13:110.
- [123] Valiev RZ, Ivanisenko YV, Rauch EF, Baudelet B. Acta Mater. 1996;44:4705.
- [124] Wright WJ, Schwarz RB, Nix WD. Mater. Sci. Eng. A-Struct. Mater. Prop. Microstruct. Process. 2001;319:229.

- [125] Wright WJ, Saha R, Nix WD. *Materials Transactions*. 2001;42:642.
- [126] Recht RF. *Journal of Applied Mechanics*. 1964;86:189.
- [127] Bowden PB. *Philosophical Magazine*. 1970;22:455.
- [128] Grady DE. *Journal of the Mechanics and Physics of Solids*. 1992;40:1197.
- [129] Grady DE. *Mechanics of Materials*. 1994;17:289.
- [130] Stock TAC, Thompson KR. *Metallurgical Transactions*. 1970;1:219.
- [131] Craig JV, Stock TAC. *Journal of the Australasian Institute of Metals*. 1970;15:1.
- [132] Shockey DA, Curran DR, Seaman L. SRI International Technical Report. 1985;
- [133] Irwin CJ. DREV-R-652/72. 1972;46.
- [134] Meyers MA, Nesterenko VF, LaSalvia JC, Xue Q. *Mater. Sci. Eng. A-Struct. Mater. Prop. Microstruct. Process*. 2001;317:204.
- [135] H. K. *Proceedings of the Royal Society of London B*. 1949;62:676.
- [136] Hopkinson B. *Philosophical Transactions of the Royal Society of London Series a-Containing Papers of a Mathematical or Physical Character*. 1914;213:437.
- [137] Sekar K, Allesu K, Joseph MA. *Dynamics of Machines and Mechanisms, Industrial Research*. 2014;592-594:102.
- [138] Davies EDH, Hunter SC. *Journal of the Mechanics and Physics of Solids*. 1963;11:155.
- [139] Follansbee P. *ASM Handbook*, ASM International, Materials Park, OH, 1985.
- [140] Suryanarayana C. *Prog. Mater. Sci*. 2001;46:1.
- [141] MJ L, CS J, MM D, MM M, J V. Multicomponent ultrafine microstructures. In: LE M, DE P, RW S, BH K, (Eds.). *MRS Proceedings*, vol. 132. Pittsburgh: Pittsburgh, PA Materials Research Society, 1989. p.79.
- [142] Perez RJ, Huang B, Lavernia EJ. *Nanostructured Materials*. 1996;7:565.
- [143] Smith CS. *Transactions of the American Institute of Mining and Metallurgical Engineers*. 1948;175:15.

- [144] Dogan ON, Michal GM, Kwon HW. Metallurgical Transactions a-Physical Metallurgy and Materials Science. 1992;23:2121.
- [145] Manohar M, Ferry M, Chandra T. ISIJ International. 1998;38:913
- [146] Li Y, Liu W, Ortalan V, Li WF, Zhang Z, Vogt R, Browning ND, Lavernia EJ, Schoenung JM. Acta Mater. 2010;58:1732.
- [147] Zhang HT, Ye JC, Joshi SP, Schoenung JM, Chin ESC, Gazonas GA, Ramesh KT. Advanced Engineering Materials. 2007;9:355.
- [148] Ye JC, He JH, Schoenung JM. Metallurgical and Materials Transactions a-Physical Metallurgy and Materials Science. 2006;37A:3099.
- [149] Manufacturing AM. What We Do. <http://www.am2t.com/WhatWeDo.html>.
- [150] Witkin DB, Lavernia EJ. Prog. Mater. Sci. 2006;51:1.
- [151] Tellkamp VL, Melmed A, Lavernia EJ. Metallurgical and Materials Transactions a-Physical Metallurgy and Materials Science. 2001;32:2335.
- [152] Guo YZ, Behm NA, Ligda JP, Li YL, Pan Z, Horita Z, Wei Q. Materials Science and Engineering: A. 2013;586:149.
- [153] Gu G, Ye LY, Jiang HC, Sun DX, Zhang P, Zhang XM. Transactions of Nonferrous Metals Society of China. 2014;24:2295.
- [154] Mines RAW. Composite Structures. 2004;64:55.
- [155] Lundberg P, Renstrom R, Lundberg B. Int. J. Impact Eng. 2000;24:259.
- [156] Lin T, Yang Q, Tan C, Liu B, McDonald A. Journal of Materials Science. 2008;43:7344.
- [157] Vogt R, Zhang Z, Huskins E, Ahn B, Nutt S, Ramesh KT, Lavernia EJ, Schoenung JM. Mater. Sci. Eng. A-Struct. Mater. Prop. Microstruct. Process. 2010;527:5990.
- [158] Zhang Z, Chen DL. Scripta Materialia. 2006;54:1321.
- [159] Domnich V, Reynaud S, Haber RA, Chhowalla M. Journal of the American Ceramic Society. 2011;94:3605.
- [160] Clausen AH, Borvik T, Hopperstad OS, Benallal A. Mater. Sci. Eng. A-Struct. Mater. Prop. Microstruct. Process. 2004;364:260.

- [161] Jiang L, Wen HM, Yang HR, Hu T, Topping T, Zhang DL, Lavernia EJ, Schoenung JM. *Acta Mater.* 2015;89:327.
- [162] Gleiter H. *Prog. Mater. Sci.* 1989;33:223.
- [163] Clyne TW, Withers PJ. *An Introduction to Metal Matrix Composites*, University Press, Cambridge, 1993.
- [164] Last HR, Garrett RK. *Metallurgical and Materials Transactions a-Physical Metallurgy and Materials Science.* 1996;27:737.
- [165] Ramakrishnan N. *Acta Mater.* 1996;44:69.
- [166] Vogt R, Zhang Z, Li Y, Bonds M, Browning ND, Lavernia EJ, Schoenung JM. *Scripta Materialia.* 2009;61:1052.
- [167] Taya M, Lulay KE, Lloyd DJ. *Acta Metall. Mater.* 1991;39:73.
- [168] Chawla N, Andres C, Jones JW, Allison JE. *Metallurgical and Materials Transactions a-Physical Metallurgy and Materials Science.* 1998;29:2843.
- [169] Lee SH, Cho KM, Kim KC, Choi WB. *Metallurgical Transactions a-Physical Metallurgy and Materials Science.* 1993;24:895.
- [170] Ferkel H, Mordike BL. *Mater. Sci. Eng. A-Struct. Mater. Prop. Microstruct. Process.* 2001;298:193.
- [171] Wei Q, Cheng S, Ramesh KT, Ma E. *Mater. Sci. Eng. A-Struct. Mater. Prop. Microstruct. Process.* 2004;381:71.
- [172] Hart EW. *Acta Metallurgica.* 1967;15:351.
- [173] Wang YM, Ma E. *Mater. Sci. Eng. A-Struct. Mater. Prop. Microstruct. Process.* 2004;375:46.
- [174] Wang YM, Ma E. *Acta Mater.* 2004;52:1699.
- [175] Dodd B, Bai Y. *Adiabatic Shear Localization: Frontiers and Advances.* 2nd ed., Elsevier, 22 Jamestown Road, London, 2012.
- [176] Follansbee PS, Regazzoni G, Kocks UF. *Institute of Physics Conference Series.* 1984;71.
- [177] Carreker RP, Hibbard WR. *Acta Metallurgica.* 1953;1:656.
- [178] Wang YM, Chen MW, Zhou FH, Ma E. *Nature.* 2002;419:912.

- [179] May J, Hoppel HW, Goken M. *Scripta Materialia*. 2005;53:189.
- [180] Korchef A, Njah N, Masmoudi J, Kolsi A, Champion Y, Guerin S, Leroux C. *Advanced Engineering Materials*. 2004;6:639.
- [181] Williams JC, Starke EA. *Acta Mater*. 2003;51:5775.
- [182] Wu XY, Ramesh KT, Wright TW. *Int. J. Solids Struct*. 2003;40:4461.
- [183] Singh PM, Lewandowski JJ. *Metallurgical Transactions a-Physical Metallurgy and Materials Science*. 1993;24:2531.
- [184] Raj R, Ashby MF. *Acta Metallurgica*. 1975;23:653.
- [185] Roy I, Chauhan M, Lavernia EJ, Mohamed FA. *Metallurgical and Materials Transactions a-Physical Metallurgy and Materials Science*. 2006;37A:721.
- [186] Wu XY, Ramesh KT, Wright TW. *Journal of the Mechanics and Physics of Solids*. 2003;51:1.
- [187] Huang Y, Hutchinson JW, Tvergaard V. *Journal of the Mechanics and Physics of Solids*. 1991;39:223.
- [188] Flom Y, Arsenault RJ. *Acta Metallurgica*. 1989;37:2413.
- [189] Zhao D, Tuler FR, Lloyd DJ. *Acta Metall. Mater*. 1994;42:2525.
- [190] Argon AS, Im J, Safoglu R. *Metallurgical Transactions*. 1975;A 6:825.
- [191] He MY, Hutchinson JW. *Int. J. Solids Struct*. 1989;25:1053.
- [192] Marshall DB, Cox BN, Evans AG. *Acta Metallurgica*. 1985;33:2013.
- [193] Tvergaard V, Hutchinson JW. *Journal of Applied Mechanics-Transactions of the Asme*. 1993;60:807.
- [194] Alpas AT, Zhang J. *Metallurgical and Materials Transactions a-Physical Metallurgy and Materials Science*. 1994;25:969.
- [195] Arsenault RJ, Shi N. *Materials Science and Engineering*. 1986;81:175.
- [196] Ravichandran KS. *Acta Metall. Mater*. 1994;42:1113.
- [197] Vaidya AR, Lewandowski JJ. *Mater. Sci. Eng. A-Struct. Mater. Prop. Microstruct. Process*. 1996;220:85.

- [198] Ding HZ, Biermann H, Mughrabi H. *Fatigue & Fracture of Engineering Materials & Structures*. 2000;23:847.
- [199] Hall JN, Jones JW, Sachdev AK. *Mater. Sci. Eng. A-Struct. Mater. Prop. Microstruct. Process*. 1994;183:69.
- [200] Allison JE. *Fundamentals of Metal Matrix Composites*, Elsevier, 1993.
- [201] Bonnen JJ, Allison JE, Jones JW. *Metallurgical Transactions a-Physical Metallurgy and Materials Science*. 1991;22:1007.
- [202] Hahn GT, Rosenfield AR. *Metallurgical Transactions*. 1975;A 6:653.
- [203] Wang YM, Ma E. *Applied Physics Letters*. 2003;83:3165.
- [204] Clifton RJ, Duffy J, Hartley KA, Shawki TG. *Scripta Metallurgica*. 1984;18:443.
- [205] Dai LH, Liu LF, Bai YL. *Int. J. Solids Struct*. 2004;41:5979.
- [206] Xu XB, Ling Z, Wu X, Bai YL. *Journal of Materials Science & Technology*. 2002;18:504.